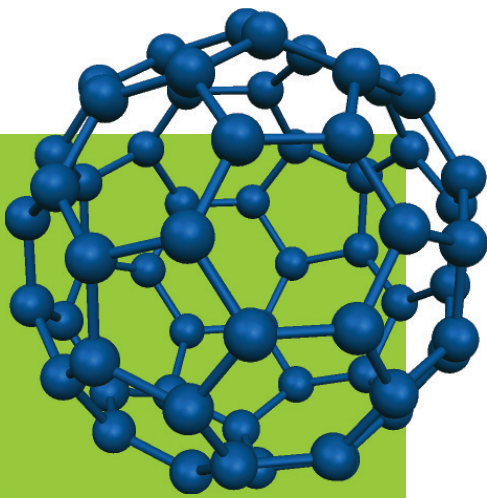


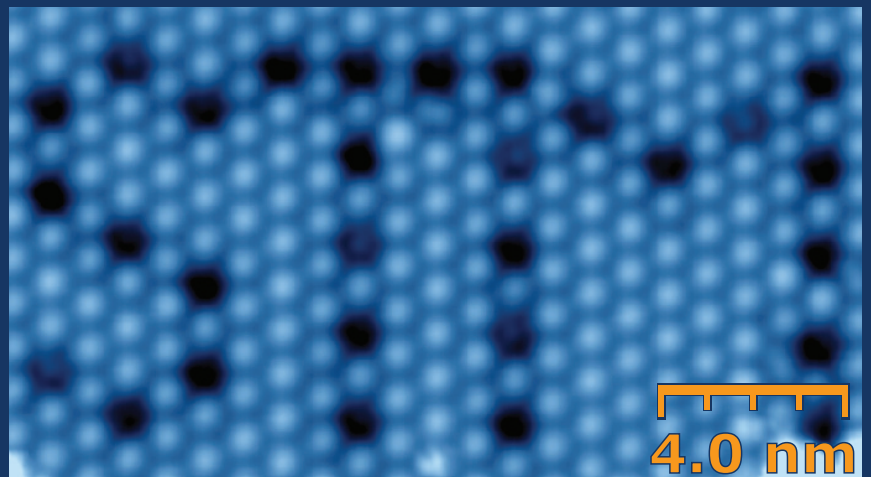
# Elementary Processes in Single Molecule Devices: Electronic Transport and Molecular Isomerization



Doctoral Thesis

Gunnar Schulze

Institut für Experimentalphysik  
Freie Universität Berlin





---

# Elementary Processes in Single Molecule Devices: Electronic Transport and Molecular Isomerization

---

Doctoral Thesis

of

**Gunnar Schulze**



submitted to the  
Department of Physics  
of the  
Freie Universität Berlin

November 2009

Diese Arbeit entstand in der Arbeitsgruppe von Prof. Dr. José Ignacio Pascual am Fachbereich Physik der Freie Universität Berlin.

Berlin, November 2009

Erstgutachter: Prof. Dr. José Ignacio Pascual

Zweitgutachter: Prof. Dr. Paul Fumagalli

Drittgutachter: Prof. Dr. Richard Berndt

Datum der Disputation: 18. Januar 2010



## Zusammenfassung

Diese Arbeit beschreibt die Untersuchung fundamentaler Aspekte organischer Moleküle auf Metalloberflächen mit Hilfe der Rastertunnelmikroskopie (RTM) und der Rastertunnelspektroskopie (RTS). Dabei werden drei Punkte behandelt: Thermische Effekte in C<sub>60</sub>-Molekülen, die mittels Tunnelströmen geheizt werden, das Isomerisationsverhalten von molekularen Photo-Schaltern auf Metalloberflächen und das Transportverhalten durch einzelne molekulare Drähte zwischen zwei Metallelektroden (RTM-Spitze und Probe).

Inelastisch streuende Tunnelelektronen führen zu einem vibrationellen Heizen von C<sub>60</sub>-Molekülen im Tunnelkontakt. Wird der Tunnelstrom in den  $\mu$ A-Bereich erhöht, so kommt es zu einem thermisch induzierten irreversiblen Bruch der ikosaederförmigen Struktur des Moleküls. Die dazu benötigte Leistung zeigt eine Abhängigkeit von der angelegten Tunnelspannung. Im Vergleich mit Transportrechnungen lässt sich zeigen, dass der größte Anteil an der Heizleistung auf resonant tunnelnde Elektronen zurückzuführen ist, während vibrationsunterstütztes resonantes Tunneln sowie die Erzeugung von Elektron-Loch-Paaren im Metall-Molekül-Grenzgebiet die wichtigsten Kühlmechanismen darstellen. Durch den Vergleich der elektrischen Leistungen die zum Zerstören des Moleküls auf drei verschiedenen Oberflächen (Cu(110), Pb(111) und Au(111)) benötigt werden, lässt sich weiterhin schließen, dass der Beitrag der Elektron-Loch-Paar-Erzeugung zur gesamten thermischen Stabilität von der energetischen Position der LUMO-Resonanz abhängt und zusammen mit der Stärke des Ladungstransfers in das Molekül ansteigt.

1,3,3-Trimethylindolino-6-nitrobenzopyrylospiran (SP) ist ein molekularer Photo-Schalter, der bei Temperaturen unter 270 K geordnete Inseln auf Au(111)- und Bi(110)-Oberflächen bildet. Über 300 K findet eine thermisch induzierte Isomerisationsreaktion der Moleküle in die isomere Form Merocyanin (MC) statt. Während für freie Moleküle SP das stabilere Isomer darstellt, konnten wir beobachten, dass MC auf den beiden untersuchten Oberflächen die stabilere Form ist. Der Grund ist eine Stabilisierung der planaren Struktur der MC-Moleküle auf der Oberfläche, die eine flache Adsorption ermöglicht. Desweiteren konnten SP→MC-Isomerisationsreaktionen beobachtet werden, die durch Elektronenanlagerung im LUMO der SP-Moleküle hervorgerufen werden. Auf der Bismut-Oberfläche konnten durch Beleuchtung einer reinen SP-Präparation mehrere unterschiedliche geordnete Inselstrukturen erzeugt werden, die aus einer Mischung aus SP- und MC-Molekülen bestehen und deren MC:SP-Verhältnis mit der Beleuchtungsmenge anwächst. Außerdem wurden Hinweise auf bidirektionales SP⇌MC-Photoschalten gefunden.

Metall-Molekül-Metall-Kontakte sind ein fundamentales Konzept der Quanten-Transport-Forschung, da sie die Messung des reinen Elektronenflusses durch ein Einzelmolekül, ohne den Einfluss einer strombegrenzenden Tunnelbarriere erlauben. Polypenylmoleküle mit zwei unterschiedlichen Ankergruppen wurden auf Kupferoberflächen aufgebracht, wo sie sich in Ketten anordnen. Die Tauglichkeit von amino- und pyridylterminierten Molekülen für das Kontaktieren und Abheben von der Oberfläche mittels der RTM-Spitze wurde untersucht. Reproduzierbare Kontakte konnten zu den Pyridyl-Endgruppen hergestellt werden, was die Messung von grundlegenden Leitungseigenschaften erlaubt.

## Abstract

Using scanning tunneling microscopy (STM) and spectroscopy (STS), we investigate fundamental aspects of organic molecules adsorbed on metal surfaces. We address three different topics: thermal effects in  $C_{60}$  molecules heated by tunneling electron currents, the isomerization behavior of photo-switching molecules on metal surfaces and the transport behavior through single molecular wires that are fixed between two metal electrodes (STM tip and sample).

$C_{60}$  molecules placed inside an STM tunneling junction exhibit a vibrational heating induced by inelastically scattering tunnel electrons. We observe that the molecules' icosahedral cages undergo a thermally induced irreversible degradation when the applied currents are raised to the  $\mu A$  range. The power needed for decomposition shows a dependence on the applied bias voltage. In comparison with transport calculations, we find that heating by resonantly tunneling electrons accounts most for the temperature increase while vibron assisted tunneling through resonances and the creation of electron-hole ( $e-h$ ) pairs at the molecule-metal interface are the most important cooling mechanisms. Comparing the decomposition powers on three different substrates, Cu(110), Pb(111) and Au(111), we find that the contributions of  $e-h$  pair creation to the overall thermal stability of the fullerene depend on the energetic alignment of the LUMO resonance, and increases with the amount of charge transfer to the molecule.

1,3,3-Trimethylindolino-6-nitrobenzopyrylospiran (SP) is a photo-switching molecule that forms ordered islands on Au(111) and Bi(110) at temperatures below 270 K. Above 300 K, the molecules are found to undergo a thermal reaction into their isomer merocyanine (MC). Unlike in the case of free molecules, where SP is known to be the most stable isomer, the MC molecules are found to be more stable on the two investigated surfaces. This is due to a stabilization of the planar MC structure on the metal, where it adsorbs flatly.  $SP \rightarrow MC$  isomerization by electron attachment into the SP LUMO could be observed as well. On bismuth, illumination of a pure SP preparation gives rise to a number of distinct self-assembled monolayer structures, consisting of a mixture of both MC and SP species with a MC:SP ratio increasing with the applied photon fluence. Furthermore, a fingerprint of bidirectional  $SP \rightleftharpoons MC$  photoisomerization was found.

Metal-molecule-metal junctions are a fundamental concept of quantum transport research since they allow the observation of bare electronic transport through single molecules without the hindering barrier of a tunneling gap. Poly-phenyl molecules with two different anchoring end groups were adsorbed on copper surfaces, where they assemble in chains. The suitability of the amino- and pyridil-terminated molecules for contacting and lifting from the surface with the STM tip was explored. Contact formation to the pyridil end groups could be achieved reproducibly and basic conductance properties were measured.

# Contents

<b>1</b>	<b>Introduction</b>	<b>1</b>
<b>2</b>	<b>Experimental and Theoretical Techniques</b>	<b>5</b>
2.1	STM, STS and IETS . . . . .	5
2.1.1	Tunneling Current . . . . .	7
2.1.2	Tunneling Spectroscopy . . . . .	9
2.1.3	Inelastic Electron Tunneling Spectroscopy . . . . .	12
2.2	Additional Surface Science Techniques . . . . .	14
2.2.1	High Resolution Electron Energy Loss Spectroscopy . . . . .	15
2.2.2	X-Ray Photoelectron Spectroscopy . . . . .	15
2.2.3	Near Edge X-Ray Absorption Fine Structure Spectroscopy . . . . .	16
2.3	Substrates and Surfaces . . . . .	17
2.3.1	Au(111), Cu(111), Cu(100) and Cu(110) . . . . .	17
2.3.2	Pb(111) . . . . .	18
2.3.3	Bi(110) . . . . .	19
2.4	Preparation Methods . . . . .	19
<b>3</b>	<b>Thermal Stability of Molecular Junctions</b>	<b>21</b>
3.1	Tunneling, Mechanical and Electronic Contact . . . . .	22
3.2	Molecular Degradation . . . . .	25
3.2.1	C <sub>60</sub> Monolayers on Metal Surfaces . . . . .	25
3.2.2	Current-Induced C <sub>60</sub> Decomposition . . . . .	28
3.2.3	Statistical Character of C <sub>60</sub> Decomposition . . . . .	30
3.3	Thermal Balance of the Molecular Junction . . . . .	34
3.3.1	Molecular Heating and Cooling Mechanisms . . . . .	36
3.3.2	Influence of the Substrate Metal . . . . .	39
3.4	Conclusion . . . . .	43
<b>4</b>	<b>Chemical Conversion of Adsorbed Photoswitches</b>	<b>45</b>

4.1	Excitation Mechanisms . . . . .	46
4.2	The Spiropyran Molecule . . . . .	47
4.3	Spiropyran on Au(111) . . . . .	50
4.3.1	Temperature Dependent Ring-Opening . . . . .	53
4.3.2	Stabilization Inversion on the Metal Surface . . . . .	58
4.3.3	Tip-induced Ring Opening . . . . .	59
4.3.4	Effect of Illumination . . . . .	62
4.4	Ring-Opening Reactions of Spiropyran on Bi(110) . . . . .	63
4.4.1	Adsorption on Bi(110) . . . . .	64
4.4.2	Thermally Induced Ring-Opening . . . . .	64
4.4.3	Tunnel Electron Induced Ring-Opening . . . . .	66
4.4.4	Photo-Induced Isomerization . . . . .	68
4.5	Conclusion . . . . .	74
<b>5</b>	<b>Transport Through Contacted Molecule Junctions</b>	<b>77</b>
5.1	Contact Formation and Lift-Up . . . . .	78
5.1.1	Di-Amino-Tri-Phenyl on Cu(100) . . . . .	82
5.1.2	Di-Pyridyl-Bi-Phenyl on Cu(111) . . . . .	85
5.1.3	Lifting Properties . . . . .	87
5.2	Spectroscopic Analysis of the DPBP Bridge Junction . . . . .	92
5.3	Conclusion and Outlook . . . . .	94
<b>6</b>	<b>Summary</b>	<b>97</b>
<b>A</b>	<b>Appendix A Details of Data Analysis</b>	<b>101</b>
A.1	Assignment of Peak Onsets in Incomplete Spectra . . . . .	101
A.2	Determination of Photo Quantum Yield . . . . .	102
A.3	Decomposition Dynamics Model . . . . .	105
A.3.1	Limitations of the Model . . . . .	109
<b>B</b>	<b>Appendix B Numerical Methods</b>	<b>111</b>
B.1	Force Field Molecular Mechanics Calculations . . . . .	111
	<b>References</b>	<b>113</b>

# Chapter 1

## Introduction

In the past years, large scale numerical simulations have proven to be an excellent tool for the understanding of complex systems. Climate models, simulations of epidemic spread or cosmological models are popular examples [1, 2, 3]. The rising importance of such calculations brings an increasing demand for more computing power. At the same time, the exponential growth of the world's data stored in electronic systems calls for a reduction of the size of the storage devices. Over the last decades, both requirement were achieved by a successive shrinking of the feature size of silicon based integrated circuits [4]. Nevertheless, it is assumed that the ongoing miniaturization of classical CMOS devices will sooner or later reach its final limits. Signal fluctuations due to quantum tunneling effects and tremendous power dissipation are expected to severely affect the devices functionality at circuit widths below 20 nm [5].

One possible solution of this problem is the emergence of molecular electronics. This concept, that was first proposed by Richard Feynman in 1959 [6], describes a novel type of electronic devices that use single molecules as building blocks for signal processing, i.e. molecular wires, molecular switches, or molecular diodes [7]. Organic molecules are the most promising candidates for this purpose, since they can be synthesized in many structures and allow a tuning of their electronic properties. Moreover, they provide an approach to solve the question of microscopic structuring of the components by their ability to order in self-assembled patterns.

Although many advances in creating functional molecular components have been made in the past years [8, 9, 10], molecular electronics is still in a conceptual stage and more than a decade of developing time will be needed to build the first applications. Many details of the interactions between molecules, surfaces and other particles as electrons, phonons, and plasmons are still unknown today, but ongoing research activities aim to explore the elementary processes of the molecular components.

This thesis deals with a number of selected topics of the field of molecular electronics. A low-temperature scanning tunneling microscope (LT-STM) was used as main tool of investigation. The STM has a high spatial resolution in the picometer scale and is here used to image, probe, and manipulate single molecules. This allows us to study effects on individual molecules that cannot be observed in a molecular ensemble. The STM tip can furthermore be utilized as metallic electrode to contact distinct molecules and form electrode-molecule-electrode junctions. In combination with scanning tunneling spectroscopy (STS) measurements, that give detailed information about the electronic properties of the sample, the scanning tunneling microscope provides a powerful tool for our research.

The first topic that is addressed in this work is the issue of thermal stability of a single molecule when it supports the transport of large current densities. Energy dissipation into heating of the conducting molecules is expected to be a serious problem of molecular electronics. Here, we examined the thermal stability of single  $C_{60}$  fullerene molecules on three different metal surfaces. The key question was hereby to identify the fundamental mechanisms of electron-induced heating and molecular cooling that determine the molecular temperature when an electric current passes through. The molecule is heated by inelastic scattering of the transmitted electrons with vibrational modes. For the cooling, two dominant mechanisms could be identified: cooling by vibron-assisted tunneling and the creation of electron-hole pairs in the electrodes. At large current densities the cooling mechanisms become insufficient to compensate for the increased heating, what leads to a structural collapse of the fullerene cage. We show that the efficiency of cooling processes mediated by electron-hole pair creation and, thus, the stability of the molecule against electrical power, can be drastically increased by the choice of an electrode material that provides a high charge transfer into the molecule.

Molecular switches are good candidates to serve as single memory bits in molecular electronics devices. For this purpose, the switching behavior needs to be conserved in the proximity of metallic electrodes. As a second aspect of this thesis, we examined the switching behavior of the molecular photoswitch trimethylindolino-nitrobenzopyrrolospiran (SP) on a metal surface. In solution, SP molecules undergo a chemical reaction into their isomeric merocyanine (MC) form upon heating or illumination. We show that a thermal isomerization of SP molecules on a metal surface into the MC form is possible, but backswitching turns out to be hindered by the substrate. The same applies when isomerization is induced by the attachment of tunneling electrons into the lowest unoccupied molecular orbital (LUMO) of the SP molecules. The efficiency of the isomerization induced with light depends crucially on the density of electronic states (DOS) of the electrode around the Fermi level. On metals with a high DOS, as gold, this process is drastically quenched by a shortening of the lifetimes of excited molecular states. On bismuth instead, a metal with a lower DOS at the Fermi energy, bidirectional photo-isomerization processes could be observed. A higher substrate temperature during illumination is also found to enhance the rate of photo-isomerization.

The final topic of this work treats the contacting and conductance behavior of molecular wires fixed between two metal electrodes. Charge transport through single molecules is a fundamental concept of molecular electronics that is not yet fully understood. Elongated molecules can serve as molecular wires that transport electric current between two contacts [9]. The details of the contact to the electrodes are known to have a great influence on the transport behavior [11]. Here we approach this topic by contacting one end of polyphenyl molecules that were functionalized with different anchoring end groups in order to form a stable bond to the STM tip. The molecules can then be straightened up from the surface by a gradual retraction of the tip. Our interests are hereby in the following points: i) to determine what anchoring end groups are most suitable to form reliable contacts to the metal tip electrode; ii) how far can the molecules be lifted; iii) what transport phenomena can be discovered in the  $I$ – $V$  curves of such a “molecular bridge” junction; iv) what information can we get from the photon spectrum of such a molecular junction. This project is still in progress and important topics of the present state of research are presented in this script.





## Chapter 2

# Experimental and Theoretical Techniques

### 2.1 Scanning Tunneling Microscopy, Scanning Tunneling Spectroscopy and Inelastic Electron Tunneling Spectroscopy

Scanning tunneling microscopy (STM) is a well-established and powerful method of surface science that allows real-space imaging of conducting or semiconducting surfaces in the nanometer range. The technique is based on the tunneling properties of electrons through a small potential barrier. To locally probe the sample, a sharp metallic tip with a single atom termination is positioned within a short distance of a few Ångströms (*tunnel gap*) above the surface. Positioning with a precision in the picometer scale is achieved by piezo-mechanical elements. The application of a *sample bias voltage*  $V_S$  in a range from a few millivolts to some volts between tip and sample results in different chemical potentials of electrons in the two leads. Since the quantum mechanical tunnel effect allows a small number of electrons to cross the short potential barrier of the tunnel gap, a resulting net current  $I_t$  can flow over this junction. The amount of the current depends on a number of parameters like applied voltage, tip and surface material, and geometric properties of the tip, but it shows also an exponential dependence on the tunnel gap distance  $z$ . The last feature allows the control of  $z$  by automatic regulation of the tip position to keep the tunneling current at a defined value (*feedback current*). An electronic feedback loop is used for this purpose. The tip is now swept laterally in a line-by-line fashion over the sample while recording the piezo-voltage that is needed to keep the current at  $I_t$ , what results in a data matrix that holds local information about the electronic and in particular geometric properties of the scanned area of the sample, the *STM topography image*. The exponential

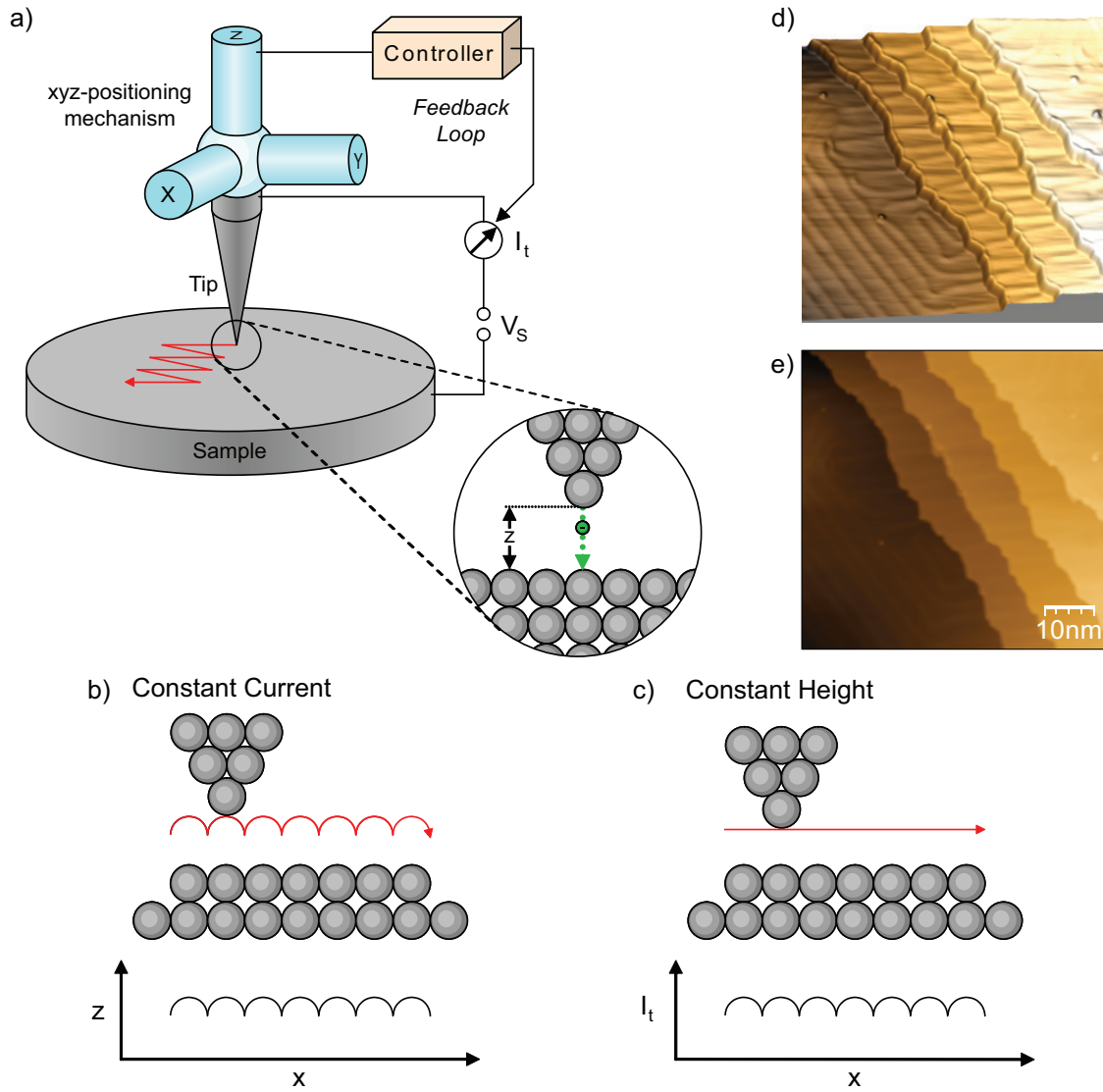


Figure 2.1: a) Working principle scheme of an STM. The gap  $z$  is controlled to keep the tunneling current  $I_t$  fixed for a given bias voltage  $V_s$ . To record images, the tip is moved over the surface line by line (red arrow). b, c) Principles of the scanning modes of constant current (b) and constant height (c): the image is taken either from the  $z$  or the  $I_t$  signal. d, e) Exemplary 60 × 60 nm constant current topography image of a clean Au(111) surface, taken with  $V_s = 1.1$  V and  $I_t = 0.2$  nA. The  $z$  signal is visualized differently in the two images: in d) as relief height and in e) as color contrast.

dependence of  $I_t(z)$  and the high precision of the tip control enables the STM to achieve atomic resolution under good conditions.

Beside the above described *constant current* imaging mode of the STM it is also possible to scan without using the feedback loop, once the height properties of a local area on the sample are known. In this case, the tip is swept at a certain  $z$  position over the sample while the tunneling current  $I_t$  is recorded. The data array resulting from this *constant height* mode technique again holds a mixture of electronic and geometric information and is denoted as *STM current image*. As far as not noted otherwise, all images presented in this work are taken in constant current mode. For treatment and processing of the images, the software “WSxM” was used [12].

The operation conditions of the STM used throughout this work include a He cooling bath that provides a constant temperature of about 5 K during the measurements (*low temperature STM*, LT-STM). Furthermore, all experiments were performed in an ultra-high vacuum (UHV) environment.

### 2.1.1 Tunneling Current

The situation of an STM tunnel gap can be understood as depicted in the energy diagrams 2.2. We assume that tip and sample are made up of equal material, i.e. with equal work functions  $\phi_t = \phi_s$ , what is ensured by our tip preparation method (see section 2.4). On application of a sample bias voltage  $V_s$ , the chemical potentials (i.e. the positions of the Fermi levels) are shifted by an energy  $eV_s$  with respect to each other. For evaluating the amount of current flowing through the junction, it is necessary to sum up all pairs of initial and final electron states of tip and sample with weighting factors that express the amount of transmission that can take place between each pair of states. For an initial state  $\psi_\mu$  and a final state  $\psi_\nu$  with energies  $E_\mu$  and  $E_\nu$  the current can be written as

$$I_t(V_s) = \frac{2\pi e}{\hbar} \int d\mu \int d\nu f(E_\mu) [1 - f(E_\nu)] \delta(E_\mu - E_\nu + eV_s) |M_{\mu\nu}|^2, \quad (2.1)$$

where the Pauli principle is ensured by the factor including the Fermi functions  $f(E)$  and the energy conservation is given by the  $\delta$ -function [13, 14]. Bardeen has shown that the tunneling matrix element  $M_{\mu\nu}$  can be expressed as

$$M_{\mu\nu} = -\frac{\hbar^2}{2m_e} \int d\vec{S} \left( \psi_\mu^* \nabla \psi_\nu - \psi_\nu \nabla \psi_\mu^* \right), \quad (2.2)$$

that is the current operator of the two states integrated over an infinite surface  $\vec{S}$  extending in the tunnel gap and separating the tip from the sample [15]. By neglecting the bias voltage potential and assuming spherical s-type tip wave functions, this quantity was first evaluated by Tersoff and Hamann [13]. Often it is useful to include the voltage potential

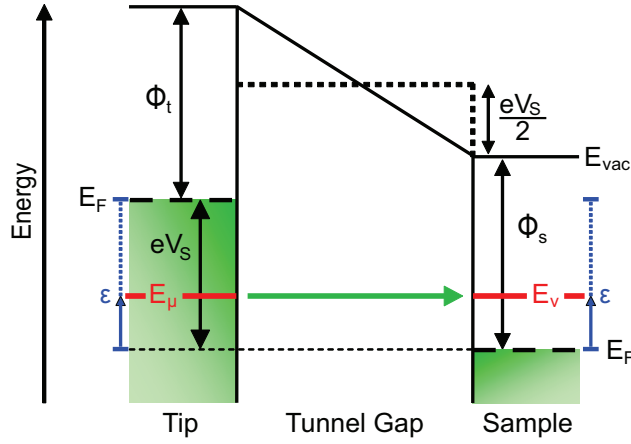


Figure 2.2: Schematic tunnel barrier energy diagram depicting the various parameters. The tunneling from the electron state at  $E_\mu$  to the one at  $E_v$  is explained in the text. The energy integration window is marked blue. The block approximation of the voltage potential barrier is marked by the dotted lines.

into the transition matrix by calculation of a WKB approximated solution [16]. For the slightly simplified case of a flat potential with a height of  $eV_s/2$  above the sample vacuum energy  $E_{\text{vac}}$  (see figure 2.2) this yields

$$|M_{\mu\nu}|^2 \sim \exp \left( -z \, 2 \sqrt{\frac{2m_e}{\hbar^2}} \sqrt{E_{\text{vac}} - E_v + \frac{eV_s}{2}} \right). \quad (2.3)$$

This treatment assumes all initial states with energy  $E_\mu$  to be equal (and the same for final states with energy  $E_v$ ), what brings another advantage: the transition coefficient  $|M_{\mu\nu}|^2$  can now be considered as depending only on the energy of the two states. Thus the integration over all states in equation 2.1 can be simplified by summing over all states of a given energy for each lead first, what results in the local densities of states (LDOS) at this energy  $\sigma(E)$ . Only energy integrals remain in the equation:

$$I_t(V_s, z) = \frac{2\pi e}{\hbar} \int dE_\mu \int dE_v \, \sigma(E_\mu) \sigma(E_v) f(E_\mu) [1 - f(E_v)] \times \delta(E_\mu - E_v + eV_s) |M_{\mu\nu}|^2 \quad (2.4)$$

$$= \frac{2\pi e}{\hbar} \int_{-\infty}^{\infty} d\epsilon \, \sigma_t(E_F + \epsilon - eV_s) \sigma_s(E_F + \epsilon) \times f(E_F + \epsilon - eV_s) [1 - f(E_F + \epsilon)] |M_{\mu\nu}|^2. \quad (2.5)$$

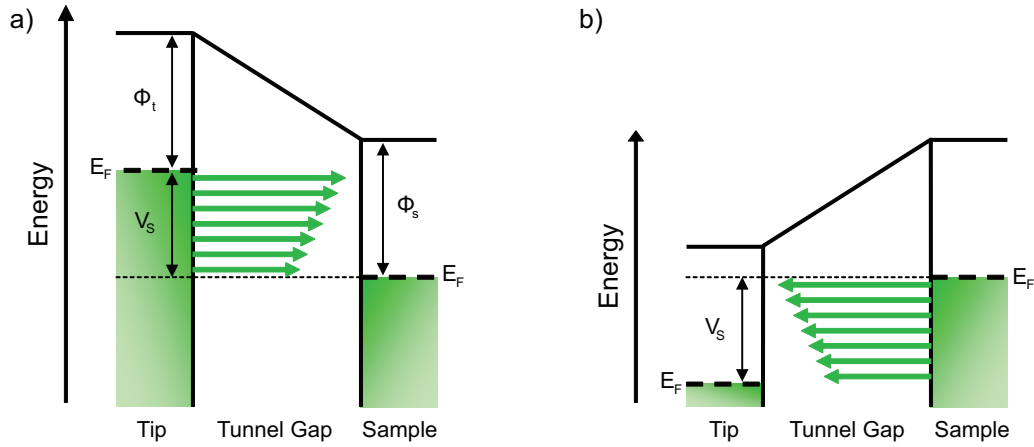


Figure 2.3: Schematic diagrams showing the tunneling process for positive (a) and negative (b) bias voltages  $V_S$ . The complete energy window  $[E_F, E_F + V_S]$  contributes to the resulting current  $I_t$ . In principle, tunneling is simplified for higher energy values (longer arrows) since they experience a lower barrier.

For the last equation the  $\delta$ -function was evaluated and an integration energy  $\varepsilon$  was introduced (see figure 2.2). The tunnel direction was assumed to be from the tip to the sample for positive bias voltages. Since the energy resolution of most of our experiments is by far lower than the temperature broadening that enters via the Fermi functions, we can make the approximation of zero temperature. The tunneling current then becomes

$$I_t(V_S, z) = \frac{2\pi e}{\hbar} \int_0^{eV_S} d\varepsilon \sigma_t(E_F + \varepsilon - eV_S) \sigma_s(E_F + \varepsilon) |M_{\mu\nu}(\varepsilon, V_S, z)|^2 \quad (2.6)$$

$$|M_{\mu\nu}(\varepsilon, V_S, z)|^2 \sim \exp\left(-z \sqrt{\frac{2m_e}{\hbar^2}} \sqrt{\phi - \varepsilon + \frac{eV_S}{2}}\right).$$

In this equation we can see the most important features of the STM current: the exponential  $z$ -dependence, the relation to the tip and surface DOS and the dependence on the energy window defined by the bias voltage. The schematic drawings of figure 2.3 depict this picture.

### 2.1.2 Tunneling Spectroscopy

Beside the imaging capability of the STM it is possible to gain information about the observed sample by performing *scanning tunneling spectroscopy* (STS) [14, 17]. The idea

is to use the above relations to measure the LDOS of the sample  $\sigma_s$  at different energies. If we assume that the transition coefficient  $|M_{\mu\nu}|^2$  and the density of states of the tip  $\sigma_t$  depend only little on the bias voltage in the energy window under observation, what is approximately the case for a metallic tip, we find that the derivative of  $I_t$  with respect to  $V_S$  is proportional to  $\sigma_s$ :

$$\frac{dI_t}{dV_S} \sim |M|^2 \sigma_t \cdot \sigma_s(E_F + eV_S). \quad (2.7)$$

The accuracy of this relation is sufficient for many purposes, where the  $dI_t/dV_S$  curve is taken to be equivalent to the LDOS spectrum around  $E_F$ . Nevertheless, the approximation of a constant  $|M_{\mu\nu}|^2$  is not always satisfactory: if a scanning tunneling spectrum is taken over a broad voltage range, e.g. from 0 to more than 3 V, the exponential  $V_S$ -dependence of the transition coefficient can cause serious deformations of the resulting spectrum. This has been simulated for three different measurements and normalization schemes of  $dI_t/dV_S$  curves in figure 2.4. The ‘classical’ way of recording STS data includes a fixed tip position at a distance  $z$  above the sample. If peaks are present in  $\sigma_s(E)$ , the exponential underground introduced by  $|M_{\mu\nu}|^2$  causes a shift of their maxima towards higher energies, as can be seen in figure 2.4 b). In addition the decreasing tunneling barrier enlarges the amplitude of peaks at higher voltages. This causes the effect that two equal maxima of  $\sigma_s(E)$ , one lying close and the other far from  $E_F$ , will be displayed in the resulting  $dI_t/dV_S$  curve with apparent heights that differ in orders of magnitude. These effects are particularly strong for large distances  $z$  (i.e. small feedback currents) and for broader features in  $\sigma_s(E)$ . A normalization procedure can be used to treat both problems [14, 18]. Therefore, the derivative of the natural logarithm of the two parameters, i.e.  $(d \ln I_t / d \ln V_S) = (V_S / I_t) \cdot dI_t / dV_S$ , is taken as spectrum. The resulting curve is referred to as *normalized derivative* and is shown in figure 2.4 c). It partially solves the problems described above, but has a tendency to downshift the maximum of peaks at higher energies. The curve is dimensionless and its value at  $V_S = 0$  is unity by definition. Unfortunately this method shows some drawbacks for experimental curves with a high noise level: at regions close to  $V_S = 0$  the noise of the normalized curve can become incredibly high. It is therefore necessary to decide for each situation if the application of the normalization procedure is useful. For the last method of recoding  $dI_t/dV_S$  spectra, the feedback loop stays active and the spectrum is measured at a constant current (see figure 2.4 d). This method is not suitable for voltages close to 0 V but it gives fair results at higher energies. The peak shifting behavior is comparable to the normalized derivative.

The general experimental procedure to measure the local DOS is therefore comparatively easy: the tip is placed over the sample at a position where  $\sigma_s$  shall be measured. Then the feedback loop is switched off to fix the  $z$  value during the experiment. Now, the voltage is ramped over the energy window of interest while recording the tunneling current. The  $dI_t/dV_S$  curve can either be acquired by numerical derivation or by application of a

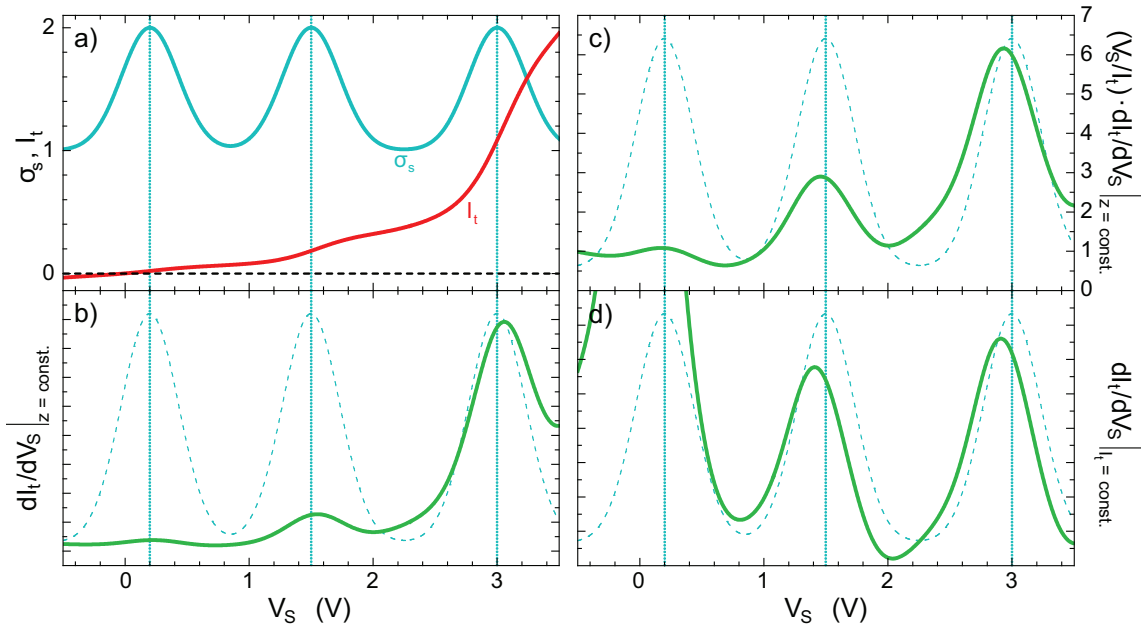


Figure 2.4: Simulated  $dI_t/dV_S$  curves for a generic sample LDOS as depicted in a) (turquoise line): three Gaussian peaks (centered at 0.2, 1.5 and 3.0 eV) on a constant underground. The red curve is the resulting tunneling current. The classical  $dI_t/dV_S$  curves without (b) and with (c) normalization were calculated at a constant  $z$ , while curve (d) was calculated for a constant  $I_t$  value. The calculations were performed from equation 2.6 with parameters  $\phi = 5.5$  eV and  $z = 10$  Å (a–c).

*lock-in amplifier technique*, what usually leads to lower noise and a higher resolution. This method represents an experimental implementation of the variational principle. A small sinusoidal voltage modulation with an amplitude of a few millivolts and a frequency of some hundreds of hertz is added to  $V_S$ . These variations are rendered by the physical system into small superimposed oscillations of  $I_t$  with an amplitude proportional to  $dI_t/dV_S$ . The lock-in amplifier compares the original modulation voltage with the resulting current and generates a final output signal that scales with the desired derivative.

The described technique also shows another important advantage: the magnitude of  $dI_t/dV_S$  can be measured *statically* without the need of varying  $I_t$ . This feature is very helpful if the local density of states shall be mapped spatially, i.e.  $\sigma_s(x, y)$ , what is commonly known as  *$dI_t/dV_S$ -mapping*. To create such a map, the area of interest is scanned while recording the  $dI_t/dV_S$ -signal from the lock-in amplifier. This can be done in constant current mode as well as in constant height mode. In both cases the resulting data matrix is a spatial representation of the local density of states on the sample at the energy  $E_F + eV_S$ . This is of high interest for the case of spatial variations of the electronic landscape, e.g. for adsorbates that introduce electronic states at their positions. How good the correspondence between the visual appearance of the probability enclosing surface of a



molecular electronic state and the  $dI_t/dV_S$ -mapped image of the same state may be seen in references [19, 20].

## Molecular Adsorbates

If the electronic structure of surface-adsorbed molecules is investigated by STS, the special properties of the technique and of the observed adsorbate system should be considered for data interpretation. It should be kept in mind that STS probes the *cationic* or *anionic* states of a molecule, since the tunneling electrons are removed from or added to the molecule. This means that in a first place not the neutral HOMO and LUMO are detected but the molecule's *ionization potential* and *electron affinity* levels. Nevertheless, in the proximity of the metal these states are nearly identical to HOMO or LUMO: if an electron is placed in the electron affinity level, its electric field will immediately be screened by the close-by metal electron sea. Therefore the electron “feels” a strongly reduced Coulomb repulsion and the electronic state is shifted closer to the “real” LUMO, i.e. down in energy towards the Fermi level. A similar process accounts for the ionization potential, that is shifted upwards in energy. Another important effect is the lifetime broadening of the electronic states: unlike in a free molecule, electrons or holes can quickly leave the molecular states into the metal, usually in timescales of  $10^{-15}$  s. This leads to a lifetime broadening of several tens to hundreds of meV of all observed states that can also be understood as quantum mechanically mixing of the molecular states with the energetically broad metal electron bands. These effects are depicted in figure 2.5. A third effect that affects the electronic level of a molecule can show up if charge is transferred into or out of the molecule: an alignment of LUMO or HOMO close to  $E_F$  may cause, in combination with the explained level broadening, a permanent increase or reduction of electric charge on the molecule. This, however, may lead to complex electronic rearrangements, including the formation of surface dipoles, additional screening by the metal, band bending, changes of the local work function and finally a realignment of the corresponding molecular levels [21].

### 2.1.3 Inelastic Electron Tunneling Spectroscopy

An important aspect that has not been illuminated yet is the capability of tunneling electrons to interact with molecular vibrations. This means that the crossing electrons can absorb or emit single molecular vibrational quanta (*vibrons*) that can best be visualized as level steps of a harmonic oscillator potential. The interactions have two main influences on the behavior of the current-voltage curve  $I_t(V_S)$ : the appearance of current kinks at the vibron energies due to inelastic tunneling effects and the appearance of additional elastic channels.



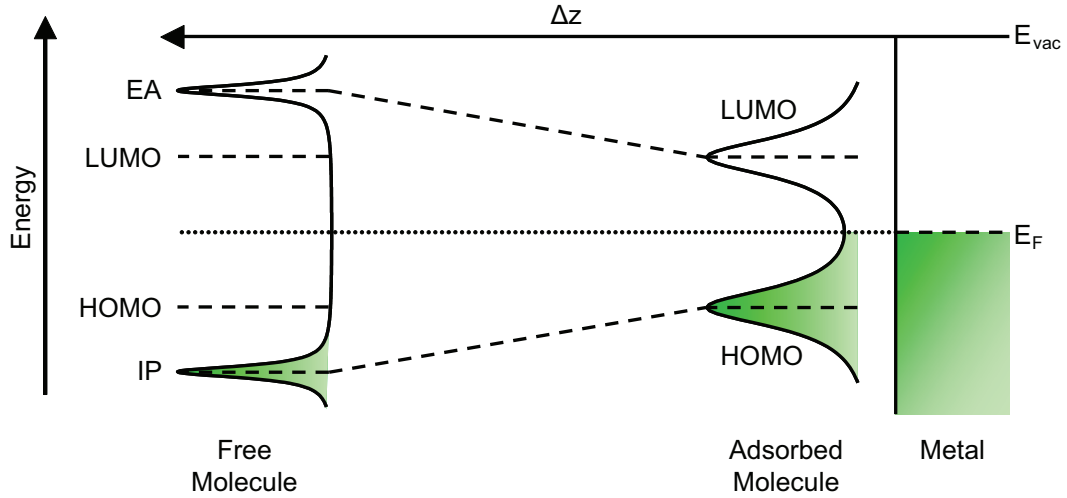


Figure 2.5: Schematic drawing of molecular level shifting and broadening effects on adsorption. Experimental methods that probe molecular resonances by electron attachment or detachment cannot directly measure the LUMO or HOMO resonances of a free molecule (left side). Instead, they record the corresponding ion resonances, i.e. the electron affinity level (EA) or the ionization potential (IP). On adsorption the distance  $\Delta z$  between molecule and metal is reduced (right side). Additional screening by the metal surface reduces the local electrostatic potential of the ionized molecule and the EA and IP levels approach towards the neutral molecule's LUMO and HOMO. STS probed these states. In addition, a level broadening takes place since electronic excitations can decay into the metal, what reduces the lifetimes of these states.

The first process of the two is measured by *inelastic electron tunneling spectroscopy* (IETS) (figure 2.6). The underlying effect can be explained by an easy picture [22, 23]: as long as the sample bias is smaller than the energy of the respective vibrational mode, i.e.  $eV_S < \hbar\omega$ , no tunneling electron can interact with the vibrons. If the bias reaches  $\hbar\omega/e$ , a small part of the electrons can deposit their energy into the excitation of the vibrational mode and leave the molecule with reduced energy (inelastic tunneling). This first order interaction process can be viewed as additional channel for the electrons to traverse the junction. Since this channel will be used by a certain fraction of *all* electrons with energies larger than  $\hbar\omega$ , the  $I_t(V_S)$  curve has an increased slope starting from this point, where the curve has a kink. The detection of this kink can be carried out in a similar way as the STS measurements but with the difference that here the second derivative  $d^2I_t/dV_S^2$  shows peaks at the respective energies. Since the effect does not depend on the traveling direction of the electrons, a similar peak is found at a negative sample bias. Only vibrations that show a sufficiently large electron-vibron coupling can be detected by this method, which are typically the Jahn-Teller active modes of a molecule [24].

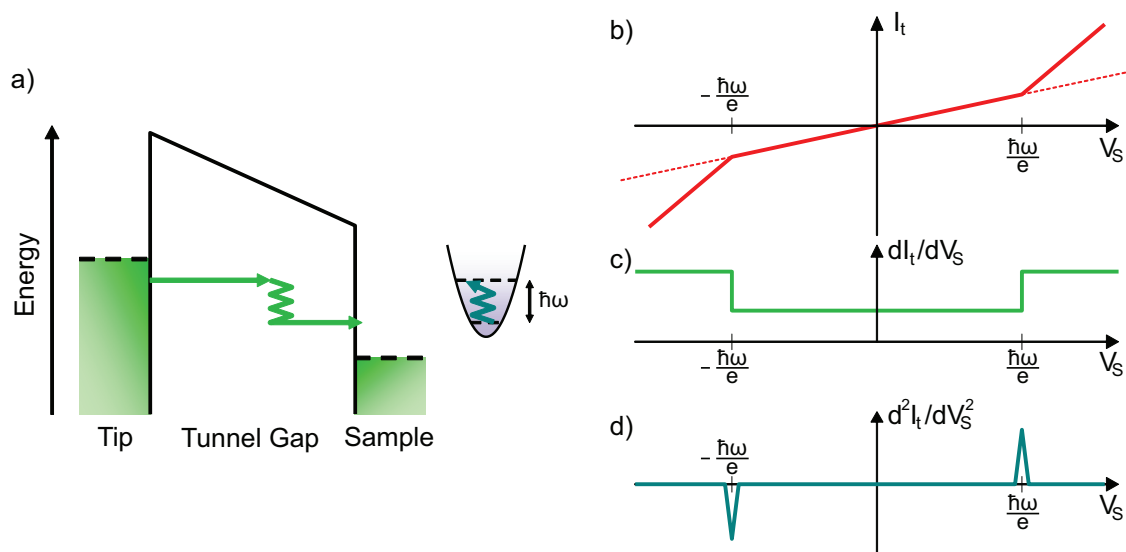


Figure 2.6: Schematic drawing of inelastic tunneling spectroscopy (IETS). a) If the energy window is adequate for the electron to tunnel under vibron emission, this channel will appear. The additional inelastically tunneling electrons lead to kinks in the  $I_t$  curve (b), that translate into steps in the  $dI_t/dV_s$  curves (c) and into a peak/dip pair in the  $d^2I_t/V_s^2$  signal (d).

In contrast to this inelastic process is the resonant tunneling through vibrational excitations of electronic resonances, commonly known as *vibronic levels*. The tunneling probability for an electron cannot benefit from a resonance level  $E_r$  if the electron energy  $eV_s$  is higher than  $E_r$ . This can change, if the electron can deposit a certain amount of energy into vibrational excitations to reach  $E_r$ : the electron has now a higher chance to cross the junction. It is not necessary for the electron to permanently deposit the energy but it can enhance its tunneling probability by excitation of virtual vibrons in a resonant tunneling process<sup>1</sup>. The result of this effect is the emergence of sharp peaks at energies  $E_r + n \cdot \hbar\omega^*$  in the  $dI_t/dV_s$  spectra [25, 26, 27], where  $\omega^*$  denotes the vibrational mode of the charged molecule. Usually, these features can only be seen if the molecule is well decoupled from the surface, e.g. by an oxide layer, since the molecular levels are quenched and broadened in the proximity of the metal.

## 2.2 Additional Surface Science Techniques

A number of other standard techniques of surface science have been used for analyzing parts of this work. This section shall give a short overview over these methods.

<sup>1</sup>This can be imagined as additional propagation diagram  in a path integral picture.

### 2.2.1 High Resolution Electron Energy Loss Spectroscopy

The technique of high resolution electron energy loss spectroscopy (HREELS) can be used to determine vibrational spectra of surface adsorbates [28]. Therefore, a beam of monoenergetic electrons is focused on the sample under a certain impact angle. The scattering electrons can interact with the adsorbates and lose a part of their energy into the excitations of vibrations. From a subsequent analysis of the scattered electron energies for different angles, a spectrum over the amount of energy loss can be deduced, that shows characteristic peaks at the energetic positions of the activated vibrational modes.

The actual electron-vibron interaction takes place due to three effects: electron scattering on molecular resonances (*resonance scattering*), on vibrational dipoles (*dipole scattering*) and by direct electron-ion interaction (*impact scattering*). While the first one is only of minor importance for surface vibrational spectroscopy, we want to briefly discuss the other two effects, that are depicted in figure 2.7. Dipole scattering can be pictured as an interaction between the moving dipole that is build up by the approaching electron and its image charge with the molecular dipolar component that is perpendicular to the surface [29]. Thus, only vibrational modes with a nonzero dipole moment in this direction contribute to this effect. Another important feature of dipole scattering is the low amount of momentum transfer that is mainly deposited before the electrons arrive at the surface, due to the long-range character of dipole interactions. When the electrons finally arrive, they scatter into roughly an equal direction as non-interacting electrons. Dipole scattered electrons are therefore mainly found in the specular direction [29]. Electrons that are impact scattered interact directly with the molecule's ion cores what results in a angle distribution that has no preference for the specular direction. The types of vibrations that can be addressed by this effect are defined by special selection rules, but they include vibrations with no dipolar component perpendicular to the surface.

The practical way to decide, if an observed vibrational peak is dominated by dipole or impact scattering (what may allow a statement about the  $z$ -component of the dipole) is therefore to measure spectra in and out of the specular direction.

### 2.2.2 X-Ray Photoelectron Spectroscopy

X-ray photoelectron spectroscopy (XPS) is based on the photo effect and is used to get information about core level binding energies of specific atoms in adsorbed molecules. X-rays with a monochromatic energy are used to excite core electrons, e.g. from the 1s state into the vacuum [30]. The kinetic energy of the emitted electrons is detected and the binding energy of the initial level can be determined as difference to the x-ray photon energy. Since atomic core levels are not involved in the chemical bonds, their energetic positions are approximately equal to the one of an elemental atom, e.g. at  $\sim 400$  eV for the 1s level of nitrogen. This allows an easy assignment of the observed peaks to the

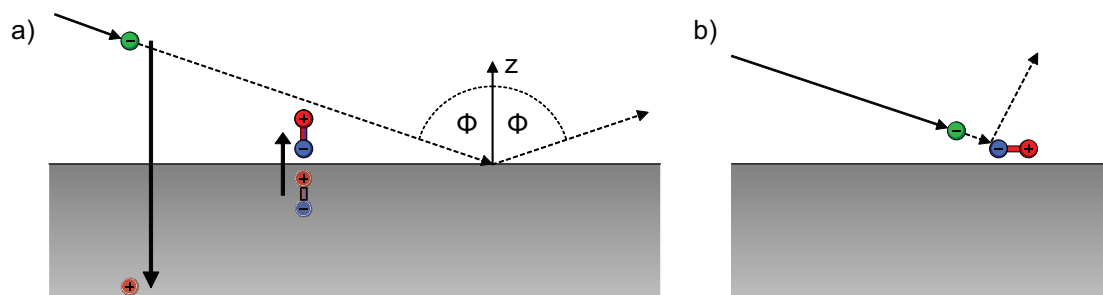


Figure 2.7: Schematic drawings of the two dominant electron scattering effect of electron energy loss spectroscopy on adsorbates. a) Dipole scattering between the electron-image dipole (large arrow) and the  $z$  component of the the vibron mode's electric dipole (small arrow). b) Impact scattering can also address dipoles parallel to the surface but it has a broader scattering angle distribution.

respective elements. On the other hand, the chemical environment, i.e. the oxidation state of the atom, can lead to small but detectable *chemical shifts* of a few meV from the original level position. The capability to determine these shifts is one important feature of the XPS technique. Besides that, XPS can be used for the quantitative analysis of the adsorbed layers.

### 2.2.3 Near Edge X-Ray Absorption Fine Structure Spectroscopy

A similar method for detecting chemical bond structures of surface adsorbed molecules is the near edge X-ray absorption fine structure (NEXAFS) spectroscopy [31]. Like XPS, its general idea is to use monochromatic X-rays to excite characteristic core level electrons into higher states that are, unlike XPS, close to but still below the vacuum level. A direct detection of the X-ray absorption is impracticable for thicker substrates, since the beam may be absorbed completely by the sample. Therefore, signals of the relaxation process, that are fluorescence intensities or the amount of emitted Auger electrons, are usually measured and plotted vs. the X-ray photon energy. NEXAFS is typically applied to “low- $Z$  molecules” containing carbon, nitrogen and oxygen, where the energy region of the K-edge (1s to vacuum) is probed (figure 2.8 a).

The general advantage over XPS lies in the fact that the final states are typically antibonding  $\pi^*$  or  $\sigma^*$  orbitals, that have a highly directional absorption characteristics, depending on dipole selection rules. In combination with polarized light and adjustable incidence angles, this technique can be used to determine the geometric orientation of the probed orbital with respect to the surface. Transitions into a  $\pi^*$  orbital in a C=C bond, for example, show a higher activation rate if the polarization vector of the exciting light is oriented perpendicular to the bond direction than if bond and polarization are aligned parallel (fig-

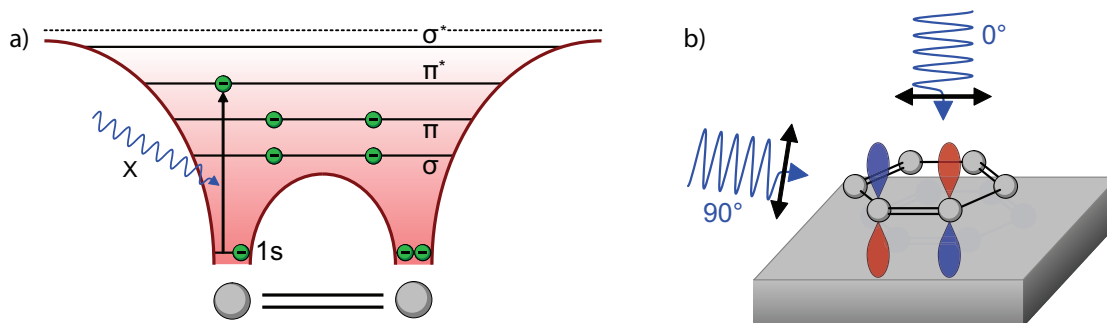


Figure 2.8: Schematic drawings of the NEXAFS method. a) shows a simple energy scheme for a  $1s$  to  $\pi^*$  level photoexcitation. The sensitivity to the bond direction of the process is shown in b): polarized light in grazing angle ( $90^\circ$ ) is more likely to excite into the  $\pi^*$  orbitals of a flat-lying double bond than illumination from the surface normal direction ( $0^\circ$ ).

ure 2.8 b). In many cases this information can be used to deduce the orientation of the adsorbate with respect to the surface. In addition to that, the chemical shifts that are found in XPS spectra are also likely to reappear in a NEXAFS measurement, although here more care has to be taken to differentiate between initial and final state effects.

## 2.3 Substrates and Surfaces

Investigations on five different surfaces of four different metals have been carried out in this work. This section wants to give a short outline of the most important features of these surfaces.

### 2.3.1 Au(111), Cu(111), Cu(100) and Cu(110)

Low-index surfaces of coinage metals (Cu, Ag, Au) are typically the first choice for STM investigations on metal surfaces: they are thoroughly investigated, easy to prepare and offer a broad variety of parameters like different surface symmetries or chemical reactivities. At the same time these metals belong to the same chemical subgroup and thus have many properties in common: a face center cubic (fcc) crystalline structure, a filled d-band edge just below the Fermi level ( $\sim -2$  eV for Cu and Au), that is important for chemisorption processes and a conduction band consisting of the respective s- and p-bands. The surface symmetry of the (111) surfaces is trigonal, while it is rectangular for the (110) and quadratic for the (100) surfaces. In our experiments Au(111), Cu(111) and Cu(110) were used as adsorption templates. On all three surfaces Shockley surface states are present

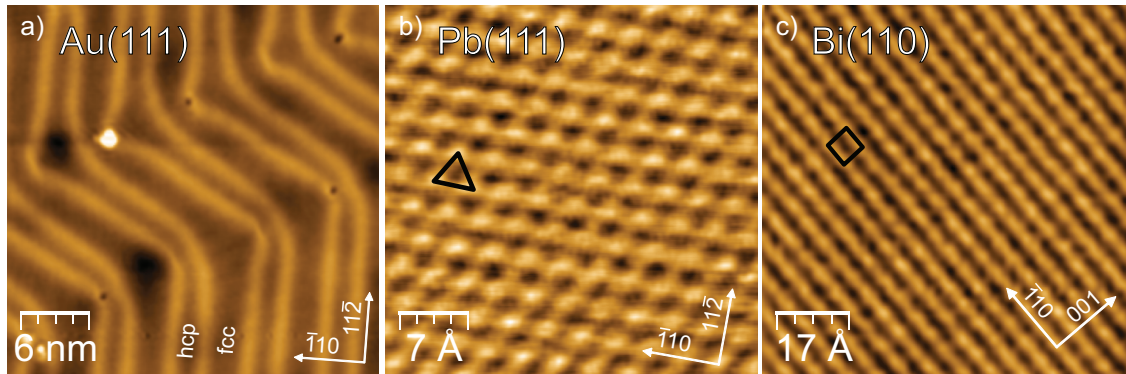


Figure 2.9: a) A Au(111) surface with its typical herringbone reconstruction lines. The elbow sites are preferential adsorption places. b) Atomic resolution on a Pb(111) surface. The triangular structure is clearly visible (black triangle). c) The rather complicated Bi(110) surface appears in first approximation as a pseudo-cubic (100) surface. Nevertheless, slight deviations from this simplified model result in the disappearance of every second atom (not visible, in the center of the black box) and in the observed line structure. Feedback parameters are: a)  $I_t = 20$  pA,  $V_S = 1.0$  V, b)  $I_t = 0.4$  nA,  $V_S = 3.3$  V, c)  $I_t = 0.3$  nA,  $V_S = 70$  mV.

with onset energies between 400 and 500 meV below  $E_F$  [32, 33]. The Au(111) surface shows a characteristic herringbone reconstruction of stripes with alternating face center cubic (fcc) and hexagonally closed packed (hcp) surface layers [34]. The reactivity for chemisorption differs between the three metals: from the mostly inert Au over Ag to Cu, the most reactive material of this group. In addition, the coordinative saturation of the topmost layer atoms is also variable for the diverse cutting directions. A (111) surface, being the “most closed”, is less reactive than a (100) or even a (110) surface, which has the fewest number of neighbors per atom. As a rule of thumb we can thus state that we expect an increasing reactivity for the surfaces Au(111), Cu(111), Cu(100) and Cu(110).

### 2.3.2 Pb(111)

A Pb(111) sample was used in our experiments presented in chapter 3 since it provides an alignment of  $C_{60}$  adsorbate resonances at an ideal intermediate position between the corresponding alignments on Au(111) and Cu(110). Whereas the crystalline structure of Pb is similar to the coinage metals, its band structure around the Fermi level differs clearly: the only important band at  $E_F$  is the bulk 6p-band that contributes to the conduction exclusively. No surface states are reported for Pb(111). However, an interesting property of the material is to be superconducting below 7 K.



### 2.3.3 Bi(110)

The certainly most exotic surface that was used in our experiment is Bi(110). Being formally a metal, the Bi bulk material is commonly labeled as “semi-metal” since its valence band and conduction band hardly overlap at  $E_F$ , resulting in a very low bulk density of states that is available for charge transport. This situation can change at the surface: depending on the cutting direction, the topmost atoms may be left over with free half-filled dangling bond states. In an ideal case, these states can form a metallic surface state. It has been found [35] that this is the case for a (110) surface: here, a large number of different surface states are present, showing a rather complex Fermi surface. Since their conductivity exceeds the one of the bulk states at  $E_F$ , the system can nearly be thought of as a two-dimensional metal. In our experiments, a Bi(110) surface was used because of its comparably weak density of states at the Fermi level and the low binding strength that is expected for the binding of phenyl rings (see chapter 4). This surface is also regarded as particularly interesting because its surface states show considerable spin-splitting effects.

The geometric structure of Bi is rhombohedral, but it can be approximated as a simple-cubic (*pseudo-cubic*) lattice (i.e. with angles that are not exactly  $90^\circ$ ) [36]. In this system, the Bi(110) translates into a (100) surface with a quasi-squared topmost atom layer, as it is shown in figure 2.9 c).

## 2.4 Preparation Methods

The preparations of all samples and surfaces that were used in this work were performed in UHV preparation chambers that are attached to the LT-STM machines. Thus, the complete cycle of sample cleaning, molecule evaporation, cooling to low temperatures and transferring of samples was done under UHV conditions. The different steps of sample preparation and the typical tip preparation methods will be reviewed briefly in the following section.

### Sample Cleaning

The metallic samples were cleaned by successive cycles of  $\text{Ne}^+$  ion sputtering (1.5 keV, Bi: 1.0 keV) at room temperature followed by annealing to temperatures  $T_{\text{ann}}$  listed below. This procedure ensures mostly adsorbate-free surfaces with extended terraces of the respective type.

Material	Au	Cu	Pb	Bi
$T_{\text{ann}}$	530° C	530° C	160° C	140° C

## Molecule Preparation

All molecules that were used are in a solid state at room temperature. The powders were evaporated from a Knudsen cell onto the cleaned samples. The applied temperatures were directly measured at the crucible. The evaporation temperature of the respective molecules  $T_{\text{evap}}$  is a critical parameter that has to be adjusted thoroughly since we usually aim for coverages of submonolayers only. In some cases, a quartz balance or a quadrupole mass spectrometer were used to detect  $T_{\text{evap}}$ . The temperatures that were used and that led to successful preparations are listed below. If not stated otherwise, the samples were held at room temperature during the evaporation. In some cases, the samples were subsequently annealed to self-order the adsorbed molecules.

Substance	$T_{\text{evap}}$
Di-Amino-Tri-Phenyl	135° C
Di-Cyano-Tri-Phenyl	165° C
Di-Pyridyl-Bi-Phenyl	160° C
C <sub>60</sub>	450° C
1,3,3-Trimethylindolino-6'-nitrobenzopyrylospiran	110° C

## Tip Preparation

Material and condition of the tip is a crucial parameter for all STM based measurements. Therefore it is important to take care that the tip is in a metallic state all the time. To ensure this, two procedures are used as standard methods:

- (i) **Field emission and high voltage treatment:** A voltage of up to 100 V is applied between the tip and a cleaned sample. On approach of tip and sample, the local electric field at the tip is enlarged until an electron beam is emitted. This electron current heats the tip locally what leads to an evaporation of contaminants and oxides. Additionally, the tip is punctured into the sample, what results in a local melting and coverage of the tip with substrate material.
- (ii) **Tip forming:** This technique can be applied during the measurements to restore the metallicity of the tip after a contamination. Therefore, the tip is indented a couple of Ångströms into the clean surface while applying a voltage in the order of a few volts. This usually results in a reformation of the tip apex. The success of such an operation can be monitored by subsequent STS measurements on a clean substrate position: the resulting spectrum's shape allows an estimation of the quality of the tip. The procedure can be repeated until a high-quality tip has been formed.



## Chapter 3

# Thermal Stability of Molecular Junctions

An important aspect of single molecules as building blocks in current conducting junctions is the intended or unintended activation of chemical conversion processes by means of the electric current. If the electron transport through the molecule gains an inelastic component, the draining energy fraction may excite molecular vibrations that sum up and eventually culminate in a significant restructuring of the chemical configuration. Although formally the term of “heat” may not be applied to this situation (the excited vibron population does not necessarily obey a Bose-Einstein distribution) it is illustrative to define an effective model temperature  $T_m$ <sup>1</sup> and use the expression “heat” to depict the potentially degrading character of these excitations for the molecule. The impact of this type of heat is of special importance for potential applications like molecular electronic circuits, where organic molecules serve as logical or conducting components. The contact resistance of such molecules is typically in the order of 10–100 k $\Omega$ . If a voltage of 1 V is applied, what is a typical value for the operation of electronic devices, the current transmitted through the molecule is in the range of 10–100  $\mu$ A. Even at a low inelastic scattering rate of the electrons crossing the molecule, say of 0.01 %, these functional currents would heat the device with power densities of several kW /cm<sup>2</sup>. This depicts the high thermal load such a system would have to withstand and demonstrates that the development of molecular electronic systems requires a profound knowledge of heat accumulation and heat dissipation processes.

One key question is, to what effective temperature the molecule inside a transport experiment gets heated by the flowing current. Although theoretical studies predict values high enough to endanger the integrity of the molecular device [37], only few experiments

---

<sup>1</sup>An effective model temperature  $T_m$  can be defined by associating the internal vibrational energy of the molecule  $E_{vib} = \sum_q \hbar \omega_q N_q$  ( $\hbar \omega_q$ : energy of vibration  $q$ ,  $N_q$ : population of vibration  $q$ ) with the total energy of a Bose-Einstein statistics with a temperature  $T_m$ .

managed to gain reliable information about the temperature inside the microscopic junction [38, 39, 40]. The reason for this is twofold: on the one hand the experiment needs to support a nanoscopic junction. Therefore, scanning probe experiments, besides mechanically controllable break junctions (MCBJ) setups, are the most convenient choice to investigate this topic. On the other hand, the temperature induced by the flowing current is a magnitude that cannot be detected directly with a conventional STM or AFM setup but only through its interference with other parameters. Huang *et al.* used a conducting atomic force microscope (C-AFM) to estimate the temperature increase of a tip-molecule-substrate junction that was formed by lifting of octanedithiol molecules with the tip and so contacting it by two gold leads [38, 39]. The temperature raise, that was detected by the change of the force needed to break the bond between tip and molecule, was about 30 K, what complies to an electronic current heating efficiency  $\gamma \approx 1.5 \text{ K / nW}$ . In another experiment performed by Néel *et al.* it was possible to extract the local temperature of an STM junction from broadening effects observed in  $I$ - $z$  contact curves [40]. They find an effective temperature of 400 K and a heating efficiency of  $\gamma \approx 0.6 \text{ K / nW}$ . Both experiments show, that the local temperature increase caused by heat generation of the electric current can easily reach the order of hundreds of kelvin, i.e. the range where most organic molecules degrade. This emphasizes the importance of further investigations in this field.

In this chapter we study the heating and cooling effects that are present inside an LT-STM junction of single  $\text{C}_{60}$  fullerenes on different metals. The thermal decomposition of the molecule is used as a signal of the temperature of the system. Using this, we observe isothermic current and power curves in dependence of the applied sample bias. In combination with numerical simulations, the contribution of several processes that are involved in heat generation and dissipation are deduced. The molecule is mainly heated by electrons tunneling through resonant states. We find that creation of electron-hole pairs is the most important cooling channel of a vibrationally excited  $\text{C}_{60}$  molecule. The influence of electronic contact between tip and molecule and of molecular resonances on the heat accumulation is observed. A statistical analysis of the degradation process can be applied and yields the number of elemental vibrational excitations that are required to degrade the molecule. Finally we observe the influence of different substrate materials and find that a large charge transfer into the molecule enhances the cooling abilities of the system.

### 3.1 Tunneling, Mechanical and Electronic Contact

Beside the 'classical' operational mode of an STM, the tunneling mode, the tip can be used to build controlled point contacts with the sample under observation. This feature is important for studies in the regime of large electronic currents. A differentiation into three distinct junction states can be made to qualitatively discern the mechanisms of transport. This classification defines the following three regimes

- (i) the *tunneling state* with a finite vacuum gap between tip and sample,
- (ii) the *mechanical contact* between tip and sample with enhanced tunneling probability but without a full conduction channel
- (iii) the *electronic contact* with accessible electronic states bridging tip and sample

The classical operational mode of an STM is, of course, the *electronic tunneling* state, that is characterized by a sufficiently large tip-sample gap  $z$ . As introduced in chapter 2.1.1 the tunneling current  $I_t$  grows exponentially with reducing  $z$ , what is expressed in equation 2.6:

$$I(V, z) \sim \int_0^{eV} d\varepsilon \sigma_t(E_F - eV + \varepsilon) \sigma_s(E_F + \varepsilon) |M_{\mu\nu}(\varepsilon, V, z)|^2$$

$$|M_{\mu\nu}(\varepsilon, V, z)|^2 \sim \exp \left( -z \, 2 \sqrt{\frac{2m_e}{\hbar^2}} \sqrt{\phi - \varepsilon + \frac{eV}{2}} \right).$$

The exponential form of  $I_t(z)$  is in very good agreement with measured curves, as it is shown at the right part of figure 3.1 b). The reason for the  $z$  characteristics of the tunneling matrix element  $M_{\mu\nu}$  is the overlap of the well separated initial and final electron states of tip and sample, whose densities are decaying exponentially into the vacuum [14, 15]. The exponential behavior of  $I_t(z)$  is therefore a good indication for such a separation.

In contrast to this is the situation where an *electronic contact* is formed between the STM tip and the sample. This means that at least one delocalized electronic state exists inside the transport energy window that bridges the complete junction from one to the other lead (fig 3.1 a). This contact can for example be created by a nano object located between tip and sample. Landauer showed [41] that the total transported current is then expected to be

$$I(V_S) = \frac{2e}{h} \cdot eV_S \cdot N_m \quad (3.1)$$

under the assumption that no scattering occurs inside the junction.  $N_m$  is the actual number of such conducting states, which in the case of a small metallic conductor is given by the state quantization in  $x$  and  $y$  direction, and in the case of a molecule bridging the junction by the number of molecular orbitals in the energy window  $[0, eV_S]$  that extends from the

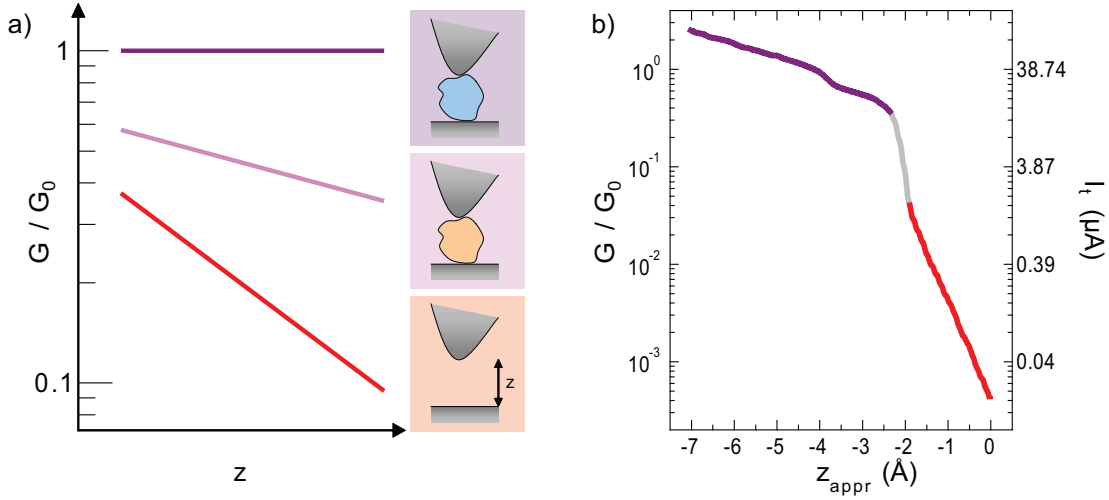


Figure 3.1: a) Scheme of three ideal  $G(z)$  curves (logarithmic scale) of different contact situations: single mode electronic contact (top), pure mechanical contact (middle) and tunneling (bottom). The insets correspond to each situation and sketch the STM junction (blue: conducting object; yellow: non-conducting object). b) Experimental STM curve showing the typical  $I_t(z)$  behavior when approaching from tunnel to electronic contact on top of a molecule. Coming from  $z_{\text{appr}} = 0$  Å, the exponential tunneling region is observed first (red curve), followed by a short transition region and the flat contact region (violet curve). The contact region shows an additional step at  $z_{\text{appr}} = -3.7$  Å which is likely to be originated in the creation of additional conducting modes. The molecule is a  $C_{60}$  fullerene on a Cu(110) surface, the bias voltage is 0.5 V.

tip to the sample. As it can be seen, for  $N_m = 1$  the minimal conductance  $G$  amounts to one *conductance quantum*

$$G_0 = \frac{2e^2}{h} \approx 12.9 \text{ k}\Omega. \quad (3.2)$$

The absence of  $z$  in (3.1) already implies that in electronic contact the current does not directly depend on the tip sample distance over a certain range. Larger changes of  $z$  will of course alter the junction geometry and may therefore influence the number of transmitting modes.

In many cases, the transition between tunnel and electronic contact can easily be detected by a considerable jump of the conductance during tip approach to a value in the order of  $G_0$ , followed by a flatter region, as it is shown in figure 3.1 b).

Beside the two described states a third, intermediate, situation can occur: The junction may be bridged by a nano object that is *not* conducting in the voltage energy window.

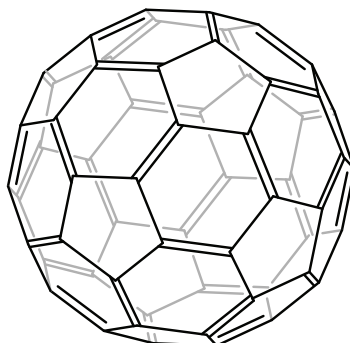


Figure 3.2: Lewis structure of a  $C_{60}$  buckminsterfullerene molecule.

The current conduction of this *pure mechanical contact* state behaves qualitatively like in the tunneling case. Depending on the nano objects permittivity a reduced slope of  $I_t(z)$  may be observed. The question, whether a contact is mechanical or electronic cannot simply be decided by looking at the geometric situation of the junction: a change of the bias voltage can turn a mechanical contact into an electronic one, if the transport energy window is enlarged to include a resonance of the connecting nano object. Therefore, upon contact formation by approaching the tip from the tunneling state, the differentiation between jump to mechanical or to electronic contact can sometimes be difficult. They can best be distinguished by their value of conductance and their different  $G(z)$  behavior.

## 3.2 Molecular Degradation

### 3.2.1 $C_{60}$ Monolayers on Metal Surfaces

Our aim is to study the heating and cooling mechanisms of single molecules in a STM junction. Fullerene  $C_{60}$  molecules (figure 3.2) were chosen as appropriate species for these experiments since their electronic and vibrational features, and contact properties are well characterized. Three metal surfaces, Cu(110), Pb(111) and Au(111), were chosen as substrate material since they cover a representative range of different reactivities and work functions<sup>2</sup>.

A sub-monolayer coverage of  $C_{60}$  molecules was deposited from a Knudsen cell at 450° C on the metal surfaces at room temperature. On Cu(110) the system was further annealed

<sup>2</sup>The work functions of the three metal surfaces are  $\phi_{\text{Cu}(110)} = 4.48$  eV [42],  $\phi_{\text{Pb}(111)} = 3.85$  eV [43] and  $\phi_{\text{Au}(111)} = 5.31$  eV [34].

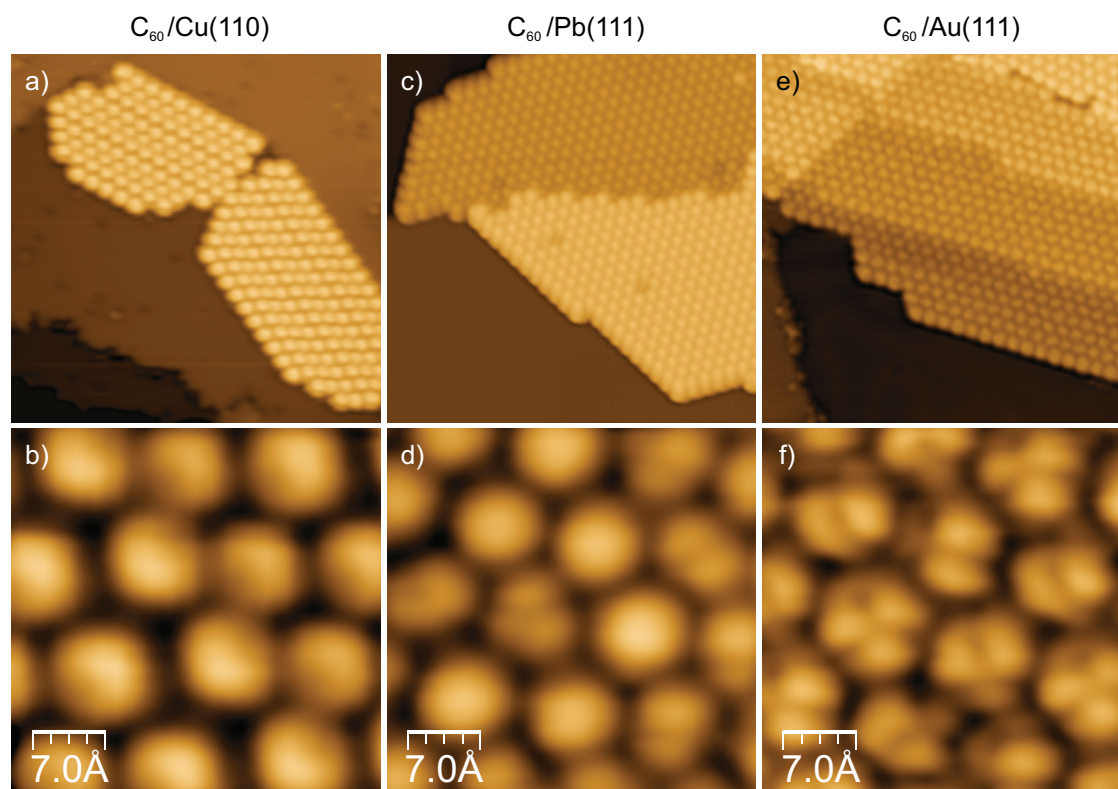


Figure 3.3: Large scale and zoomed STM images of C<sub>60</sub> monolayer islands on (a,b) Cu(110), (c,d) Pb(111) and (e,f) Au(111). The images were recorded with positive bias, thus showing shapes of orbitals of the unoccupied states region. This allows an assignment of the molecular orientation on the surface. Feedback parameter are: a)  $I_t = 1.1$  nA,  $V_S = 1.8$  V, b)  $I_t = 1.0$  nA,  $V_S = 2.3$  V, c)  $I_t = 1.0$  nA,  $V_S = 0.4$  V, d)  $I_t = 2.0$  nA,  $V_S = 0.5$  V, e)  $I_t = 0.57$  nA,  $V_S = 0.4$  V, f)  $I_t = 0.57$  nA,  $V_S = 0.4$  V.

to 470 K to ensure that the molecules self-assemble in ordered domains and populate a thermally stable adsorption state. High resolution STM images allow the determination of the C<sub>60</sub> orientation on the surface by comparison of the internal structure with calculated results of the orbital shapes [19, 20].

On Cu(110), C<sub>60</sub> forms ordered islands with a pseudo-hexagonal structure (figure 3.3 a and b), in which the fullerenes adopt a well-defined adsorption configuration with a pentagon-hexagon C-C bond pointing upwards [44, 45]. An STS spectrum on these molecules (figure 3.4 a) resolves a clear spectroscopic fingerprint characterized by a sharp resonance at  $\sim 1.5$  eV above the Fermi level and associated to the alignment of the LUMO+1 resonance. The LUMO resonance appears as a broader peak centered at  $\sim 0.2$  eV and is partially occupied.

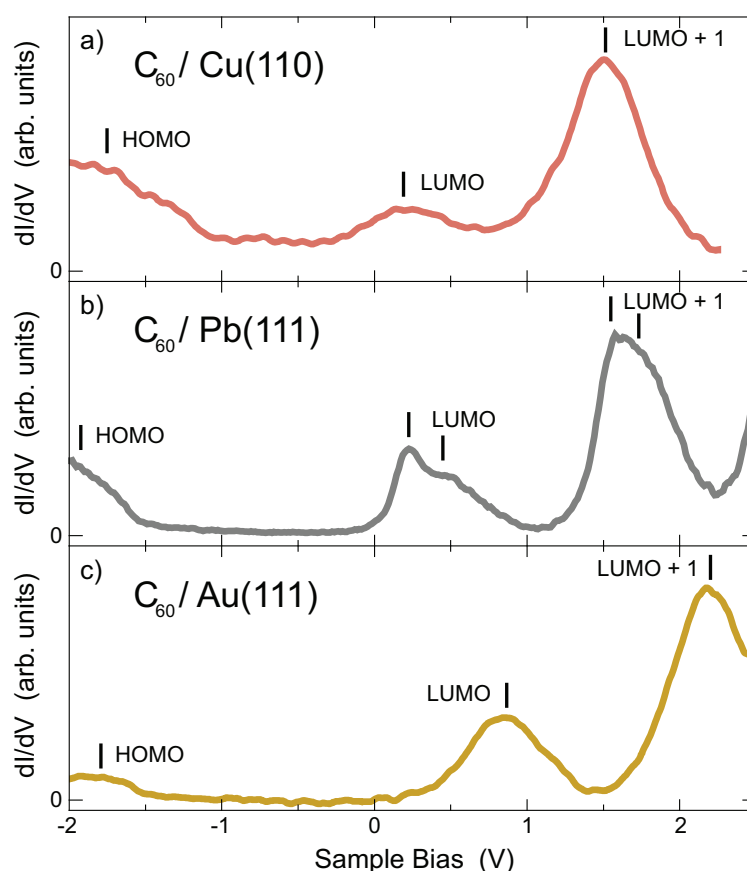


Figure 3.4: Tunnel conductivity spectra of  $C_{60}$  on Cu(110) (a), Pb(111) (b), and Au(111) (c). Bars mark the fitted positions of HOMO, LUMO, and LUMO+1. Two peaks were fitted to the LUMO and LUMO+1 levels on Pb(111).  $dI_t/dV_S$  data were obtained by using a lock-in amplifier with a rms modulation amplitude  $V_{ac}$ . (Cu:  $R_{\text{junct}} = 1.1 \text{ G}\Omega$ ,  $V_{ac} = 20 \text{ mV}$ , Pb:  $R_{\text{junct}} = 0.7 \text{ G}\Omega$ ,  $V_{ac} = 5 \text{ mV}$ , Au:  $R_{\text{junct}} = 0.3 \text{ G}\Omega$ ,  $V_{ac} = 30 \text{ mV}$ .)

$C_{60}$  adsorption on Pb(111) at room temperature results in highly ordered hexagonal islands (figure 3.3 c and d). Here, scanning tunneling spectroscopy reveals the LUMO and LUMO+1 derived resonances as in Cu(110) but more pronounced and with a characteristic split structure due to the breaking of degeneracy upon adsorption (figure 3.4 b). The energetic alignment of the LUMO close to  $E_F$ , with a small tail crossing it, indicates a small amount of charge transfer into the  $C_{60}$  molecule.

Finally, on Au(111) the  $C_{60}$  islands show a similar hexagonal lattice as on Pb(111) (figure 3.3 e and f), but with a larger variety regarding molecular orientations [46], as one can determine from intramolecular structures resembling the lobed shape of the LUMO resonance [20]. Both LUMO and LUMO+1 resonances are resolved in  $dI_t/dV_S$  spectra as pronounced peaks, independently of the molecular orientation [47] (figure 3.4 c). The



position of the LUMO peak appears far from  $E_F$ , at  $\sim 0.8$  eV, what indicates that very few charge is transfer from the substrate [49].

### 3.2.2 Current-Induced $C_{60}$ Decomposition

In our experiments, we approached the STM tip a distance  $z_{\text{appr}}$  towards a single  $C_{60}$  molecule. The approach speed  $\zeta$  was kept constant during the experiments and a value  $\zeta \approx 0.4$  Å/s was used<sup>3</sup>. During the operation, the sample bias  $V_S$  was held fixed while recording the current  $I(z_{\text{appr}})$  flowing through the molecular junction (figure 3.5 a–c).

The tunnel regime is revealed by an exponential increase of  $I(z_{\text{appr}})$  with diminishing gap distance. At a certain approach distance the  $I(z_{\text{appr}})$  curves deviate smoothly from the exponential dependence, indicating the onset of a tip-molecule contact [40]. The conductivity at this point is a small fraction of  $G_0$  which depends on the substrate material. For a small positive sample bias the molecule remains intact upon contact formation and even further indentations of several Ångströms, leading to a stable junction with the molecule contacted by the STM tip on the one side and the metal surface on the other [40]. In this case, the integrity of the indented molecule after tip contact can be verified by its appearance in the STM images (figure 3.5 d and e) and, especially, by its electronic fingerprint in  $dI_t/dV_S$  spectra (figure 3.5 f and g).

If the approach experiments are performed at bias voltages above a certain threshold value (depending on the substrate material), a sharp drop appears in the  $I(z_{\text{appr}})$  curves, denoting the occurrence of an irreversible change in the junction (figure 3.6). At the moment the discontinuity occurs, the critical values of current  $I_{\text{dec}}$  and position  $z_{\text{dec}}$  can be retained. Both,  $I_{\text{dec}}$  and  $z_{\text{dec}}$ , depend on the applied sample bias  $V_S$ , as will be explained later.

After the current drop STM images reveal that the molecule is transformed into a feature typically  $\sim 1$  Å lower than before the event (figure 3.7 c and g) and the characteristic resonances of the fullerene icosahedral cavity have vanished from the corresponding STS spectrum<sup>4</sup> (figure 3.7 d and h). Thus, the discontinuous current drop is interpreted as a fingerprint of the fullerene cage's degradation. The precise way in which the  $C_{60}$  decomposes can not be determined in detail in our measurements. The effect is observed solely on the molecule selected for the tip approach, therefore an interpretation of the observed process as electron-induced polymerization with neighboring molecules can be excluded [50]. The degradation operation shows a high reproducibility, as is depicted in figure 3.8 for the case of  $C_{60}$  on Pb(111) and Cu(110). We can strongly discard that the fullerene

<sup>3</sup>Unless not states otherwise, e.g. figure 3.10.

<sup>4</sup>It should be noted, that decomposition is not the only possible process observed during tip approach. Especially rotations of the molecular orientation are known from other surfaces [48] and can often be found on Au(111). These events exhibit a similar tunnel current drop behavior as the decompositions do. They can be identified by inspection of the  $dI_t/dV_S$  spectra (no serious changes of the resonances are observed in these cases) and have to be excluded from the statistics.



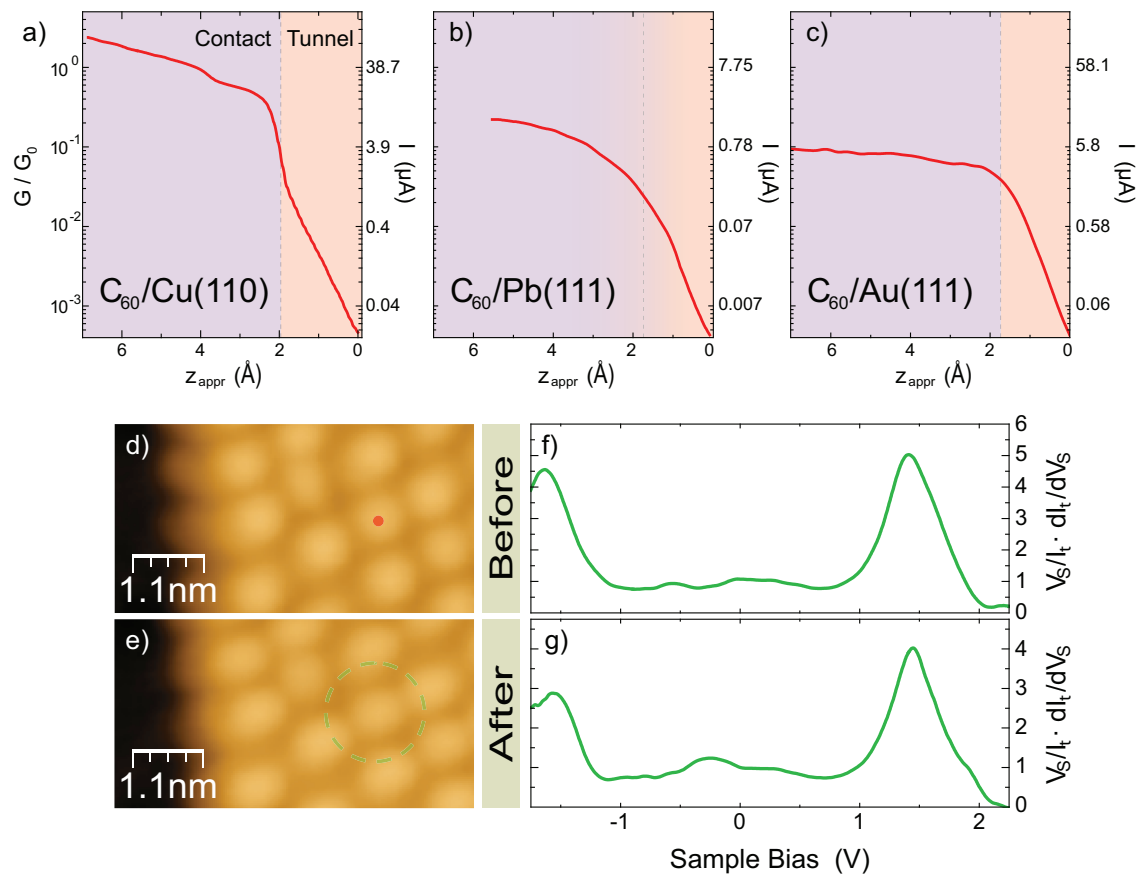


Figure 3.5: a–c): Conductance and current vs.  $z$ -distance plots taken on top of a C<sub>60</sub> molecule on Cu(110) (a), Pb(111) (b) and Au(111) (c). The conductance scale on the left of (a) accounts for all three graphs. The sample bias values are a):  $V_S = 0.5$  V, b):  $V_S = 0.1$  V, c):  $V_S = 0.75$  V. The purple (red) shaded areas indicates the contact (tunnel) regime. d) and e): STM images of C<sub>60</sub> molecules on Cu(110) before (d) and after (e) a contact formation (red dot) similar to the one shown in a). f) and g): normalized  $dI_t/dV_S$  curves of a C<sub>60</sub> molecule on Cu(110) before (f) and after (g) a contact formation similar to the one shown in a). After indentations with applied positive sample biases below a value of 0.6 V (Cu(110) and Pb(111)) or 1.2 V (Au(111)), the molecules show no signs of degradation.

cage is broken mechanically by the tip for two reasons: first, for high bias values the process takes place before a tip-molecule contact is formed (i.e. in the tunneling regime, compare figure 3.6 a) and second, because the molecule stays intact at indentations of more than 6  $\text{\AA}$  at low bias voltages (figure 3.5).

The literature reports decomposition temperatures of C<sub>60</sub> molecules to be in the range of 700 K to more than thousand K, depending on the adsorption state and material [51, 52, 53]. We assume that in our experiment the molecules are heated to temperatures in the

same order of magnitude. This implies a *heating efficiency*  $\gamma \approx 0.03$  to  $0.05$  K/nW. The next section will try to provide an intuitive picture, how the temperature accumulation inside the fullerene takes place.

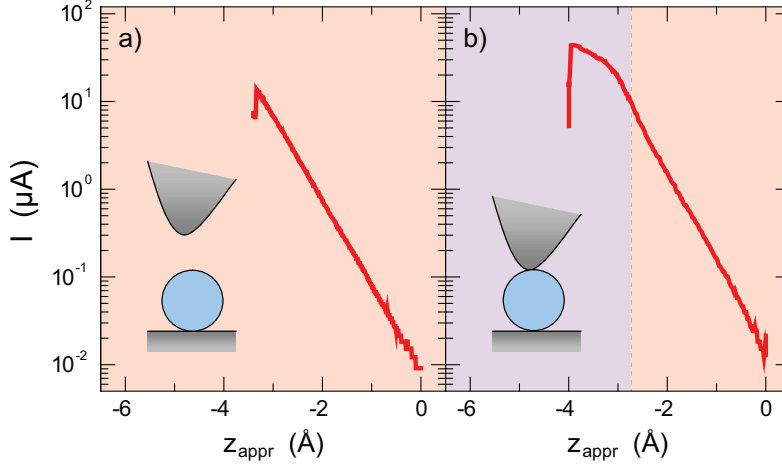


Figure 3.6:  $I(z_{\text{appr}})$  plots showing the molecular decomposition on Cu(110) in tunnel (a,  $V_S = 2.0$  V) and in contact (b,  $V_S = 1.0$  V) as sharp drops of the current. Similar curves are derived on Pb(111) and Au(111). Shaded areas mark the contact (purple) and tunnel (red) regime.

### 3.2.3 Statistical Character of $C_{60}$ Decomposition

In the following, we want to provide a simple model that visualizes the degradation process, i.e. the fission of one or more bonds of a  $C_{60}$  molecule. Generally we can state that the relevant degrees of freedom defining the atomic positions of the molecule (typically referred to as *reaction coordinates*) are stabilized in a minimum of the molecule's potential landscape. This confining potential is predominantly shaped by the chemical bonds between the atoms and has certainly some complex form, but it may be instructive to think of it as simple potential well that only depends on one reaction coordinate parameter (figure 3.9).

A  $C_{60}$  molecule exhibits 174 internal vibrational modes but we want to focus on the critical ones that contribute to the vibrational ladder climbing processes by which the energetically lowest potential barrier for decomposition can be overcome, what induces an irreversible breaking of the fullerene cage.

Every electron of the current flowing through the junction has a certain probability  $\Phi$  to excite such critical vibrational modes. A once created vibrational excitation (vibron) has an mean lifetime  $\tau_{\text{vib}}$  and will typically decay after a time in this order of magnitude. If multiple vibrons are excited within a timescale shorter than this mean lifetime, the

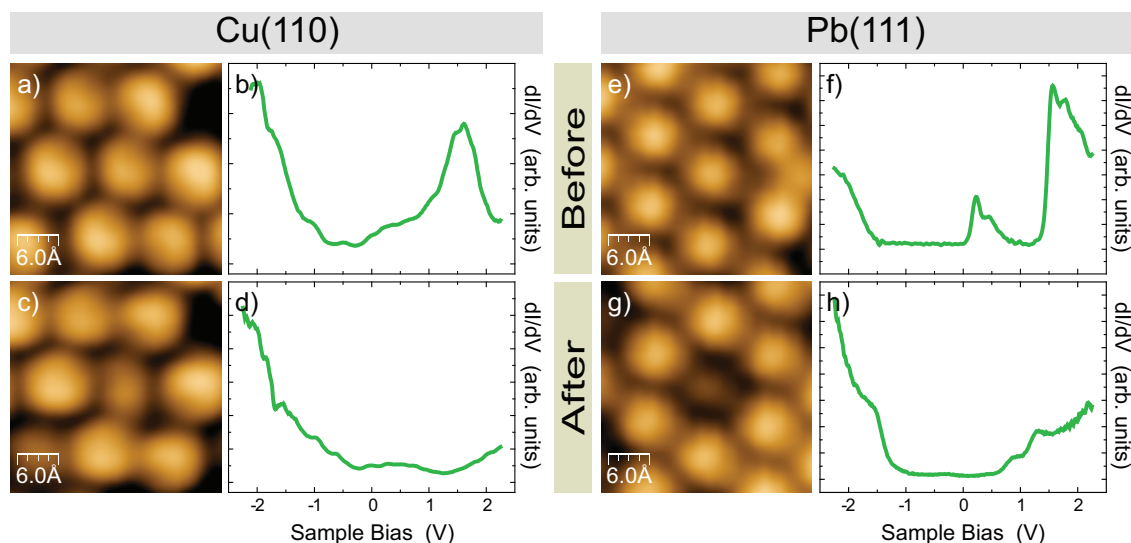


Figure 3.7: Molecular decomposition of  $C_{60}$  on a Cu(110) (a–d) and on a Pb(111) (e–h) surface. (a, b, e, f): STM images and  $dI_t/dV_S$  plots of an intact  $C_{60}$  (central molecule). (c, d, g, h): STM image and  $dI_t/dV_S$  plot after decomposition events on the central molecule and on molecules at the image border. A height difference of 0.6 Å (c) and 0.7 Å (g) and the disappearance of the characteristic LUMO and LUMO+1 resonances confirms the degradation of the  $C_{60}$  molecule. Feedback parameters: a, b)  $I_t = 1.0$  nA,  $V_S = 2.3$  V, c)  $I_t = 1.0$  nA,  $V_S = 2.0$  V, d)  $I_t = 1.0$  nA,  $V_S = 2.3$  V, e)  $I_t = 0.2$  nA,  $V_S = 0.5$  V, f)  $I_t = 1.0$  nA,  $V_S = 2.3$  V, g)  $I_t = 0.2$  nA,  $V_S = 2.3$  V, h)  $I_t = 1.0$  nA,  $V_S = 2.3$  V.

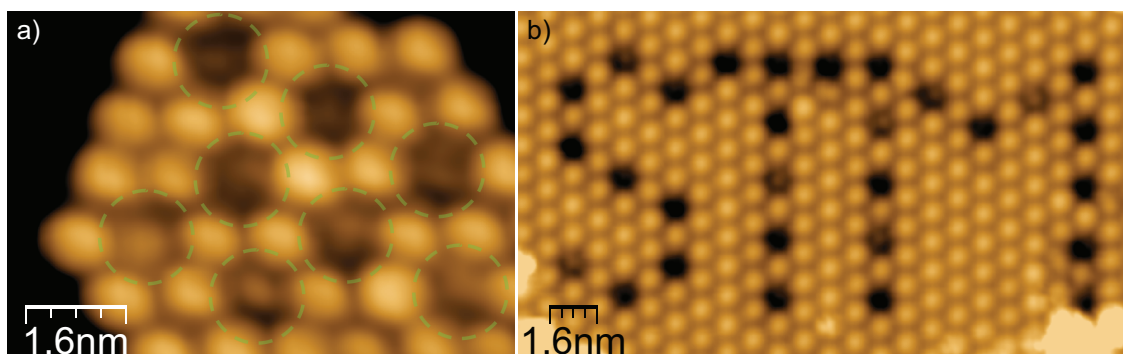


Figure 3.8: a) Image after a successive series of  $C_{60}$  decomposition manipulations (green circles) on Cu(110), that depicts the high reproducibility of the operation ( $I_t = 1.0$  nA,  $V_S = 2.3$  V). b) A similar series, used to write the letters ‘STM’ into an island on Pb(111) ( $I_t = 0.2$  nA,  $V_S = 0.5$  V).

system can “climb the ladder” of vibrational levels up to a point where it can escape the stabilizing potential (see figure 3.9). The critical parameter that defines how many single excitations are needed for this to happen is labeled as  $N$ . In our model, we will treat the

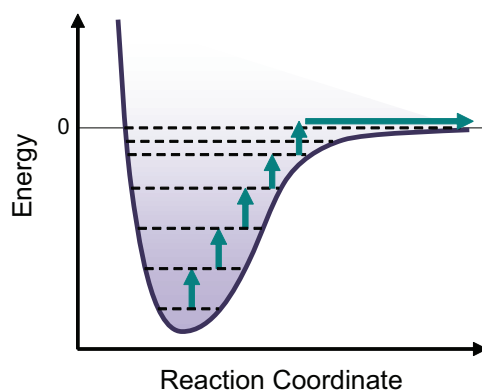


Figure 3.9: Scheme of a chemical binding potential with several vibrational levels. The reaction coordinate can be for example the distance between the atoms of a dimer molecule. A series of single-step excitations can be used to multi-excite the system, so it can escape the potential well (arrows). The system then degrades.

vibron excitation probability  $\Phi$ , the vibrational lifetime  $\tau_{\text{vib}}$ , and the critical number of excitations needed to degrade the model molecule  $N$  as fixed parameters of the system.

We can now model the molecular degradation process as the condition for the molecule to decompose, if  $N$  such critical vibrons are excited within a time span of  $\tau_{\text{vib}}$ , i.e. before the first excitation decays again. This comparatively simple definition can be used to calculate expectation values of  $I_{\text{dec}}$  and fit them to experimental results<sup>5</sup>. The mathematical details of this method are described in the appendix section A.3.

The most surprising consequence of the described decomposition definition is the dependence of the “microscopic” magnitude  $I_{\text{dec}}$  on the “macroscopic” tip approach speed  $\zeta$  (that is in the order of Å/s). If the decomposition current  $I_{\text{dec}}$  is measured once with a certain approach speed  $\zeta$  and then a second time with a  $\zeta$  ten times larger, the degradation will occur at a noticeably higher value of  $I_{\text{dec}}$  in the second experiment than in the first. The reason for this is based in the quantum mechanical character of the electron transport through the junction, i.e. in the fact that the moment one electron tunnels through the junction, and hence vibrons can get excited, is a fundamentally random observable. Therefore, the excitations occur in a random time series. For any fixed tunneling current  $I_t$ , the realization of the degradation criterion, i.e. of  $N$  excitations in a time span  $\tau_{\text{vib}}$ , will inevitably occur at a certain moment. The probability, and thus the average time span

<sup>5</sup>Due to its simplicity, the model implies a number of approximations. The first one is the assumption that the vibron excitation and deexcitation rates, and thus  $\Phi$  and  $\tau_{\text{vib}}$ , do not depend on the order of the excitation level of the system. Even for a simple harmonic oscillator potential this is not the case [54]. The second simplification is to neglect the statistical character of the vibrational deexcitation process and to assume instead that each vibration decays exactly after the time  $\tau_{\text{vib}}$ . However, the two approximations affect the model behavior only slightly, as described in more detail in appendix A.3, but they simplify the mathematical treatment of the problem to a large extend.

that is needed for the event to happen, depends strongly on the parameters: for smaller  $N$  or longer  $\tau_{\text{vib}}$  the realization probability for the event is larger and it is likely to happen earlier and vice versa. The probability of course also depends on the tunneling current. Under normal tunneling conditions, the realization of this condition is so unlikely that it will not be observed. But if the tip is approached towards the  $\text{C}_{60}$  molecule, the current increases gradually and so does the probability for decomposition. Now if the tip is approached at a low speed, the system has “more attempts” to fulfill the condition at each value of  $I_t$  than if  $\zeta$  is larger. Hereby, the time span of each attempt is  $\tau_{\text{vib}}$ , i.e. of the order of a vibrational excitation lifetime ( $\sim 10^{-13}$  s). Therefore a huge number of attempts can be undertaken every second. The condition will thus already be realized at a value  $I_t$  that provides a rather small probability for degradation. If the tip is now approached ten times faster, it will have a good chance to “rush” over the decomposition current value  $I_{\text{dec}}$  that was observed at the lower speed experiment, since the system has ten time less attempts at every  $I_t$  value. As a consequence, the degradation will be observed at a higher current value.

This approach speed dependence can be observed in the experiments: for the case of  $\text{C}_{60}$  on Pb(111) and a fixed sample bias  $V_s = 2.0$  V, the average decomposition current  $I_{\text{dec}}$  was measured for four different approach speeds  $\zeta$ . The resulting values of  $I_{\text{dec}}(\zeta)$  are plotted in figure 3.10 a). As it can be seen,  $I_{\text{dec}}(\zeta)$  obeys a *power law*. Values of  $I_{\text{dec}}$  that were calculated from the model described above were fitted to the graph (for details of the calculation see appendix A.3). For a fixed value of  $V_s$  the model depends on three critical parameters: the number of elementary vibrational excitations  $N$ , the mean lifetime of the critical vibrational mode(s)  $\tau_{\text{vib}}$  and the electron yield for inelastic scattering at the critical modes  $\Phi$ . The last two parameters cannot be separated in the model and appear as combined parameter  $\tau_{\text{eff}} = \tau_{\text{vib}} \cdot \Phi$ . From the fitting of the data the parameter  $N$  can be determined to be  $11 \pm 2$  electrons per decomposition. The value of  $\tau_{\text{eff}}$  is found to be  $2.7 \cdot 10^{-14}$  s. Due to a number of simplifications applied to the model, the resulting value of  $\tau_{\text{eff}}$  certainly deviates strongly from its real number, but we expect that its order of magnitude can be compared (see A.3). The exact value of  $\Phi$  for the applied sample bias is also not known, but an inelastic scattering yield of a few percent per mode can be taken as a rough number, as it was found in the IETS experiments measured around  $E_F$  in reference [24]. The estimation for the resulting vibron lifetimes is then in the order of picoseconds. This is a typical value for vibrational lifetimes of molecules that was also found in the numerical simulations of the system that are described in section 3.3.1 (see also figure 3.14).

Since the actual moment of degradation during the tip approach has a random character even at a fixed approach speed  $\zeta$ , as described above, every single decomposition experiment will give a different value of  $I_{\text{dec}}$ . For a given  $\zeta$ , the values of  $I_{\text{dec}}$  follow a distribution that can be derived from the model as well. In figure 3.10 b), the experimental distribution of  $I_{\text{dec}}$  is compared to the model distribution for a  $\zeta$  of 48 Å/s. The good accordance between measured and calculated distribution confirms the validity of the model.

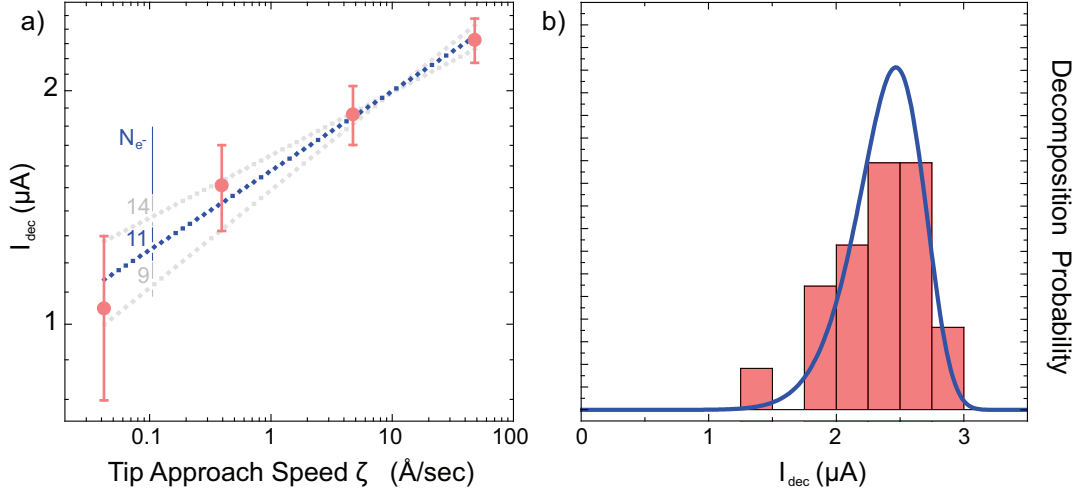


Figure 3.10: a) Measured values of the  $C_{60}$  decomposition current  $I_{\text{dec}}$  (red dots) on Pb(111) at a sample bias of  $V_S = 2.0$  V for different tip approach speeds  $\zeta$ . The blue line marks the best fit of the decomposition model described in the text with parameters  $N = 11$  and  $\tau_{\text{eff}} = 2.72 \cdot 10^{-14}$  s. The gray dashed lines are comparison calculations with  $N = 14$  and  $\tau_{\text{eff}} = 7.07 \cdot 10^{-14}$  s respectively  $N = 9$  and  $\tau_{\text{eff}} = 9.96 \cdot 10^{-15}$  s. All errors are  $2 \times$  standard error of the mean (SEM). b) Statistical distribution of the decomposition events with respect to the current  $I_{\text{dec}}$ : the red bars show the experimental data distribution in comparison with the model results (blue line). Width and shape of both distributions are in excellent agreement, indicating a high validity of the suggested model. Parameter values are as in a),  $\zeta = 48$  Å/s.

Summing up, the approach speed dependence of  $I_{\text{dec}}$  gives an insight into the dynamics of the excitation of vibrational modes of the system. From the large variations of  $I_{\text{dec}}$  for different approach speeds  $\zeta$  we conclude that the mode population at the moment of degradation is in a non-equilibrium state and that the energetic distribution of the vibrations during the experiment does *not* necessarily follow a Bose-Einstein statistics. The excitations occur in a short time span that does not allow a complete thermal redistribution. As stated earlier, the definition of the effective temperature  $T_m$  is therefore only based on the total energy of the vibrational modes in comparison with a real Bose-Einstein distribution.

### 3.3 Thermal Balance of the Molecular Junction

To gain more information about the dominating vibron excitation mechanisms, it is useful to analyze the dependence of the critical current for decomposition on the applied bias voltage. The corresponding graph of the statistical average of  $I_{\text{dec}}$  as a function of  $V_S$



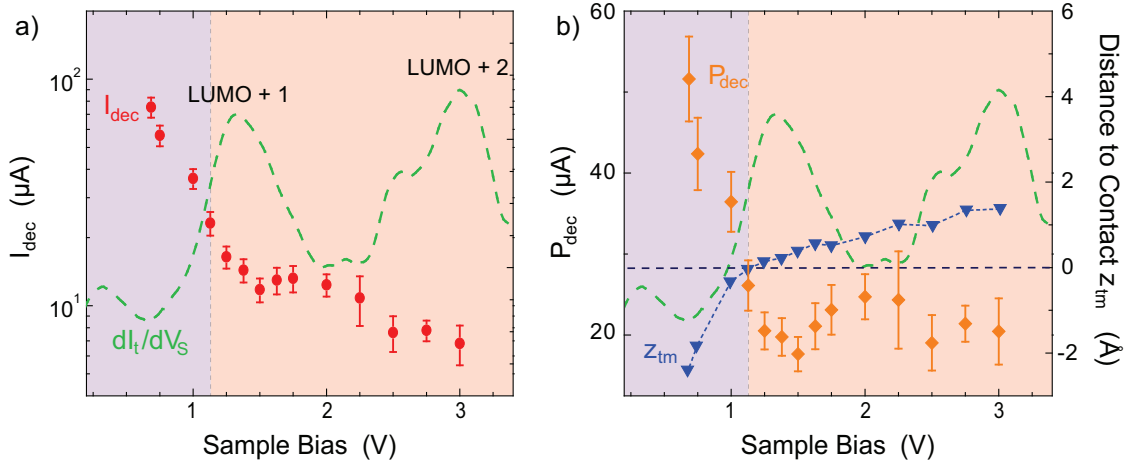


Figure 3.11: a): Statistical average of currents reached at the point of degradation  $I_{\text{dec}}$  vs. sample bias  $V_S$ . The statistics contain 180 events that were measured on fullerenes surrounded by unperturbed  $C_{60}$  molecules. b): Bias dependence of  $P_{\text{dec}}$  (orange diamonds) and of the distance to the contact position  $z_{\text{tm}}$  (blue triangles) (estimated as in figure 3.6; for events in the tunnel regime,  $z_{\text{tm}}$  is obtained by linear extrapolation). Shaded areas mark the contact (purple) and tunnel (red) regime. All error are  $2 \times \text{SEM}$ .

between 0.6 and 3.0 V is shown in figure 3.11 a) for the case of  $C_{60}$  on the Cu(110) surface. The general behavior exhibited by  $I_{\text{dec}}$  is a monotonous increase with decreasing bias: at the highest  $V_S$  values under investigation, 3.0 V, an electron current of 7  $\mu\text{A}$  is sufficient to activate the  $C_{60}$  decomposition, whereas a current of over 70  $\mu\text{A}$  is needed to produce the same result if the applied voltage is only 0.6 V. Looking closer, the  $I_{\text{dec}}$  curve can be divided into two distinct regimes: one region below 1.2 V that has a steeper slope and a flatter region above this voltage. Furthermore, two small plateaus are observed at 1.5 and 2.5 V, which cannot be attributed to statistical noise.

The two different regions observed in the  $I_{\text{dec}}(V_S)$  plot become more evident when we plot the power  $P_{\text{dec}}$  ( $P_{\text{dec}} = I_{\text{dec}} \times V_S$ ) applied to the  $C_{60}$  junction for its degradation (figure 3.11 b). In the regime above 1.2 V,  $P_{\text{dec}}$  keeps basically constant at 20  $\mu\text{W}$  and oscillates slightly around this value. The oscillations are connected to the plateaus formerly observed in  $I_{\text{dec}}$ . Below 1.2 V,  $P_{\text{dec}}$  increases sharply up to more than 50  $\mu\text{W}$  for the lowest bias value of 0.6 V. Similar plots for  $I_{\text{dec}}$  and  $P_{\text{dec}}$  were also observed on the other surfaces, Pb(111) and Au(111), but with significant differences, especially in the overall magnitude of the applied power (figure 3.15).

From the analysis of the corresponding tip approach curves  $I(z_{\text{appr}})$  we can get a first hint on the origin of the two regimes observed in  $I_{\text{dec}}$  and  $P_{\text{dec}}$ : whereas for voltages above 1.2 V all degradations occurred in the tunneling regime, at lower bias values, the tip is

in contact with the molecule at the point of decomposition. Figure 3.6 shows two of these events in different situations. The distance<sup>6</sup> between the tip and the molecule  $z_{\text{tm}}$  is superimposed to figure 3.11 b). As can be seen, the two different regions of degradation in tunnel ( $z_{\text{tm}} > 0 \text{ \AA}$ ) and in contact ( $z_{\text{tm}} < 0 \text{ \AA}$ ) correspond to the two regimes of different  $P_{\text{dec}}(V_{\text{S}})$  behavior, i.e. of constant decomposition power and of a steep slope of  $P_{\text{dec}}$ . This suggests a connection between the state of contact of the  $\text{C}_{60}$  molecule with the tip and the local effective temperature of the junction.

### 3.3.1 Molecular Heating and Cooling Mechanisms

For a certain set of current and bias values, the effective temperature of the molecule  $T_{\text{m}}$  depends on the balance between *heat generation* by inelastic scattering of electrons with vibrational modes and *heat dissipation* into the ‘cold’ electrodes [37, 55, 56]. In our case, both tip and sample are at 5 K. In general, the different mechanisms of heat generation and heat dissipation can be classified into two groups. The first group contains mechanisms that are *current driven*, like the heating by inelastic scattering of tunneling electrons. Theoretical simulations showed that the efficiency of this heating process is strongly enhanced if a molecular resonance is placed inside the transport energy window, because a larger number of vibronic levels is then accessible [55]. A related current-driven cooling mechanism is the *vibron assisted tunneling*, where a tunneling electron absorbs vibronic energy that is then transported into the metal cold bath [37, 57]. Both mechanisms, sketched in figure 3.12, take place when electrons tunnel resonantly through molecular resonances. The second class of thermal energy exchange processes occur on direct molecule-lead interactions. They contain the effects of molecular vibrons decaying into substrate phonons or into electron-hole pair excitations [37, 55, 57]. The first process is known to play a minor role in molecular cooling, since the energy band width of the metal phonons is typically one order of magnitude smaller than the vibron spectrum of a molecule and so few first-order transitions can take place. The second process dominates in metals and, hence, has more impact on the temperature regulation of the molecule. Both processes are independent of the transported electrons and are therefore static features of the system. It is now important to find out, which role the different mechanisms are playing in the investigated system.

Model transport calculations based on a nonequilibrium Green’s function formalism were performed by A. Pecchia and coworkers<sup>7</sup> [59] to simulate our results on the  $\text{C}_{60} / \text{Cu}(110)$  system [44]. For different static tip-molecule distances  $z_{\text{tm}}$  the effective molecular temperature  $T_{\text{m}}$  was calculated and plotted as a function of the applied bias in figure 3.13 a). For all distances, the achieved temperatures easily reached values of more than 1000 K.

<sup>6</sup>The zero-point of  $z_{\text{tm}}$  is defined as the position the point contact is established.

<sup>7</sup>In collaboration with the group of Thomas Frauenheim that provided density functional theory calculations of relaxed  $\text{C}_{60} / \text{surface slabs}$  [58].



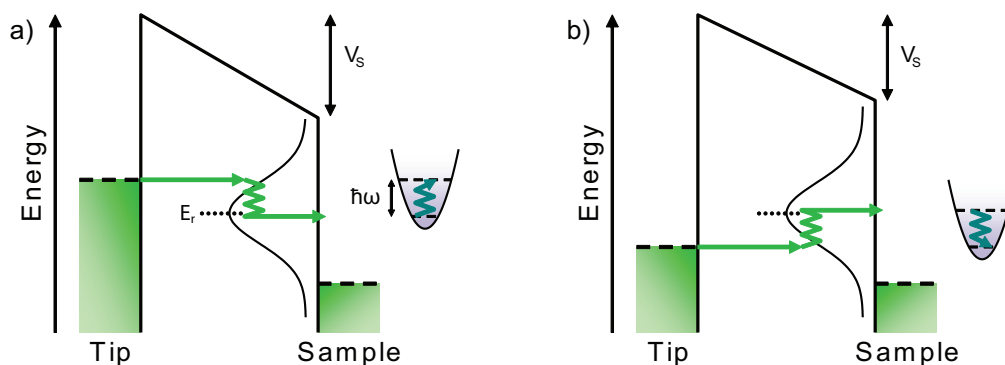


Figure 3.12: Schematic drawings of vibron interactions with tunneling current electrons for a molecule inside a tunnel junction: a) Inelastic electron-vibron scattering at a resonance level  $E_r$  heats the molecule; b) Vibron assisted tunneling is a cooling effect most effective for electron energies close to and below  $E_r$ .

The calculations find that only a comparably small fraction of electrons is scattered inelastically ( $\sim 10^{-3}$ ) and, hence, contribute to the heating of the  $C_{60}$  molecule. The general behavior of  $T_m$  is an increase with the simulated bias voltage. Interesting details of the characteristics of  $T_m$  can be seen around the numerical molecular resonances at 0.7, 1.5 and 3.0 eV above the Fermi level. When the tip's Fermi energy reaches the onset of a resonance, the temperature increase with  $V_s$  is reduced and can even become negative at higher states. This behavior is reversed at the point the actual resonance enters the transport window: now the increase of  $T_m$  gets enhanced until the resonance is far inside the window. The LUMO is the resonance that contributes most to the heating of the molecule. Reason and scale of this oscillatory behavior is given by the calculated  $C_{60}$  vibrational band of 200 meV width: an electron with an energy below the resonance can tunnel resonantly by absorption of a molecule's vibron (vibron assisted tunneling, shown in figure 3.12 b). It then carries the energy into the substrate thus contributing to a decrease of the molecular temperature. When the initial electron has more energy than is needed for a resonant tunneling process, it may deposit it by emission of one vibron into the molecule (figure 3.12 a). This effect heats the molecule most if the complete vibrational band is excited.

In order to reproduce the experimental curves of  $I_{dec}$  and  $P_{dec}$ , a critical value of the parameter  $T_m$  was chosen as decomposition temperature  $T_{dec}$ , allowing the extraction of a theoretical  $z_{dec}(V_s)$  curve. In a second step the curve  $I_{dec}(V_s)$  was constructed from simulated I-V characteristics. The value  $T_{dec}$  was adjusted to 1650 K to qualitatively fit the resulting curves of  $I_{dec}$  and  $P_{dec}$  to the experimental values. The calculated curves show a rapid increase for decreasing bias voltages below 1.2 V, where the tip is found to be in contact with the molecule. For bias values larger than 1.2 V, the decomposition appears in the tunnel regime. A steplike behavior around the resonances is obtained for  $I_{dec}$ , translating into oscillations of  $P_{dec}$  (see figure 3.13 b). These oscillations have their origin in

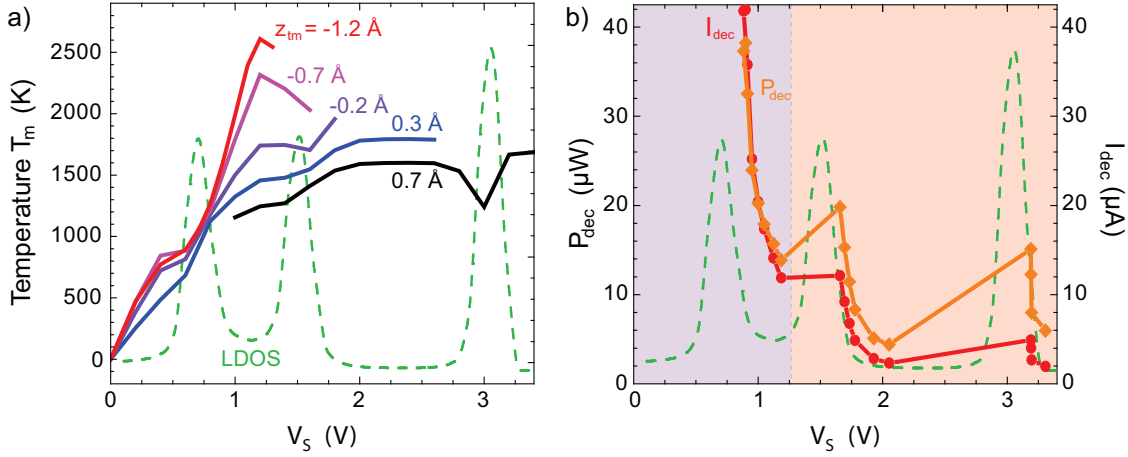


Figure 3.13: Results of the numerical simulation: a)  $T_m$  vs.  $V_s$  for the indicated distances to tip-molecule contact. The oscillations of  $T_m$  are associated with the numerical molecular resonances (green dashed line), as described in the text. b) The calculated values of  $I_{dec}$  (red dots) and  $P_{dec}$  (orange diamonds) are plotted for a critical temperature  $T_{dec}$  of 1650 K. Shaded areas mark the contact (purple) and tunnel (red) regime. The steps (oscillations) of  $I_{dec}$  ( $P_{dec}$ ) in the tunnel regime show similarities with the experiment. The steep increase of both curves in the contact regime can be explained by electron-hole pair emission into the STM tip lead.

the above explained enhanced cooling and heating below and above the resonances and resemble the experimentally observed features of  $P_{dec}$  at the LUMO+1 and LUMO + 2.

This, however, can not explain the very large increase of  $P_{dec}$  for sample bias below 1.2 V. Here, molecular decomposition is achieved once the tip is in contact with  $C_{60}$ . The tip-molecule contact enhances the dissipation of hot vibrons from the molecule into the tip. Since the STM current flows from the tip to the molecule, only the two cooling mechanisms of the second class described above can contribute to the effective absorption of energy from the fullerene: vibrational decay into substrate phonons and into electron-hole ( $e-h$ ) pair excitations. The performed calculations suggest that the former plays a small role in the cooling effects, what can be understood from the fact that the phonon band width at the leads (30 meV [60]) is much smaller and energetically separated from the vibrational spectrum of the  $C_{60}$  molecule (33 meV – 200 meV [61]). Hence, substrate phonons are expected to be primarily coupled to external modes of molecular motion with respect to the surface, that do not contribute to the decomposition of the fullerene cage. This is nicely reflected in the different broadening of the energy levels of the vibrational modes that is found in the calculated vibrational DOS spectrum of  $C_{60}$  on Cu(110) (figure 3.14). Vibrational modes with an energy  $\hbar\omega$  within the range of the substrate's phonon band experience a considerable lifetime reduction and thus level broadening due to the

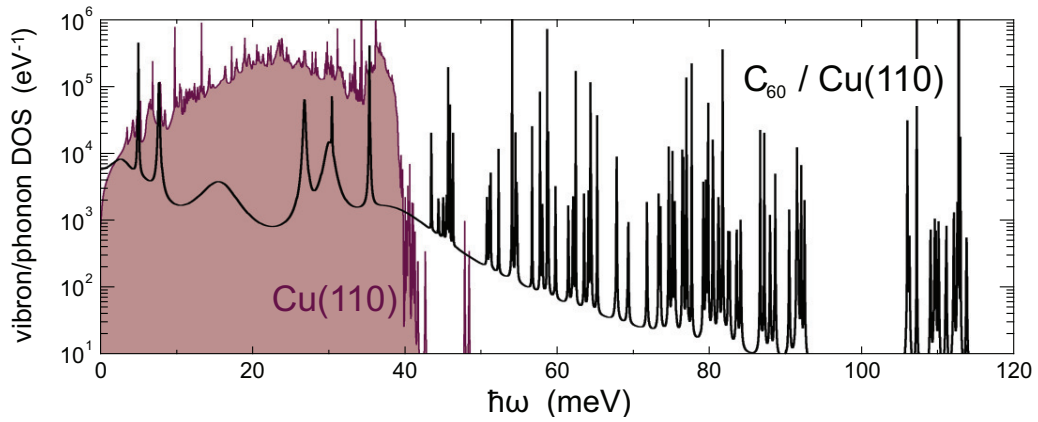


Figure 3.14: Calculated density of states of vibrational modes of  $C_{60}$  on Cu(110) (black line) and of the Cu(110) substrate phonons (purple line). The  $C_{60}$  modes show a considerably higher lifetime broadening if their energy lies within the range of the substrate phonon band (red shaded area). The reason is their ability to decay into the phonon band by a first order process. Source of figure: [63].

fact that they can easily decay into phonons of the substrate. The calculated vibrational modes of the molecule with higher energy show a small level broadening, demonstrating that they hardly decay by this channel.

Instead, the main cooling mechanism on metal surfaces is the  $e-h$  excitation in the leads [62]. The calculations evidence that the sharp increase of  $I_{dec}$  and  $P_{dec}$  below 1.2 eV vanishes if the  $e-h$  excitation into the tip is suppressed artificially. Thus, the vibrational cooling upon contact formation (*tip cooling*) can explain the characteristics of the curves in contact. For bias voltages below 0.6 V, the LUMO resonance starts to be removed from the conduction window, leading to a reduced heating of the molecule (see figure 3.13). This is the reason why the thermal decomposition could not be achieved in this range.

### 3.3.2 Influence of the Substrate Metal

The decomposition power  $P_{dec}$  is plotted for the three different metal substrates in figure 3.15. The curves on all surfaces, Cu(110), Pb(111), and Au(111), show the typical division into the steep slope region of the contact regime and the roughly constant behavior in tunnel. The most striking difference between the curves are the absolute values of  $P_{dec}$ : while  $C_{60}$  can withstand electric powers of several tens of microwatts on Cu(110), this value is one order of magnitude lower on Pb(111) and on Au(111).

Qualitatively, the decomposition power on Pb(111) and Au(111) performs oscillations around the molecular resonance positions as it was already found on Cu(110). A magnification of the tunnel regime part of  $P_{dec}$  for all three surfaces superimposed by corre-

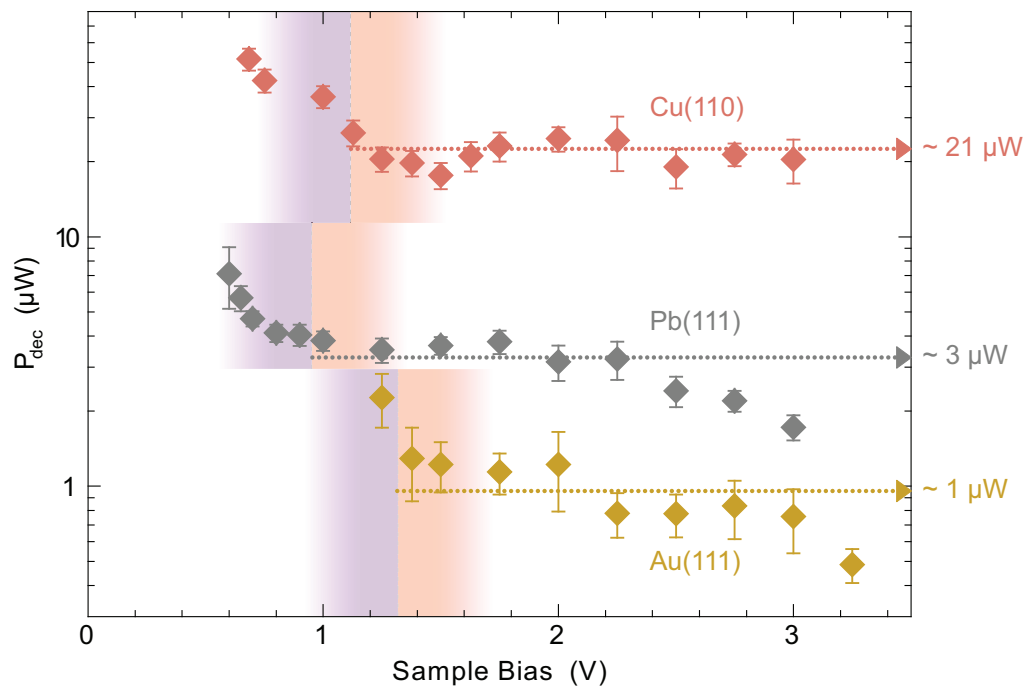


Figure 3.15: Decomposition power spectrum of  $C_{60}$  on three different surfaces: Cu(110) (red), Pb(111) (gray) and Au(111) (yellow). The total number of recorded events are: 152 on Cu(110), 150 on Pb(111) and 105 on Au(111). The average value for the points in the tunnel regime of each data group is marked by the dashed arrows and noted on the right. The border between contact and tunnel regime is marked by the shaded broad vertical lines.

sponding  $dI_t/dV_S$  curves is once more presented in figure 3.16. The oscillating features of  $P_{dec}$  are found at the positions of the LUMO+1 on all materials and at the LUMO+2 positions of Cu(110) and (less articulate) of Pb(111)<sup>8</sup>. So, the discussed mechanisms of most efficient vibron absorption and emission below and above the resonance by the tunneling electrons can also consistently be observed on these surfaces.

The average power  $\bar{P}_{dec}$  for degrading the  $C_{60}$  molecule in the tunnel region depends strongly on the metal surface used:  $\bar{P}_{dec} \sim 21 \mu\text{W}$  on Cu(110),  $\bar{P}_{dec} \sim 3.1 \mu\text{W}$  on Pb(111), and  $\bar{P}_{dec} \sim 1.0 \mu\text{W}$  on Au(111). We can expect that the heat generation, that depends on electron-phonon coupling of the tunneling electrons to the  $C_{60}$  vibrational modes, does not vary a lot on the three surfaces. Therefore, the differences of  $\bar{P}_{dec}$  originate in the different heat dissipation capabilities. Since  $e-h$  pair creation is the most important non-current-driven energy dissipation process, it would stand to reason that the observed tendency

<sup>8</sup>On Pb(111) the LUMO + 1 resonance is found to be split into two peaks at 1.5 V and at 1.8 V. The position of the  $P_{dec}$  step at 1.8 V on Pb in figure 3.16 is therefore probably due to the high energetic component of this resonance.

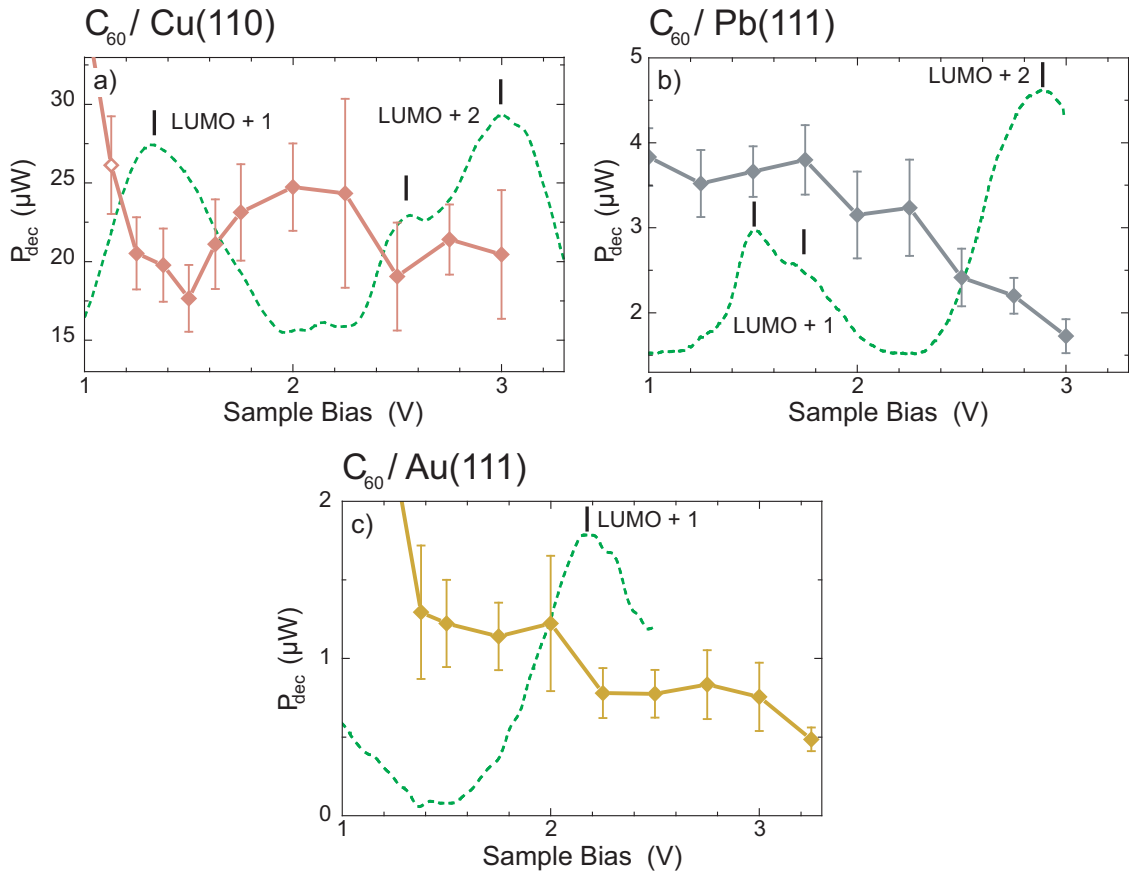


Figure 3.16: Decomposition spectrum  $P_{\text{dec}}$  of  $\text{C}_{60}$  in the tunneling regime on (a) Cu(110), (b) Pb(111), and (c) Au(111). Dashed green lines are the respective normalized  $dI/dV_S$  curves (Cu:  $R_{\text{junc}} = 0.9 \text{ G}\Omega$ , Pb:  $R_{\text{junc}} = 0.7 \text{ G}\Omega$ , Au:  $R_{\text{junc}} = 0.3 \text{ G}\Omega$ ). Molecular resonances are marked by vertical bars. The  $P_{\text{dec}}$  plots show oscillating behavior around the energies of the molecular resonances. All errors are  $2 \times \text{SEM}$ .

can be explained by this mechanism. One critical material property that influences the efficiency of such a process is the density of states (DOS) at  $E_F$ . Yet, this bare surface parameter fails to explain the observed sequence (Cu, Pb, Au): while the DOS at  $E_F$  of Cu(110) indeed has the highest value of the three, this criterion would place Au(111) into a second position and finalize with Pb(111)<sup>9</sup>. On the other hand, the efficiency of  $e-h$  pair creation is also known to be affected by the presence of a molecular resonance at the Fermi level [67]. If we consider the occupation of the LUMO of the  $\text{C}_{60}$  molecule as controlling parameter of the cooling efficiency, the correct order of the observed values of  $\bar{P}_{\text{dec}}$  on the three substrates is restored: the  $dI/dV_S$  plots in figure 3.17 a–c) depict the

<sup>9</sup>Density of surface states are approximately  $0.017$  and  $0.0105 \text{ (eV } \text{\AA}^2)^{-1}$ , for Cu(110) and Au(111), respectively [33, 64, 65]. The bulk DOS at  $E_F$  is:  $\text{DOS}_{\text{Pb}}(E_F) = 0.0166 \text{ (eV } \text{\AA}^3)^{-1}$ ,  $\text{DOS}_{\text{Au}}(E_F) = 0.0173 \text{ (eV } \text{\AA}^3)^{-1}$ ,  $\text{DOS}_{\text{Cu}}(E_F) = 0.025 \text{ (eV } \text{\AA}^3)^{-1}$  [66].

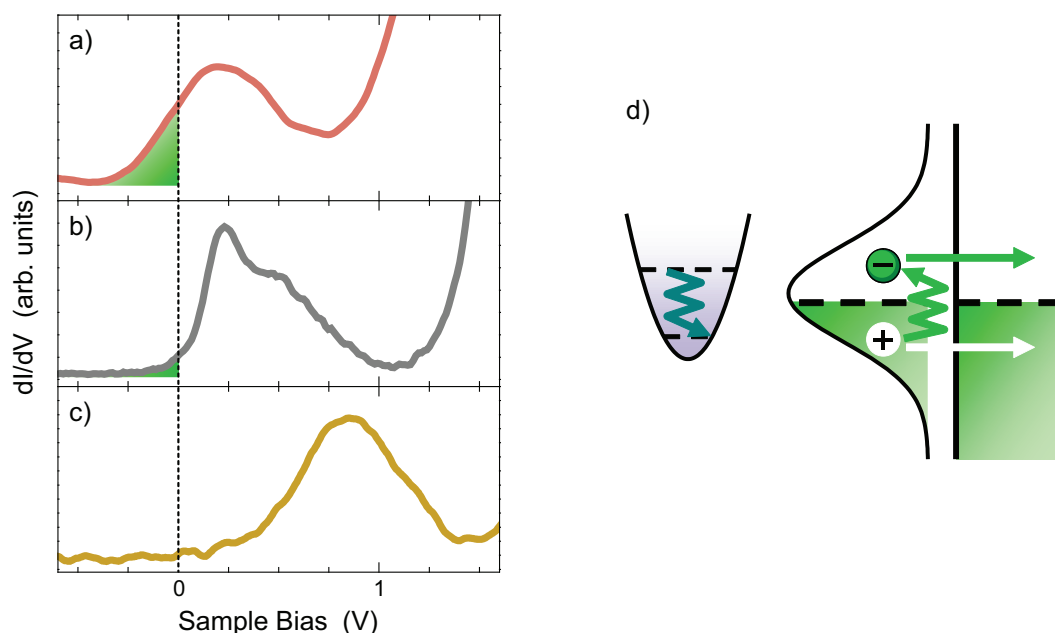


Figure 3.17: a–c): Magnification of the  $dI/dV_S$  curves of 3.4 (a–c) showing the LUMO of  $C_{60}$  on Cu(110) (a), Pb(111) (b) and Au(111) (c). The occupied portions of the LUMO peaks are marked as green shaded areas. A decreasing amount of electron transfer into the molecule can be expected for Cu(110) to Pb(111) to Au(111). d): Schematic drawing of the proposed mechanism of vibron decay by electron-hole-pair creation close to a partially occupied molecular resonance. The decay probability is increased by the the alignment of the molecular resonance close to the Fermi level [67]. The  $e-h$  pairs created at the molecule-metal interface leave into the metal before they recombine.

different alignment of the LUMO resonances with respect to  $E_F$  on the three surfaces and the resulting amount of charge transfer into the molecule. The molecular DOS at  $E_F$  is largest on the Cu surface, where a charge of more than one electron is transferred into the molecule [68]. On the Pb surface, a small part of the tail of the LUMO peak is in the occupied region while on Au the occupation of this resonance is negligible.

This finding allows us to draw a qualitative picture, in which the charge transfer from the metal into the molecules causes an increase of the density of molecular states around  $E_F$ . This enhances dissipative channels, mediated by the generation of  $e-h$  pairs at the molecule-surface interface, that are then reflected back into the metal where they can recombine (figure 3.17 d) [67]. The rate of heat dissipation thus increases with the charge transfer, what results in a reduction of the molecular temperature and causes that a larger power is required to thermally degrade the molecules. Ignoring additional mechanisms like hybridization of metallic and molecular states, which could also have an effect on the dissipation of vibrational energy, our results hint that a molecule in contact with a metal electrode can sustain larger current densities if it experiences a larger charge transfer.

### 3.4 Conclusion

In this chapter, the current induced degradation of single  $C_{60}$  molecules by STM was used as a novel approach to gain insight into the sparsely explored field of local temperature evolution in electronic transport junctions. The thermal decomposition process of the fullerene molecules in monolayer islands, that was characterized on three different metal surfaces, was used to draw a thorough picture of different mechanisms that are involved in the temperature regulation of these junctions.

Thermal degradation events of adsorbed  $C_{60}$  molecules can be excited by gradually increasing the electron tunneling current flowing through a single molecule, what is realized by a continuous approach of the STM tip. On Cu(110), the molecules are found to degrade at an average current value of 20  $\mu A$  (3  $\mu A$  on Pb(111) and 0.6  $\mu A$  on Au(111)). The degradation effect is characterized by a considerable modification of the molecule's appearance in the STM images and by a change of the local electronic states, especially the disappearance of the LUMO.

The heating process can be understood as inelastic scattering of tunneling electrons with molecular vibrational modes by electron-phonon coupling interactions, typically mentioned as *vibrational heating* in the literature. The energy accumulation itself is hereby a statistically fluctuating process of excitations and deexcitations of internal vibrational modes. The overcoming of a barrier in the molecular potential triggers the decomposition process. We found that an average of 11 single electron excitations is needed to decompose one molecule on Pb(111) at a sample bias of 2.0 V. The lifetime of a single vibrational excitation determines the efficiency of this process.

The total power of the tunneling current needed to degrade the molecules was found to depend on the state of the junction (tunnel or contact), on the applied sample bias, and on the substrate material. These observed variations of the decomposition power are attributed to differences in the heating efficiencies  $\gamma$  of the systems. The heat accumulation properties, and thus the temperatures, of the current conducting molecular systems depend on the balancing of the vibrational heating process and the different energy dissipation mechanisms. The two most important cooling effects are hereby the *vibron assisted electron tunneling* and the  *$e-h$  pair creation* process.

We find that the critical tunneling current  $I_{dec}$  that is needed to decompose the molecule varies with the applied sample bias  $V_S$ . In a naive picture, where every electron with an energy high enough to excite internal vibrational modes contributes equally to the heat accumulation, this would not be the case. Instead, a dependence on the energies of the electrons enters the system via the vibron excitation rates and the rates for the opposite process, the vibron decay into excitation of the tunneling electrons. In both processes, electrons with an energy close to a resonance state have a higher tunnel probability due to additional channels that include the emission or absorption of a molecular vibrons.



The enhancement of inelastic scattering leads to a total heating efficiency that varies with the applied bias around the resonance states, explaining the observed oscillations of the decomposition power  $P_{\text{dec}}$  at these positions. This picture is confirmed by theoretical simulations that show a high degree of agreement with the experimental data.

The  $\text{C}_{60}$  molecules on Cu(110) show a remarkably high thermal stability to withstand electrical powers of up to  $50 \mu\text{W}$ . Their observed heating efficiency  $\gamma$  is by far the smallest found in this study. For the system  $\text{C}_{60}/\text{Pb}(111)$ , the heating efficiency is six times larger and for  $\text{C}_{60}/\text{Au}(111)$  it is over 20 times larger than on copper. We can ascribe these large differences to the important cooling process of  $e$ - $h$  pair emission, which is strongly affected by the alignment of molecular resonances with respect to the Fermi level. On copper, the high amount of charge transfer into the molecule enhances the  $e$ - $h$  creation and demonstrates the importance of this process.

To increase the thermal stability of current-conducting nanoscopic systems in a potential future application, a focus must be set on the electronic and on the geometric properties of the system. A smaller number of resonance states inside the conduction window and a high density of states at the Fermi level can considerably increase the thermal stability, although these demands may be in conflict with the functional properties of the intended device. An alternative strategy may be the increased contact with the metallic “cold bath”, e.g. the contacts. The exemplary *tip cooling* situation, found in our experiments when a tip-molecule contact is formed, proves the efficiency of this method. In combination with an enhanced  $e$ - $h$  pair emission, this effect can lead to the extraordinary stability found for  $\text{C}_{60}$  on copper that was probed with voltages below 1 V.

The molecular decomposition may of course also be used as a functional element by a potential application, e.g. as temperature or current detecting mechanism or for a nanoscopic fuse. In this case, the described effects of heating and cooling and their dependencies on the various parameters can be used for tuning the degradation currents to required values.



## Chapter 4

# Chemical Conversion of Adsorbed Photoswitches

The observed bond breaking of a single C<sub>60</sub> molecule shows two major drawbacks for the use in potential future applications. The first one is that the process is not reversible. The option to reset the system to its initial state would be a huge advantage for many applications. The second drawback is that the exact chemical details of the induced molecular structure are unknown and possibly vary from molecule to molecule. Therefore difficulties may arise if the chemical reaction should be used to apply defined changes of a certain functionality of the molecules. Both problems can be faced by choosing an appropriate molecule to induce reversible chemical conversions. Our approach is the use of *molecular switches*, i.e. of molecules that possess two or more isomeric states that differ in chemical and/or geometrical configuration and that allow a reversible transformation between them. These states are separated by an activation barrier which can usually be overcome by photon, electron or temperature induced excitations. While many switches are well characterized in gas phase and solution, their switching properties on a surface may change drastically, but are still largely unresolved. *Photo switches* are especially in our focus of interest since their switching mechanism involves electronic excitations by the photon field. Inside an STM junction there is a good chance that similar excitations can be obtained by the attachment or detachment of tunneling electrons and that these excitations may trigger a comparable switching reaction. In many cases the changes of the switching states are accompanied by a change of certain functionalities as e.g. light absorption properties, conductivity or dipole moment. This fact may be used in further applications.

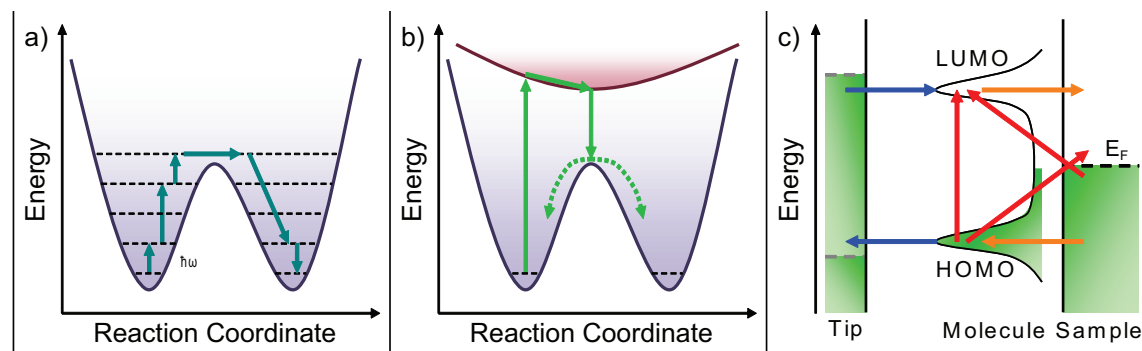


Figure 4.1: Schemes of molecular switching mechanisms. a): Transition between two conformational states (the two minima of the reaction coordinate potential, blue line) by successive vibron excitations. b): Possible transition involving an electronically excited molecular state (red potential curve): the shape of the excited state potential drives the system into either one of the two conformations. c): Overview over the expected mechanisms for obtaining an electronically excited state of the molecule and the ways for quenching: blue arrows represent the electron/hole excitation of the LUMO/HOMO by the STM tip; red arrows show the possible transitions of electrons excited by light irradiation. Orange arrows show electron deexcitation paths into the substrate.

## 4.1 Excitation Mechanisms

The potential energy landscape of a molecular switch is generally characterized by multiple minima defining the switching states that are separated by potential barriers. In the experiments of the last chapter, the modification of the chemical structure of a single C<sub>60</sub> molecule was induced by the excitation of atomic vibrations (see figure 4.1 a). Other ways to overcome the potential barrier between two conformational states of a photo switching molecule are given by changing the occupation state of the molecule's electronic levels [30]. In its anionic, cationic or neutral electronically excited state, the potential energy landscape of the molecule can exhibit a different shape than in the ground state. If the excitation lifetime is long enough, the system can evolve in this excited state's potential. Depending on the actual potential pathway, this evolution can drive the system into a position, where, after deexcitation, it has a high probability to access another conformational state [69, 70] (figure 4.1 b). For a molecule on a metallic surface, there are two ways to induce these electronically excited states in our experiment: by adding/removing of electrons into the LUMO/from the HOMO by the STM tip or via photon absorption processes (figure 4.1 c). The latter can either induce an *intramolecular electronic excitation* or it can excite electrons from the substrate into the LUMO or from the HOMO into free states of the metal. The rate of switching reactions is therefore limited by the efficiency of these mechanisms to create the required excitations, i.e. by the electron tunneling rate or by the photon absorption cross section.

The switching yields are also reduced by the coupling to the substrate: electronic deexcitations into the metal in a timescale shorter than the average time required for the switching process reduce the efficiency [71]. Additionally, a strong binding of one switching configuration can severely deform the potential energy surface and thus quench the switching procedure. An appropriate choice of the substrate is therefore fundamental for the examination of reversible molecular switching processes on surfaces.

Following this, we end up with three distinct experimental ways to stimulate a transition of the adsorbed switches. Heating of the sample induces vibrational excitations that may switch the molecules. Experimental methods quantifying rates of thermally induced transitions provide information about the height of the potential switching barrier. Therefore, a Boltzmann statistical vibron distribution is assumed in the molecule, as discussed in more detail in the corresponding paragraph. The second way to induce a switching is given by the illumination with light. Up to now only few systems of surface adsorbed molecules are reported to conformationally switch upon light exposure [72, 73, 74, 75]. Reasons for the hindering of the switching can be a reduction of the effective transition dipole moment on the surface (including parallel alignment), fast electron decay into the substrate [71] or a severe deformation of the reaction potential due to the strong binding of one switching conformation to its environment [75]. For a photo-switchable molecular system, the measurement of the switching yield in dependence of the photon energy can give detailed information about the observed switching mechanism. The same holds for the yield of switching induced by tunneling electrons, the third experimental way to induce the molecular transformations [69, 76, 77, 78, 79]. It should be noted that beside the above mentioned switching mechanisms involving vibrational or electronic excitations switching processes can also be induced by strong static electric fields, as can be found in an STM junction [76].

In cooperation with the collaborating groups of the Sonderforschungsbereich (Sfb) 658 “Elementarprozesse in molekularen Schaltern an Oberflächen”, our motivation is to study the different mechanisms of conformational switching of a molecular photo switch on a metal surface and to gain closer insight into the details of the switching reaction and into the role of molecule-surface interactions.

## 4.2 The Spiropyran Molecule

Our molecule of choice is the 1,3,3-Trimethylindolino-6'-nitrobenzopyrylospiran (*spiropyran*, SP). The molecule can undergo a thermally and optically induced reversible configurational change into the isomeric *merocyanine* (MC) form. The Lewis formulas of the species are shown in figure 4.2. A number of structural and functional differences between the two forms make these molecules interesting for various applications. While spiropyran molecules are three dimensional, inert, and colorless, the merocyanine iso-

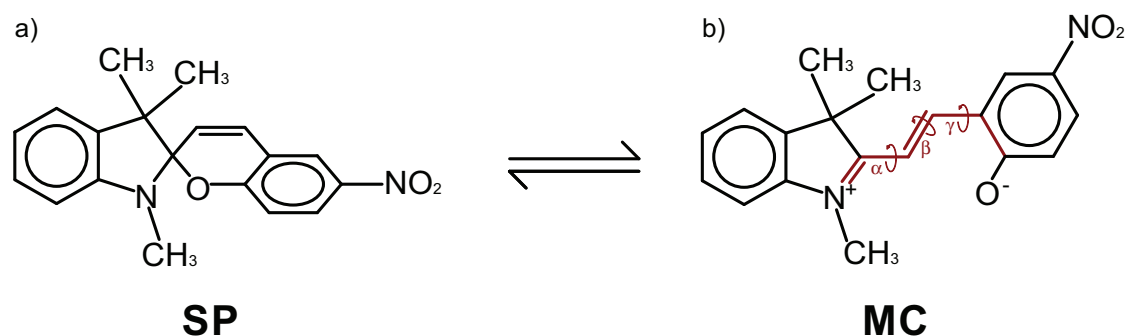


Figure 4.2: Structure of 1,3,3-Trimethylindolino-6-nitrobenzopyrylospiran (SP) and one of its merocyanine (MC) zwitterionic isomers (TTC). While SP is chiral and possesses two halves with orthogonal planes, the conjugated MC form is planar and prochiral. The four MC rotamers given by the two possible rotations of the phenolate and the indole groups are labeled after the *trans* (T) or *cis* (C) state of the torsional angles  $\alpha$ ,  $\beta$  and  $\gamma$  along the bonds marked red. On the metal surface, each of the four conformations is expected to appear indistinctly under its two chiral forms.



Figure 4.3: The molecules that form the basis of the two main groups of the spiropyran molecule are indoline (a) and nitrobenzopyran (b). In the merocyanine isomer, the bonding state of the indoline's nitrogen atom resembles more the situation in an indole molecule (c), where conjugated double bonds are formed to the neighboring carbon atoms.

mers are planar, chemically highly active, conjugated, and colored. The merocyanine compound is a resonance hybrid between a neutral form (quinonoid) and a zwitterion [80]. The latter one exhibits a strong dipole moment. The large change of molecular properties poses a great interest in the use of these molecules to form parts of sensors and detectors [81], to perform logic operations in molecule-based devices [82, 83] or to induce reversible changes of chemical or optical properties of organic-inorganic interfaces [84].

The spiropyran molecule consists of two major groups, that are build up from the molecules *indoline* and *nitrobenzopyran* (figure 4.3 a and b). We will use this notation

to distinguish between the two different nitrogen atoms. If the molecule is isomerized to its merocyanine form, the character of the indoline's nitrogen atom is changed by the participation in a conjugated  $\pi$ -bonding system. It then resembles more the case of an *indole* molecule (figure 4.3 c), and can accumulate positive charge by releasing one electron into the conjugated system.

The conformational difference between the two species is given by the C-O bond of the SP molecules that is not present in the merocyanines. Quantum chemical calculations show that the conversion process of a free or solved SP into its MC form starts with the fission of the C-O bond, followed by two unfolding steps until the flat MC molecule is reached [85, 86]. The initial bond fission has the highest activation barrier of all reaction steps, what makes it the rate-determining process. Experimental values for this energy barrier height range between 0.9 eV and 1.2 eV, depending on the solvent [87, 88]. The lowest barriers are reported for non-polar solvents, so the barrier of a free molecule can be estimated in this order. The successive steps after bond cleavage are rotations of the molecular groups around the torsional angles  $\alpha$  and  $\beta$  of the C-C double bonds until the merocyanine molecule ends up in its ground state, the planar TTC rotamer (for nomenclature see caption of figure 4.2). The activation barrier for the back-reaction is reported to be  $\approx 90\%$  of the SP  $\rightarrow$  MC reaction's barrier in propanol and ethanol [88, 89].

The SP  $\rightarrow$  MC coloration process for free or solved molecules can be activated by UV illumination. In most solvents, SP has two absorption peaks, a larger one at around 245 nm and a smaller one around 345 nm. MC molecules show a large absorption peak at 560 – 600 nm [87]. Illumination with this wavelength or with UV light can trigger the decolorating MC  $\rightarrow$  SP back-reaction process. The longer absorption wavelength of the MC molecules is attributed to their extended conjugated  $\pi$ -electron system. In addition to their different photochemical activity, the two isomers can also be switched by thermal activation. In solution at room temperature this results in thermal SP  $\rightleftharpoons$  MC equilibrium of the two species with an MC/SP ratio increasing with the solvent's polarity [90].

To incorporate the molecular functionality into functional devices, it is important to understand how such a thermodynamic equilibrium is affected when the molecules are condensed into structurally ordered films on top of a surface [91, 92]. It is known that the interaction with a metal surface is capable of modifying the equilibrium structure of molecular conformational switches [77, 93, 94]. Even a chemically inert substrate like gold is active enough to influence the molecular conformation by interacting non-covalently with conjugated molecular species [69]. Spiropyran molecules are known to form ordered structures on a Au(111) surface [95, 96], but no stable phases of the open isomer have been reported.

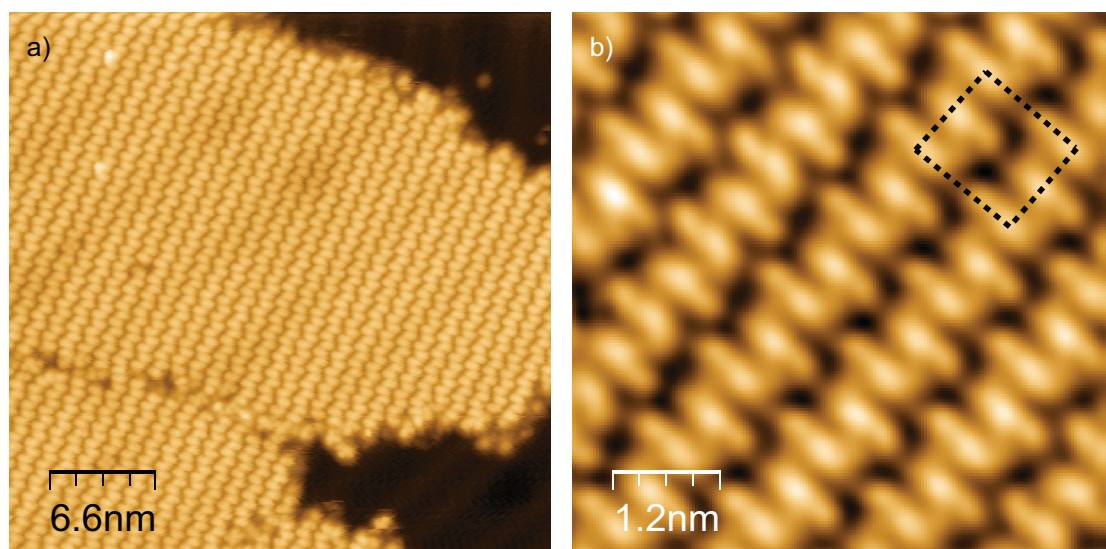


Figure 4.4: a): STM image of an adsorbate-covered Au(111) surface annealed to  $T_{\text{ann}} \sim 240$  K. The height of the molecular islands oscillates around  $0.3 \pm 0.1$  nm depending on the applied sample bias. b): High resolution STM image showing the alternating alignment of molecules along rows and their intramolecular chiral structure. The unit cell indicated as a dashed rectangle amounts to  $1.2 \times 1.1$  nm<sup>2</sup> ( $I_t = 4.0$  pA,  $V_s = 1.0$  V).

### 4.3 Spiropyran on Au(111)

Atomically clean (111)-oriented Au single crystals, prepared using standard sputtering-annealing methods, were used as substrate. In all experiments described, a submonolayer of commercially available 1,3,3-Trimethylindolino-6-nitrobenzopyrrolospiran molecules was first deposited in UHV on the cold metal substrate ( $T < 150$  K) by warming a custom-made Knudsen cell containing the crystalline spiropyran powder to  $\sim 380$  K. The adsorbate-covered surface was then annealed up to the desired temperature  $T_{\text{ann}}$  and, unless otherwise specified, further cooled down back to the lowest possible temperature for its inspection.

First we study the structure of the different molecular phases prepared at a gradually increasing temperature using scanning tunneling microscopy. A molecular layer of SP deposited on a cold Au(111) surface undergoes an ordering transition at  $T_{\text{ann}} \sim 220$  K leading to the formation of extended self-assembled domains. STM images of the adsorbate-covered surface annealed above this temperature resolve that the islands are composed of molecular rows (figure 4.4 a) along which the molecules alternate their orientation (figure 4.4 b). In spite of such an anisotropic structure, the domains show an overall rounded shape, suggesting that intermolecular interactions within the layer are of similar strength both along and across the molecular rows. The observation of the unperturbed Au(111)



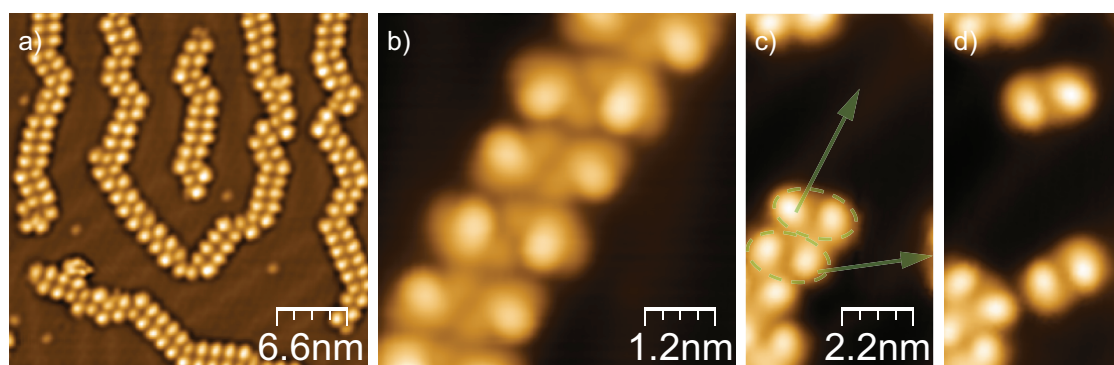


Figure 4.5: a): STM image of an adsorbate-covered Au(111) surface after annealing to temperatures above  $T_{\text{ann}} \sim 300$  K ( $I_t = 20$  pA,  $V_S = 1.1$  V). b): High resolution STM image of the molecular chains showing that the molecular species exhibit an intramolecular pattern composed of a 0.1 nm high planar oval structure with a 0.25 nm high internal lobe ( $I_t = 50$  pA,  $V_S = 1.0$  V). c): STM image of the end of a molecular chain with the arrows indicating lateral manipulation experiments with the STM tip. d): Consecutive STM image showing the manipulated molecular dimers separated from the chain.

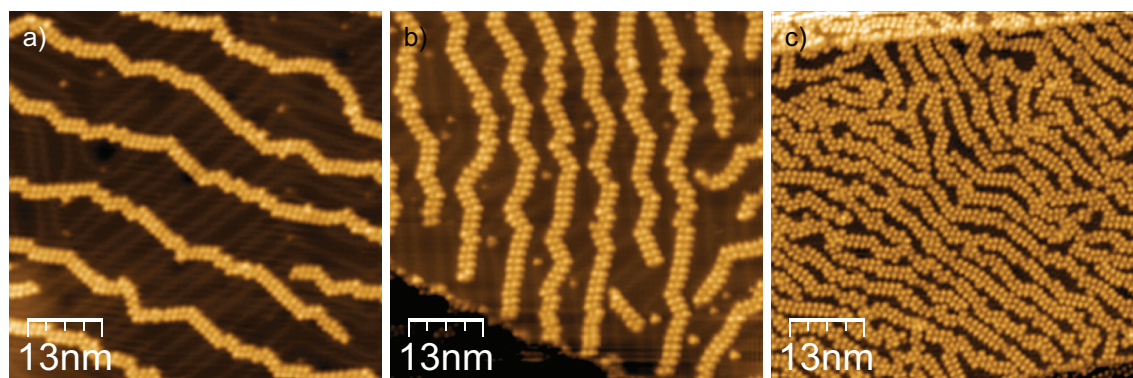


Figure 4.6: STM images of merocyanine chains on Au(111) at low (a), intermediate (b) and dense (c) coverage. The chains avoid lateral packing, regardless of their orientation with respect to the underlying herringbone reconstruction.

herringbone reconstruction underneath the layers suggests that the molecules populate a weakly bonded adsorption state, as usually found in several low temperature phases of organic adsorbates on Au(111) [97].

We cannot relate *a priori* the observed structures to the closed or to the open form, since during thermal sublimation, equilibrium between both species might have been reached. High resolution STM images as in figure 4.4 b) find that all molecules exhibit the same shape and orientation on the surface, demonstrating that we have only one type of molecular species. Chiral intramolecular features, visible in figure 4.4 b), could be equally

explained by the presence of the chiral SP or the prochiral MC isomers on the surface. The observed row structure and the dimension of its unit cell ( $1.2 \times 1.1 \text{ nm}^2$ ) agree with previous observations of this system [95], which were attributed to the closed SP isomer.

The properties of the molecular layer change drastically when the annealing temperature reaches  $T_{\text{ann}} \sim 300 \text{ K}$ . In this case, the two-dimensional molecular domains disappear, and a new phase composed of molecular chains is observed (figure 4.5a). The chains show a preference to follow the underlying Au(111) herringbone reconstruction, as well as to avoid lateral packing, even for the case of higher coverages (see figure 4.6). The former can be understood as a consequence of an enhanced interaction with the metal surface. The latter is characteristic of long-range repulsive interactions among chains, similar to those found in ensembles of organic molecules with large dipole moments or charge transfer on metal surfaces [98, 99, 100]. Hence, a stronger interaction of the high-temperature phase with the metal surface can be concluded by the STM observations. It is important to remark that since the experiments are performed after posterior cooling to low temperatures, the transformation from 2D domains to chains is not reversible, further confirming that the chain structure corresponds to the thermodynamically more stable phase.

A close-up view of such a molecular chain is shown in figure 4.5 b). The chain structures can be in general explained as formed by the packing of molecular dimers. Each molecule is imaged as an asymmetric oval feature with a higher lobe ( $0.25 \text{ nm}$  high) on one side. The molecular dimers could be detached from the chains by lateral manipulation using the tip of the STM (figure 4.5 c–d). In contrast, the dimers themselves are stable units, which could not be dissociated by the STM tip nor by the tunneling current without irreversibly destroying the molecular features. Qualitatively, this fact can be interpreted as the dimer bonding strength being larger than the interaction between molecule and metal and between adjacent dimers.

Based on the well-known isomerizability of spiropyran, we may associate the two observed phases with structures formed each by solely one of the two different isomers of the parent spiropyran compound, with a complete transition from one to the other triggered by temperature and by the presence of the metal substrate. However, the STM images do not provide a definitive assessment of the molecular isomers, nor their orientation, that appear at each phase. In order to identify them, x-ray photoelectron and x-ray absorption spectroscopies, as well as high resolution electron energy loss spectroscopy were performed on the system by our collaborators of the AG Kuch and AG Wolf as a function of the annealing temperature.



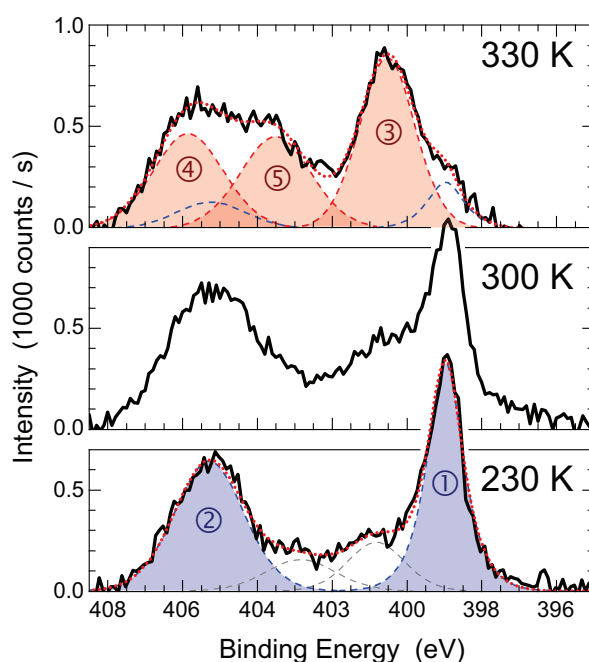


Figure 4.7: X-ray photoelectron spectra of  $\sim 1$  ML spiropyran on Au(111), taken during heating of the sample from 230 K to 330 K. The shown features correspond to the nitrogen 1s level. The splitting of the peak at 405.3 eV (②) into two peaks (405.8 eV ④ and 403.5 eV ⑤), the disappearance of the peak at 399.0 eV (①) and the observed emergence of the peak at 400.5 eV (③) are signals of the isomerization process from the SP species at 230 K to the MC species at 330 K, as described in the text. Fitting curves are marked as dashed lines. The photon energy used was 500 eV. Source of figure: [101].

#### 4.3.1 Temperature Dependent Ring-Opening and Adsorption Structure

The XPS spectra of the nitrogen atoms 1s core level were measured at temperatures ranging from 230 K to 330 K (figure 4.7). Measurements and analysis were performed by W. Kuch and coworkers [101]. The spectra taken at 230 K show two clear peaks at 399.0 and 405.3 eV, that resemble the N1s photoemission features of crystals of benzooxazolinic spiropyran [102]. We therefore assign the species observed at low temperatures to the SP isomer. The emergence of two distinct peaks can be explained by chemical shifts (see section 2.2.2) of the two nitrogen atoms's 1s levels due to their different environment. By comparison with [102], the peak at 399.0 eV can be assigned to the indoline nitrogen atom while the 405.3 eV peak originates from the nitro group's N atom.

This interpretation is further supported by the spectra taken at higher temperatures. In analogy to our STM findings, the spectral shape undergoes a conversion at approx. 300 K. The 330 K spectrum shows a new component at 400.5 eV while the peak at 399.0 eV

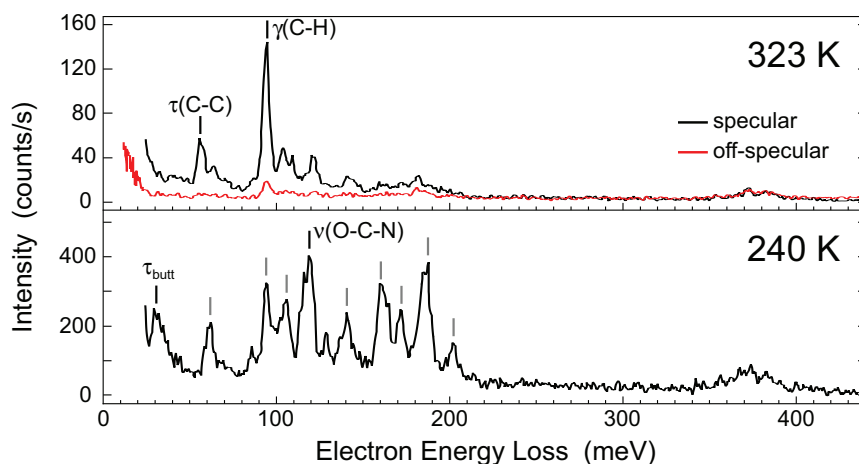


Figure 4.8: HREELS data of 0.7 ML SP molecules on Au(111), measured after annealing to 240 K and to 323 K. The black curves were recorded in specular and the red curve in 9.2° off-specular scattering geometry with a primary electron energy of 3.7 eV. Vibrational modes mentioned in the text are marked and labeled. Other modes are marked and were designated in reference [111]. The specular signal contains both dipole- and impact-scattered components, while only impact-scattered electrons contribute to the off-specular signal, as described in section 2.2.1. By comparison of the two curves, it can thus be determined if a vibrational mode has a dipole-active  $z$ -component. Source of figure: [104].

vanishes. The nitro groups's peak at 405.3 eV is broadened and split into features at 405.8 eV and 403.5 eV. The total spectrum's shape is now typical for a merocyanine molecule [102, 103]. The higher binding energy of the indole nitrogen peak indicates an increased electronegativity of this atom, what can be explained by a partial zwitterionic character of the MC molecule: an additional  $\pi$  bond of the nitrogen leads to a positive charging of this atom (see figure 4.2 b). Our interpretation of the XPS spectra is therefore that the observed low temperature isomers are of the SP type, transforming into the MC form on heating the sample above 300 K.

A comparable picture can be drawn from HREEL spectra taken at 240 K and 323 K (figure 4.8). Measurements and analysis were done by P. Tegeder and coworkers [104]. The low temperature spectrum shows a large number of strong peaks, that can be assigned in good accordance to molecular vibrations of SP [105, 106, 107] or to its subgroups benzopyran [108] or nitrobenzene [109, 110]. Especially important are the clear features of the O-C-N stretch vibrations ( $\nu(\text{O-C-N})$ ) at 119 meV and of the butterfly torsional modes at 32 meV between the pyran and the phenyl rings ( $\tau_{\text{butt}}$ ), that cannot originate from MC molecules, thus giving another hint that the low temperature phase must be attributed to the SP isomer.

In HREEL spectra taken at a sample temperature of 323 K the  $\nu(\text{O-C-N})$  and  $\tau_{\text{butt}}$  peaks have vanished, showing that the C-O fission has taken place during the heating. A flat-lying orientation of the MC molecules on the surface can be assumed from the strong dipole activity of the C-H deformation modes  $\gamma(\text{C-H})$  and the phenyl ring torsion modes  $\tau(\text{C-C})$ .

Another confirmation of this model comes from angle resolved NEXAFS measurements, performed and analyzed by W. Kuch and coworkers [101]. The absorption properties of the transitions from the nitrogen 1s state to the unoccupied molecular orbitals were measured in the same temperature range as the other experiments, i.e. between 230 K and 330 K. The resulting spectra are shown in figure 4.9. All spectra measured with light at a grazing incidence angle show one prominent peak at around 403 eV. This peak can be assigned to an electronic transition from a core level into a nitrogen's  $\pi^*$  level as a final state. Since the only nitrogen atom of a SP molecule involved in a  $\pi$  bond is located at the nitro group, this peak must be attributed to this moiety. The feature is absent in all normal incidence spectra, indicating that the nitro group is aligned parallel to the sample all the time, what is consistent with the HREELS data. For sample temperatures above 300 K, a second, but shifted, intense  $\pi^*$  peak appears at 399 eV in the grazing incidence spectrum. The interpretation is that when switching to the zwitterionic MC isomer, the indoline nitrogen atom starts to participate in an additional  $\pi$  bond (see figure 4.2). The shift of the peak with respect to the first at 403 eV is caused by the increased core level binding energy on the positively charged N atom, what could be already seen in the XPS data. The absence of this peak in the normal incidence spectrum tells us that the indole group, and thus the whole MC molecule, is aligned flat on the gold surface, in complete agreement to the HREELS data.

With the identification of the molecules forming each phase and their orientation at the surface it is now possible to construct complete structural models that furthermore explain the nature of intermolecular forces stabilizing the different molecular phases and that account for the STM images. We use for this purpose molecular dynamics simulations using the *mm2* force field as implemented in the TINKER package [112]. The orientation of the molecules at the surface deduced from our NEXAFS and HREELS measurements has been fixed in the simulations by confining the motion of various atoms to a plane (more details are given in the appendix B.1). We use a two step method based on an initial stabilization of the preferred packing structure of two molecules, followed by a subsequent minimization of larger molecular ensembles constructed by fitting the relaxed dimers to high-resolution STM data. This approach allows us to account for weak non-covalent forces among a large ensemble of molecules, and its validity is tested by checking that the resulting minimum energy configurations agree with the experimental data.

To simulate self-assembled islands of SP isomers, we impose a molecular orientation such that the benzopyran part of the molecule lies parallel to the confining plane, with the dimethyl moiety of the indoline group oriented towards the metal surface. This is

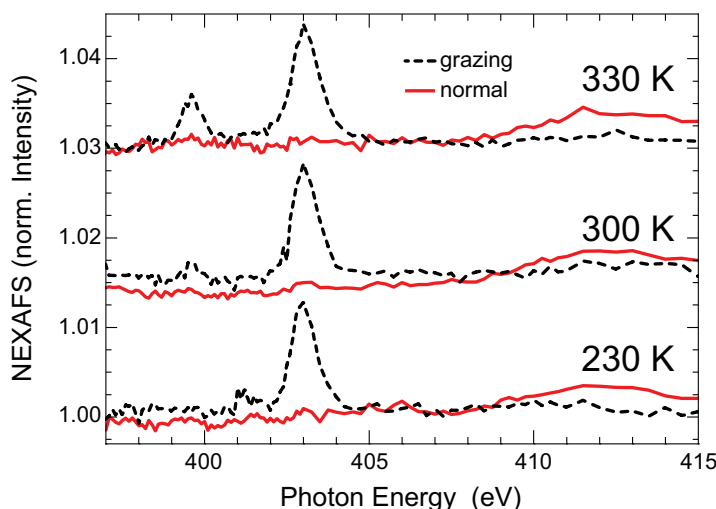


Figure 4.9: Nitrogen K edge X-ray adsorption spectra of 1 ML SP on Au(111), measured during heating of the sample from 230 K to 330 K. The spectra were measured at normal (red curves, 0° to surface normal) and at grazing light incidence (dashed black curves, 70° to surface normal). The spectra are shifted vertically for clarity. Source of figure: [101].

shown in figure 4.10 a), where the resulting dimer configuration with the lowest energy is pictured. In this structure, two spiropyran molecules of different chirality face each other in a mirror-symmetrical alignment. The energy-minimized island structure was composed from this and is shown in figure 4.10 c) in comparison with an STM image. The most stable configuration comprises rows with SP molecules of alternating chirality, in agreement with the chiral intramolecular structure observed in the STM images in figure 4.4 b) [95]. Chiral recognition between the rows also exists, where the most stable configuration is the one that bonds two rows with the same chiral sequence (rows 1 and 2 in figure 4.10 c). Occasionally, domain boundaries are observed (rows 2 and 3 in figure 4.10 c), which can be explained by a change in the chiral sequence of the rows<sup>1</sup>. The nitro group appears to have a dominant role in the stabilization of these structures through the formation of two hydrogen bonds with molecules in the neighboring chain.

The most stable rotamers of a free MC molecule are the four planar conformations with their  $\beta$  angle in a trans state (CTT, TTT, CTC and TTC) [86, 113]. On a metal surface this tendency is retained, since the interaction between the ring systems and the surface can be maximized in a flat-lying adsorption geometry. Nevertheless, the conformational flexibility between the four cases is reflected in the observation of several dimer bonding structures in the merocyanine chains, as they follow the underlying herringbone reconstruction. Among all the possible combinations of MC planar isomers, our calculations

<sup>1</sup>With some functionalized STM tips, such change in the chiral sequence of a row leads to a change in the intramolecular contrast, as was observed in [95].

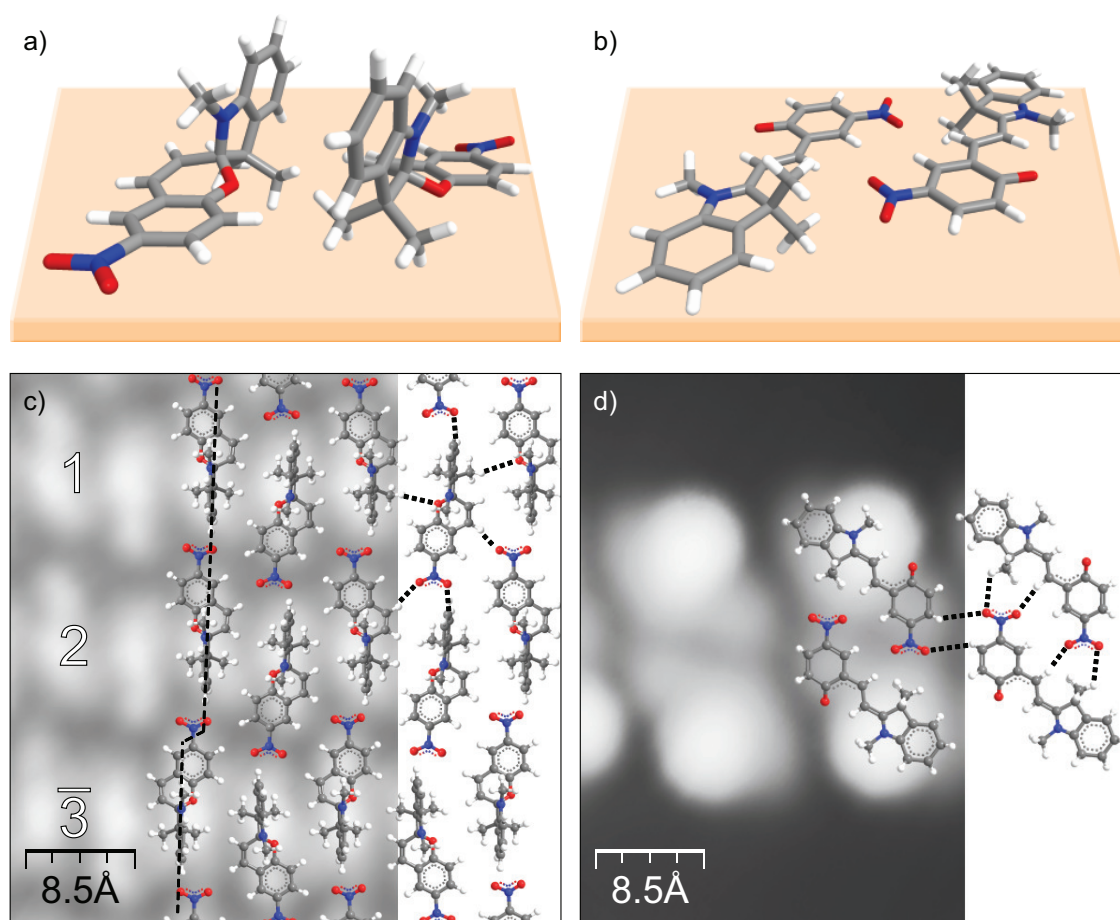


Figure 4.10: Three-dimensional minimum energy configuration of a) nitro-spiropyran and b) nitro-merocyanine molecular dimers. An underlying surface parallel to the  $z = 0$  plane, in which the motion of some atoms is confined, is drawn only for illustrational purposes. c,d): Top view of the corresponding molecular domains, partially superimposed to the STM images. Expected hydrogen bonds joining one molecule to its neighbors are shown as dashed lines. In c) molecular rows labeled 1 and 2 have the same structure, whereas the row  $\bar{3}$  is rotated by  $180^\circ$ , causing a misalignment between rows (vertical dashed line).

of a free two-dimensional layer show a universal tendency for the molecular dimers to be stabilized by the nitro end-groups. As shown in figure 4.10 d), the most stable dimers are created when these groups are involved in the formation of H-bonds between them. According to our model, the higher lobe observed in the intramolecular structure marks the site of the indole nitrogen atom. Hence, its higher appearance agrees with the partial positive charge localized at this site in the MC zwitterion: the positive charge reduces the local work function of the metal surface and thus the effective barrier for tunneling electrons. This local charge could also play an important role in the apparent electrostatic repulsion between chains observed in the STM images [100].

### 4.3.2 Stabilization Inversion on the Metal Surface

One conclusion from these experiments is the stability inversion of the adsorbed  $SP \rightleftharpoons MC$  system with respect to the free one. In gas phase or in solution, the spiropyran isomer is lower in energy and thus more stable than merocyanine. After a  $SP \rightarrow MC$  conversion, the molecules will be subject to a gradual thermal backswitching into the spiropyran form. On the Au(111) surface, we observe the opposite behavior, as MC is now the more stable isomer. This stability inversion due to the surface takes place for two reasons: either a weakened C-O bond gives rise to a reduced  $SP \rightarrow MC$  activation energy or a comparatively strong merocyanine-metal interaction may increase the activation barrier of the  $MC \rightarrow SP$  backswitching. The former can be tested by a closer analysis of the HREELS data.

To evaluate the switching barrier height of the reaction, the temperature dependence of the switching rate was analyzed. The C-H deformation mode  $\gamma(C-H)$  of the HREELS data was used as a quantitative measure for the number of molecules switched. Upon annealing of pure spiropyran preparations to different switching temperatures, the relative peak intensities can be correlated to an Arrhenius-like expression (for more detail see reference [111]). From this, the activation barrier of the  $SP \rightarrow MC$  reaction can be extracted to be  $0.84 \pm 0.05$  eV. This value is close to the free molecule's activation energy, what can be attributed to the weakly adsorbed state of the spiropyran on Au(111).

Consequently, the origin of the stability inversion of the species can only be explained by a considerable increase of the binding energy of the merocyanine molecules. This is understandable: due to its planar shape, the molecule can maximize its interaction with the surface in a flat-lying adsorption geometry. This is known to be the energetically preferred orientation of aromatic molecules on most metal surfaces [114, 115]. The binding strength is further enhanced by the zwitterionic character of the merocyanine molecule that induces interactions with image dipoles in the metal.

Under this conditions, the  $SP \rightarrow MC$  reaction is much more likely to occur than its back reaction. The opening of the ring simply requires the cleavage of a C-O bond, and it can occur even in molecules embedded in an ordered domain. In contrast, the closing reaction of a flatly adsorbed merocyanine molecule would imply the previous removal of the indole group from the surface and the cleavage of the intermolecular hydrogen bonds stabilizing a molecular dimer. The addition of these non-covalent forces to the C-O bond formation signifies a substantial increase in activation barrier to close the adsorbed MC isomer.



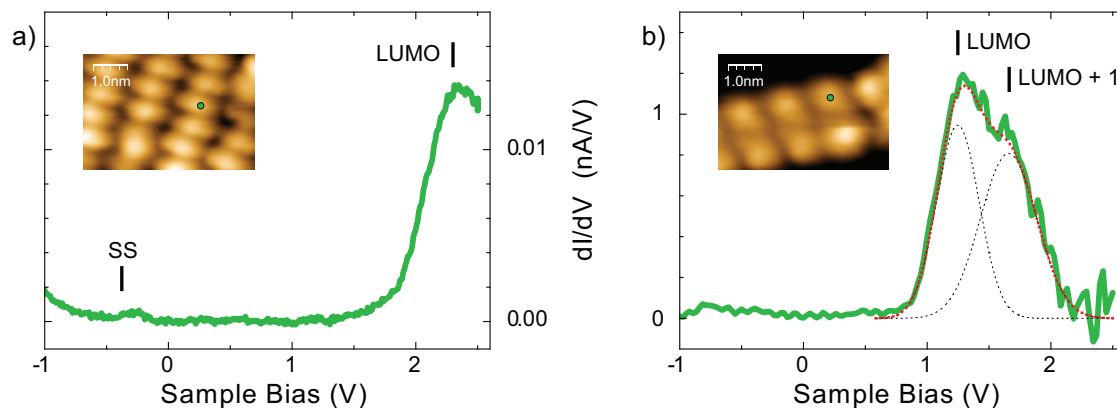


Figure 4.11:  $dI_t/dV_S$  spectra of spiropyran (a) and merocyanine (b) molecules on Au(111). In a) the center of the LUMO at  $2.4 \pm 0.1$  eV and the surface state (SS) is marked. In b) a fit of two Gaussian curves reveals the LUMO (center at  $1.25 \pm 0.1$  eV) and the LUMO+1 ( $1.6 \pm 0.1$  eV). The insets show the corresponding STM images, the green points mark the positions of the spectra.

### 4.3.3 Tip-induced Ring Opening

The next question we want to address is, whether an isomerization process can also be induced by means of the STM tip. We start by measuring  $dI_t/dV_S$  spectra to analyze the electronic structure of the species in more detail. The results are shown in figure 4.11. Chart a) shows a typical tunnel spectrum of a spiropyran molecule inside an island. In the unoccupied range of the spectrum, a LUMO resonance is clearly visible as a peak at  $\sim 2.4$  V. No other unoccupied state can be seen at energies closer to  $E_F$ . In the region of occupied states no clear feature can be observed besides the Au(111) surface state. It was not possible to perform spectroscopy with voltages above 2.5 V for reasons described below.

The spectrum of a merocyanine molecule is shown in figure 4.11 b). The spectrum shows clear differences from the SP case: two unoccupied resonances, the LUMO and the LUMO+1, are visible at energies 1.25 eV and 1.6 eV. The two states overlap due to their broad line width but a distinction is possible by fitting two Gaussian curves as shown in the figure. The height of the peaks with respect to each other varies on the different molecules. A possible origin of this observation may be the fact that merocyanine molecules can occur as four different rotamers in a flat-lying geometry that may slightly differ in their electronic details. Like in the case of the spiropyran molecules no clear features are found in the negative part of the spectrum.

Spiropyran molecules show a tendency to undergo a reaction as soon as a voltage in the range of the LUMO resonance ( $\sim 2.4$  V) is applied (figure 4.12 a–d). This effect often appeared while the voltage was ramped upwards for measuring the spectrum and usually

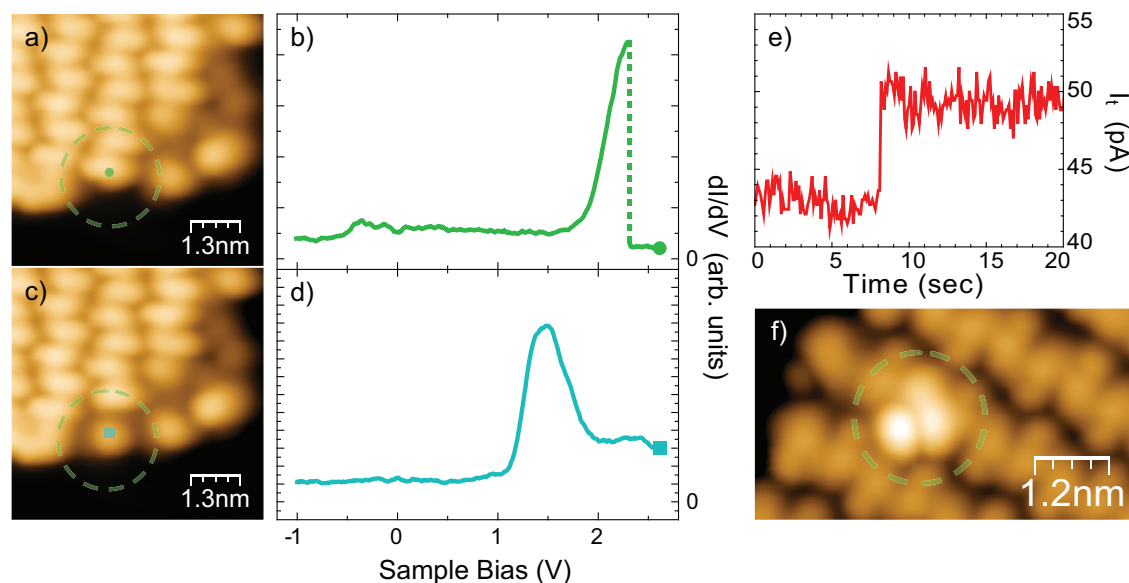


Figure 4.12: SP  $\rightarrow$  MC switching processes induced by tunneling electrons. a): Image of a spiropyran island before the switching experiment. The probed molecule is marked. b):  $dI/dV_S$  curve recorded on the molecule while ramping the voltage upwards. A sudden drop of the signal occurred at 2.3 V when  $V_S$  approximately reached the LUMO position. The backward curve can be seen in d) and shows the typical fingerprint of a MC molecule. The subsequent image is shown in image c). e):  $I_t(t)$  curve recorded on top of a spiropyran molecule in an island at a bias voltage of 2.0 V without feedback loop. The jump of the  $I_t$  at 8 s signals a switching. f): Image of the molecule probed in e) after the switching event.

manifests in a sharp change of the tunnel current. Since the voltage is ramped twice for taking one spectrum (increasing  $V_S$  at first to a maximum and then descending it again), it is possible to probe the LDOS on the same spot directly after the reaction has occurred. In most cases, this second spectrum shows that the characteristic LUMO peak at 2.4 eV has vanished. Instead a strong resonance with a center at approximately 1.5 V appears, similar to the merocyanine's LUMO/LUMO+1 compound peak. The reaction can be induced on molecules at the island's borders as well as on molecules inside the island. By taking a subsequent image of the area, the impact on the topography of the system can be examined. Molecules on the island's border change their appearance after such an event and now resemble merocyanine molecules that frequently decorate the islands borders (see figure 4.12 b).

Based on these results, we interpret the observed reaction as a SP  $\rightarrow$  MC isomerization process. The voltage dependence of the switching as can be inferred from the voltage ramps on single molecules can also be revealed by scanning at different voltages: on scanning with a sample bias of e.g. 1.3 V the molecules are not affected, whereas many



switching events were observed at voltages larger than 1.7 V, in coincidence with the spiropyran LUMO. From this we can determine the underlying mechanism as a process mediated by an anionic molecular state. A phonon mediated effect that may also experience an increase in switching rate close to a resonance, as seen in the former chapter, is quite unlikely with a view to the low currents applied here. The observation that the ring opening can be induced by the transition into an anionic state is another type of isomerization process that has to be distinguished from the well-known photo-isomerization, where an intramolecular HOMO  $\rightarrow$  LUMO excitation process is induced by photons in neutral molecules.

The SP  $\rightarrow$  MC isomerization cannot be induced only on spiropyran molecules at island borders but also on molecules inside an island. The main difference is thereby the resulting STM image, as it is shown in figure 4.12 f): the merocyanine molecule appears as additional protrusion that surmounts the surrounding molecules about 0.5 Å. The explanation of this is that steric hindering by neighboring spiropyran molecules prevents the newly-created merocyanine from taking its common planar position.

To obtain quantitative information about this electron-induced switching process, we performed a number of experiments of controlled voltage pulses that were applied to either type of molecules. At the beginning of the operation, the STM tip is positioned over the selected isomer. The required sample bias above the onset of 1.7 V is then set, after the feedback loop is opened for a few seconds. The tunneling current is recorded during the whole procedure. Usually, a switching reaction can be identified by a sudden change in the current due to a change in the LDOS and/or the junction geometry. The type and quality of the reaction is checked by subsequent imaging and by measuring  $dI_t/dV_S$  curves.

We applied this procedure at different voltage and feedback current values to merocyanine molecules in the dimer chain structure. It turns out that no reproducible reaction could be achieved on this species. All observed events can be classified as being either planar rotations or translations or leading to uncontrollable and irreversible changes in the shape and electronic structure of the molecule. We conclude that this behavior is a confirmation of our picture of the tight planar adsorption of the molecules that prevents the structural back-folding, what is a prerequisite for the C-O bond formation.

In a next step the method was applied to spiropyran molecules in islands and at island borders. Since switching is only expected in the voltage range between 1.7 V and 2.4 eV, we restrict our experiments to this interval. The molecules showed an isomerization behavior, as expected from the previous experiments, i.e with jumps in the spectra occurring after a certain time span. From this, a value of the quantum yield for isomerization by tunneling electrons can be estimated to be  $\approx 2.2 \cdot 10^{-10}$  switching events per electron<sup>2</sup>. Although this value lies within the range of tunnel electron quantum yields for isomeriza-

<sup>2</sup>To estimate the electron switching quantum yield  $\Phi$ , the number  $n_i$  of electrons that were transported through the junction before the isomerization took place was registered for each observed event  $i$ . The function  $\Phi \cdot \exp(-n \cdot \Phi)$  was then fitted to the histogram of the set of  $n_i$ .

tion of adsorbed molecular switches reported in the literature [78, 69, 79], the observed yield is about nine orders of magnitude smaller than typical photo-isomerization yields of spiropyran molecules in solution: the quantum yield for conventional photocoloration of undisturbed spiropyrans is in the order of one [90]. Two reasons can account for this large difference: either the efficiency of the isomerization via the anionic state that has been probed by the tunneling electrons is much smaller than the one for photoswitching of neutral molecules. Or the quenching influence of the metal surface accounts for the large reduction of the process rate. To distinguish between these two possible explanations, we performed light illumination experiments to measure the quantum yield for photo-isomerization on the metal surface.

#### 4.3.4 Effect of Illumination

Under the assumption that the big difference of nine orders of magnitude between the tunneling electron yield for  $SP \rightarrow MC$  isomerization on the gold surface and the photo-switching yield of free molecules is only caused by the different efficiencies of the two switching mechanisms (i.e. switching over the anionic state by tunneling electrons and over the neutral electronically excited state by photons), we would expect a quantum yield for photo-isomerization on the metal surface in the same order as in solution. On the other hand, if the quenching properties of the metal surface are responsible for the differences, a strong reduction of the photon quantum yield should be detected. Therefore, the light illumination experiments can help to decide about the origins of the observed low switching rates.

In a free spiropyran molecule, photoabsorption of light with wavelengths of 245 nm (5.06 eV) and 345 nm (3.59 eV) triggers the ring-opening process. The backward reaction can be excited by photons of about 580 nm (2.1 eV) wavelength. On the surface these values may be changed, either by altered electronic level positions [70] or by switching via different absorption processes. For being sensitive to all possible types of processes, we decided to use two wavelengths for the experiments: a short one (355 nm, 3.49 eV) that may induce intramolecular excitations in SP molecules and a longer one (532 nm, 2.33 eV) that would still allow for excitations from the Fermi level into the LUMO state. Such additional mechanisms can lead to photo-isomerization on the metal surface as well, as was shown by [92]. Photo excited hot metal electrons or holes may populate the LUMO or HOMO by first or higher order processes. These processes are closely related to the above described tunnel electron attachment. As light source either a Xe arc lamp or a neodymium-doped yttrium aluminum garnet (Nd:YAG) laser that was provided and run by M. Wolf and coworkers [104] were used.

Samples of freshly prepared SP islands were illuminated for times between 30 and 60 minutes. The sample temperatures ranged between 140 and 230 K and the illumination light power was set to values between 10 and 140 mW/cm<sup>2</sup>. Before and after the illumi-

nations, the relative number of merocyanine molecules with respect to the total number of MC and SP molecules was determined from the STM images<sup>3</sup>. In combination with the photon flux this value allows the evaluation of the resulting photon quantum yield for  $SP \rightarrow MC$  isomerization<sup>4</sup>. The resolution of this method is limited by the statistical fluctuation of the relative number of MC molecules in the different images and can theoretically be increased by analyzing a larger sample area, i.e. more STM images. In our case, a minimum resolution of about  $10^{-9}$  switches / photon was achieved. Within this error range, we were not able to detect a significant increase of the number of merocyanine molecules after the illuminations. This means that the photon yield for isomerization on the gold surface is equal or less than  $10^{-9}$  switches / photon and therefore at least eight orders of magnitude smaller than the yield of free spiropyran molecules.

The main result of this experiment is the finding that the switching processes are strongly hindered by the Au(111) surface. From the low photon switching yield on the surface, we can conclude that quenching processes on the metal surface play an important role. The lifetime of the electronically excited states is reduced by additional relaxation channels into the substrate. The lifetime of an electron in the spiropyran's LUMO can be estimated from the peak line width in STS data to amount to  $2 \cdot 10^{-15}$  seconds. This time appears to be not sufficient to initiate the ring-opening process. Besides this, the  $MC \rightarrow SP$  back-switching process was found to be hindered by the surface as well, since the merocyanine species binds strongly to the substrate, what inhibits molecular folding processes that are required for the back reaction.

## 4.4 Ring-Opening Reactions of Spiropyran on Bi(110)

The results of the last section suggest that a different substrate can improve the switching rates of the adsorbed spiropyran molecules. An appropriate candidate should exhibit a low DOS at the LUMO energy and should have a reduced binding strength to the planar merocyanine molecules. This is expected to be the case for a non-d-band metal. From these considerations, we decided to perform further experiments on molecules adsorbed on a Bi(110) surface that complies with these requirements.

<sup>3</sup>Even before the illumination a small number of MC molecules could be found in the SP islands and on their borders.

<sup>4</sup>With the relative MC numbers  $N_{MC} = \#MC / (\#SP + \#MC)$ , the area density  $d_{Ph}$  of the applied photons and the area of one SP molecule  $a_{SP}$ , the yield can be calculated as  $\Phi = (N_{MC,after\ Illu.} - N_{MC,before\ Illu.}) / (d_{Ph} \cdot a_{SP})$ .

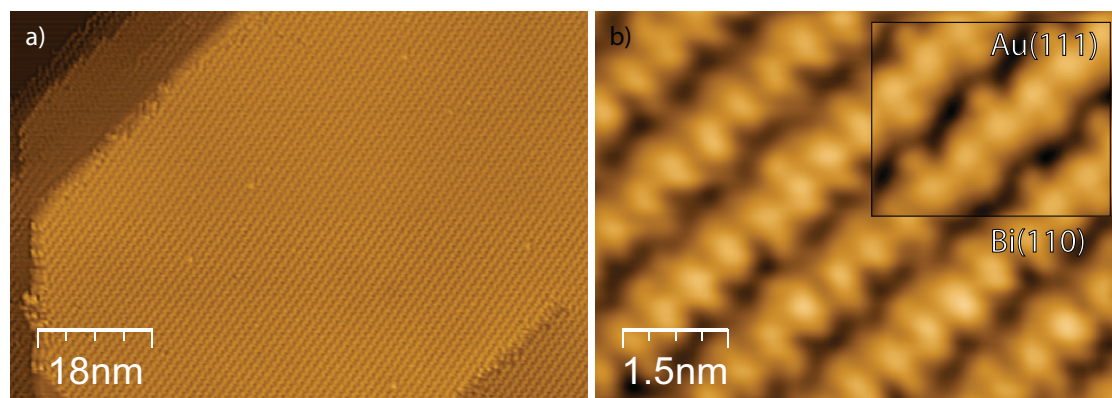


Figure 4.13: Spiropyran island phase on Bi(110). a) shows an overview and b) a close-up of the molecules. The molecular appearance is identical to the case of Au(111) (small inset). Image feedback parameters: a)  $I_t = 50$  pA,  $V_S = 1.2$  V, b)  $I_t = 50$  pA,  $V_S = 0.7$  V, inset  $I_t = 47$  pA,  $V_S = 1.0$  V.

#### 4.4.1 Adsorption on Bi(110)

On Bi(110), the adsorption behavior of spiropyran resembles the one previously found on Au(111) to a large extent. One exception from this is the temperature range that is necessary to form the ordered island phase. On gold, the maximum temperature value for obtaining self assembled spiropyran layers is at about 280 K. At higher temperatures the molecules will irreversibly switch to their MC phase. In contrast to that, a preparation at room temperature on bismuth gives rise to pure spiropyran islands on the surface (figure 4.13). The topographic structure of these islands resembles in shape, size and character the one found on the gold sample (figure 4.13 b) and inset). Their apparent height is about 2.7 Å and thus roughly equal to the case on Au(111). From the large amount of agreement between the topographic images of the islands on the two surfaces we conclude that the underlying molecular structure is very similar or equal. As already stated, the weakly interacting gold surface and the even weaker bismuth surface act solely as a 2-dimensional template and do not disturb the intermolecular forces inside the molecular layer.

#### 4.4.2 Thermally Induced Ring-Opening

When the sample is annealed to 330 K, the structure of the molecular overlayer changes drastically. Instead of one ordered layer, three distinct types of phases can now be observed that are depicted in figure 4.14 a). The most apparent difference between the three structures is their ordering behavior: while the first phase is completely ordered, the second structure shows a clear long-range order but it also reveals a certain variety in its short range composition. The third structure seems to be completely unordered on the first view,



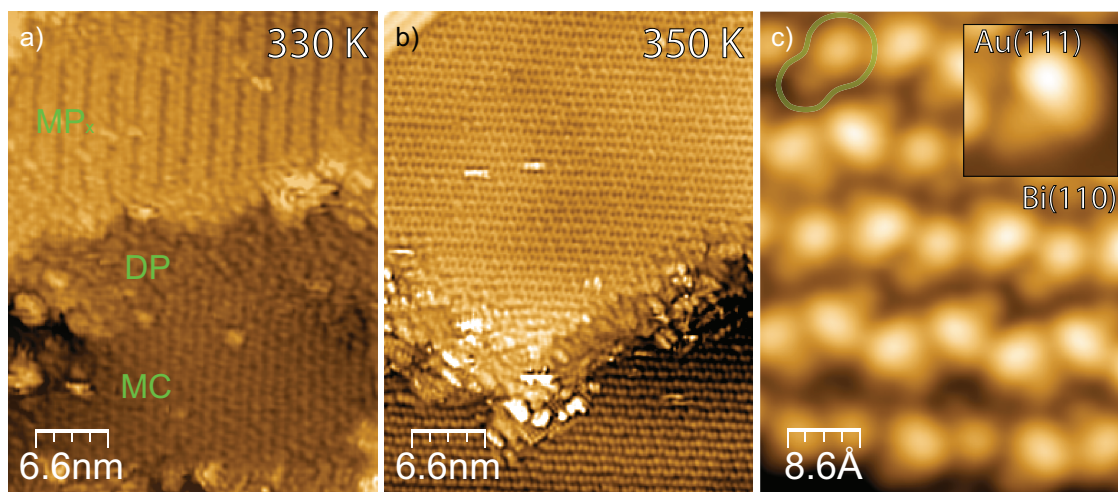


Figure 4.14: a): Molecular phases on Bi(110) after annealing to 330 K: the pure merocyanine phase (MC), a disordered molecular phase (DP) and a phase with long-range order ( $MP_x$ ) are present at the same time. b): After annealing to 350 K only the MC island phase is observed. c): Close-up view of the pure MC phase. A single molecule is marked by the green line. The shape of the molecules resembles the ones previously found on Au(111) (inset image). Image feedback parameters: a)  $I_t = 10$  pA,  $V_S = 1.0$  V, b)  $I_t = 50$  pA,  $V_S = 1.0$  V, c)  $I_t = 60$  pA,  $V_S = 1.0$  V.

although it clearly consists of molecules in one layer with size and height comparable to the spiropyrans.

If the sample is further annealed to 350 K, the surface is completely covered with only the first phase (figure 4.14 b). In high resolution topography images (figure 4.14 c) the structure can be identified as having a  $14 \times 11 \text{ \AA}^2$  unit cell, with a zig-zag pattern of single molecules consisting of two round protrusions. One protrusion has an apparent height of about  $2.5 \text{ \AA}$  while the other is approximately  $0.5 \text{ \AA}$  lower. This appearance resembles single MC molecules on Au(111) (inset figure 4.14 c). In combination with the fact that the molecules appeared after annealing the spiropyran layer we can deduce that these molecules are the result of a thermal  $SP \rightarrow MC$  conversion process.

The assembly structure of the merocyanine molecules differs from the observations on Au(111), where one-dimensional chains were found that are subject to repulsive forces. These forces seem to be reduced on the bismuth surface. A possible explanation may be a change in the molecules' zwitterionic character. On the gold surface the molecule's electronic dipole is stabilized by strong image charges in the metal states. Since these states are strongly reduced in bismuth, the indole nitrogen is expected to accumulate less positive charge, what will reduce the electrostatic repulsion between different molecules. This fact also reflects in the STM images: on the gold surface, the strong protrusion at the position of the indole group, presumably resulting from a reduction of the local work

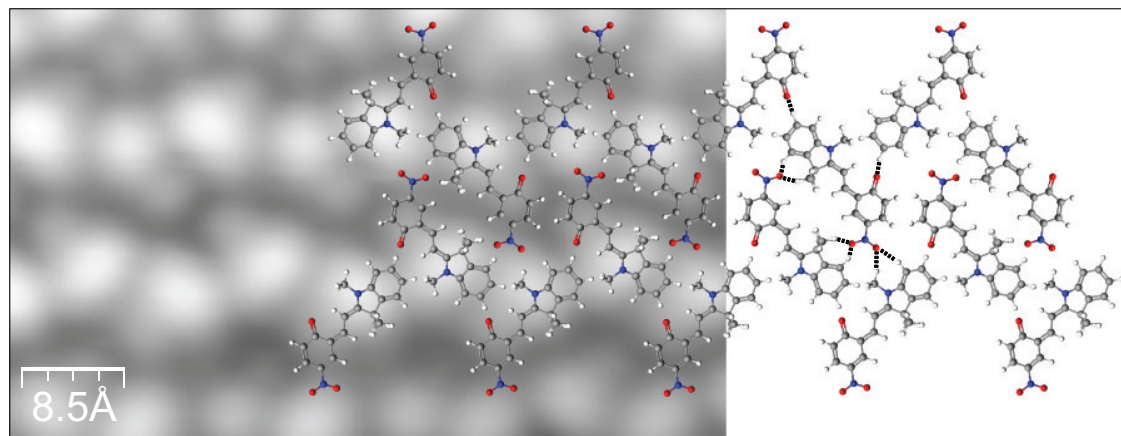


Figure 4.15: Structural model of flat-lying merocyanine molecules on Bi(110). The hydrogen bonds of one molecule are denoted by dashed lines.

function due to its positive charging, appeared much more widespread than on bismuth (compare figure 4.14 c) and inset). A structural model of the phase that was crafted by comparison to the gold case is shown in figure 4.15.

As a first conclusion, we note that a thermal isomerization also takes place on a spiropyran monolayer on bismuth, as it was already shown on gold and for molecules in solution. The critical temperature is similar to that found in many solvents [88]. Furthermore, we see that the molecules remain in their merocyanine form on cooling down to 4 K. We can assume that the binding state to the neighbors and to the substrate stabilizes the molecules and prevents a thermal backswitching to the SP isomer.

#### 4.4.3 Tunnel Electron Induced Ring-Opening

On bismuth, the two isomer phases show slightly different electronic properties from the gold case. The  $dI_t/dV_S$  curves of both species are shown in figure 4.16. The spiropyran spectra show three reproducible features, one occupied state at  $-1.8$  eV (HOMO) and two distinct peaks in the unoccupied states region, one at  $1.7$  eV (LUMO) and another at  $2.6$  eV (LUMO+1). If we compare the LUMO resonance to the value observed on gold, we find a difference of  $0.7$  eV what is in rough accordance to the difference of the two metals work functions<sup>5</sup> ( $\Delta\phi = 1.1$  eV). This means we have an electronic state alignment governed by *vacuum level alignment*, what is typical for weakly interacting molecular systems where no charge exchange with the surface is involved [116].

<sup>5</sup>The small deviation of the energy differences may be due to the non-precise work function value of polycrystalline Bi ( $4.2$  eV) that was used for the work function for Bi(110).

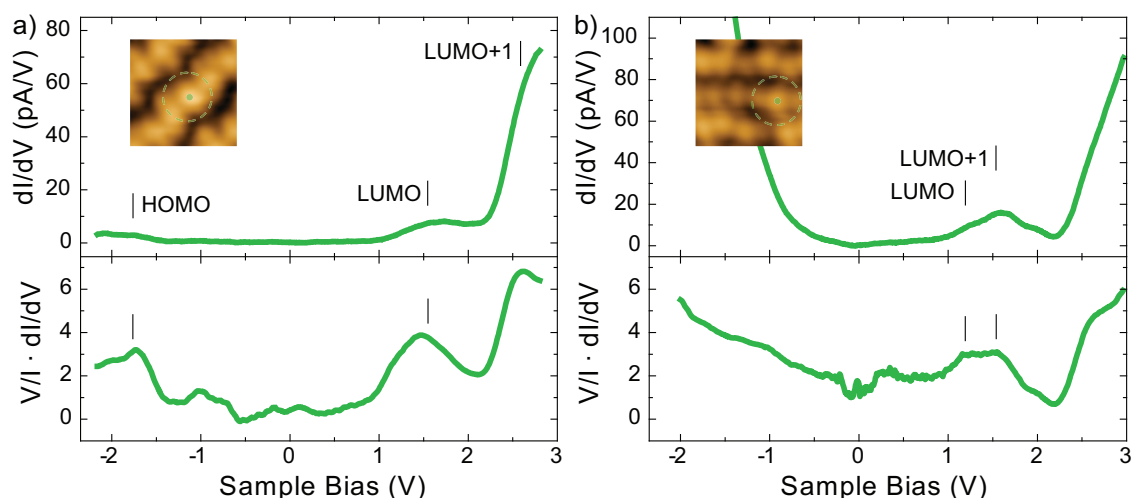


Figure 4.16: Tunnel spectroscopy curves of SP (a) and MC (b) isomers on a Bi(110) surface. The direct  $dI_t/dV_S$  curves are shown on top and the normalized curves are plotted below. The insets show STM images of the probed molecules. The molecular resonances are marked.

The next point of interest in the SP spectrum is the HOMO-LUMO gap. This has a value of 3.5 eV what corresponds to an excitation photon wavelength of 335 nm. This wavelength value is remarkably close to the 345 nm absorption wavelength of the free or solved molecule that is known to induce the ring-opening reaction. The molecule's energy level alignment appears to be mostly unaffected by the substrate. This is a promising observation since it hints for weak interactions between molecule and substrate, what is a precondition for enabling photo-isomerization processes.

The  $dI_t/dV_S$  spectrum measured on a MC molecule in an island is shown in figure 4.16 b). The most surprising property is the similarity with the SP spectrum: a broad feature at about 1.6 V and the onset of a second feature at about 2.6 V resemble the LUMO and the LUMO+1 peak of spiropyran. Like in the gold case, the normalized spectrum reveals that the first feature is composed of two peaks at 1.2 V and 1.6 V. We assign these two peaks to the merocyanine's LUMO and LUMO+1 resonance. A contrasting point to the SP spectrum is that no HOMO resonance can be observed on the Bi(110) surface. The position of the LUMO does not show a significant change compared to spectra taken on the Au(111) surface. Since due to the different work functions of the two metals a considerable change of the  $dI_t/dV_S$  curve should be expected, as indeed was the case for the SP isomer, we conclude that the electronic character of the merocyanine molecule differs greatly on the two substrates. The reason may be again the reduced zwitterionic character of the molecule on bismuth.

Tunnel electron induced SP  $\rightarrow$  MC switching is also possible. Figure 4.17 shows one example of a successful switching of a spiropyran molecule to its merocyanine isomer



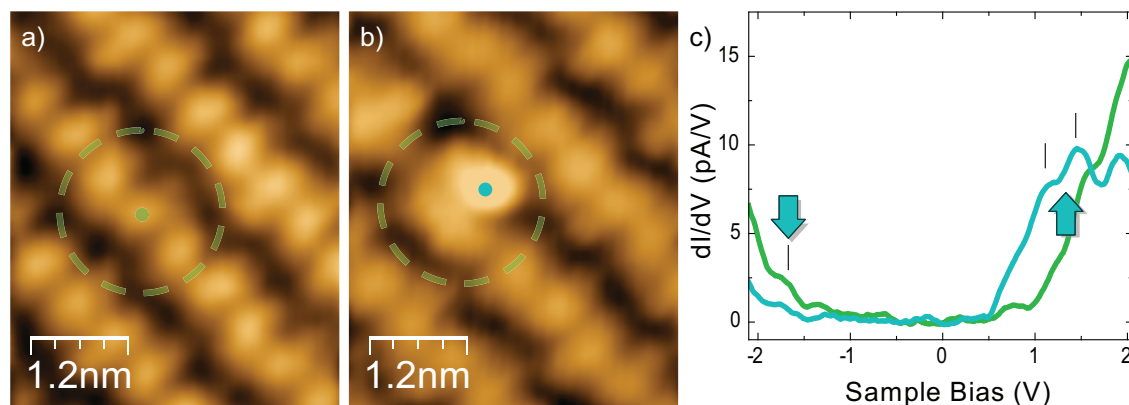


Figure 4.17: Exemplary switching event induced by tunnel electrons. The images show the spiropyran island before (a) and after (b) the switching event was triggered on the marked molecule. c) shows the initial (green) and final (turquoise)  $dI/dV_S$  spectra on the molecule. The effect of the switching is marked by two big arrows: in the occupied regime density of states is lost where the HOMO of the spiropyrans is situated and a double-feature arises in the unoccupied region where the merocyanine's LUMO and LUMO+1 can be expected.

inside an SP island. The resulting image (figure 4.17 b) is similar to the images of comparable cases observed on Au(111).  $dI_t/dV_S$  curves taken before and after the operation are shown in figure 4.17 c). Two apparent changes can be observed in the spectra: one is the increasing double feature at 1.1 V and 1.4 V. Another one is the decrease of density of states in the region of the spiropyran HOMO. Both are signs of a successful isomerization reaction. The experiments show that tunnel electron induced switching on Bi(110) has a similar behavior as on a gold surface. A rough estimation of the switching quantum yield shows that it ranges in the same order as on gold ( $\sim 10^{-10}$  switching events per electron). This is somehow unexpected since the reduced electron density of the metal at  $E_F$  should decrease the lifetime of the anionic state and therefore increase the switching efficiency. We will more deeply discuss this fact together with the results of the photo switching experiments in the last section of this chapter.

#### 4.4.4 Photo-Induced Isomerization

We investigated the photo switching behavior of the spiropyran monolayer (and submonolayer) on Bi(110) by illuminating the sample with light of different intensities and at different substrate temperatures. As light sources, a 45 mW blue light semiconductor diode laser and a 75 W Xe arc lamp, with a continuous spectrum in combination with diverse band pass filters, were used. In all experiments the irradiation angle was  $45^\circ$  to the surface normal. The spiropyran coverage was newly prepared for each illumination attempt

and checked by STM imaging for adequate quality. We can rule out any effects by surface warming or other external sources than the applied light, that may have taken place during the illumination procedure<sup>6</sup>.

In the central experiment, the sample was illuminated for 240 minutes with the laser diode ( $\lambda = 445$  nm (2.8 eV)). The light spot on the sample shows an inhomogeneous intensity distribution in a way that it can be approximated by an oval spot with a Gaussian profile. The maximum intensity at the central point is thereby estimated to be  $260 \text{ mW/cm}^2$  (see appendix A.2). Aside from this maximum, the intensity gradually decreases to zero on the sample, what allows for exploring the effects of several power densities in one sample preparation. The sample was held at room temperature during the whole illumination period. After the illumination, the sample was cooled down to 5 K again for investigation with the STM.

The subsequent examination of the sample surface shows that the molecular layers have undergone a structural change. Depending on the exact position on the sample, the changes vary with the intensity of the applied illumination that is distributed over the sample with the mentioned spot profile. Depending on the degree of illumination, a mixture of different self assembled molecular patterns can be observed with one dominant phase at each position. An overview over this dominant phases is given in figure 4.18 a–d).

On a position with a low irradiation of approximately  $720 \text{ J/cm}^2$ , the initial pure SP phase (4.18 a) has transformed into a grid pattern phase of about  $23.5 \times 13.0 \text{ \AA}^2$  unit cell size (figures 4.18 b, 4.19 a). The shape of the pattern consists of molecules forming higher spinal rows separated by molecules in a ladder step arrangement that are about  $0.3 \text{ \AA}$  lower. Although the difference in appearance of these two sections already hints that the phase consists of different molecular species, this assumption gets confirmed if we take a look at a line of spectra taken at the interface between the spiropyran island and the new grid pattern phase (figure 4.19 b). As we can clearly see, no severe difference can be found between the spectra of the spiropyran molecules and the molecules in the new pattern's spinal rows. On the other hand, clear differences can be seen for the ladder step molecules, that show a shift of the LUMO resonance and an increase of occupied DOS at low voltages. We take this difference, in addition to the fact that the phase appeared upon light irradiation, as an evidence that the phase is built up of spiropyran molecules forming the spinal rows *and* merocyanine molecules as ladder steps. From the size of the pattern's unit cell we can conclude a molecular ratio of merocyanine to spiropyran molecules of either 1:2 or 1:1. Although this point cannot be clarified for completeness, we assume a 1:2 ratio from the existence of two lobes per unit cell in the spinal row (see figure 4.19

---

<sup>6</sup>The temperature of the sample was monitored during the illumination and did not exceed 292 K at any time. A reference preparation (equal process as for illumination but without light) did not evoke any change of the SP islands and rules out other sources of the observed changes than the illumination.

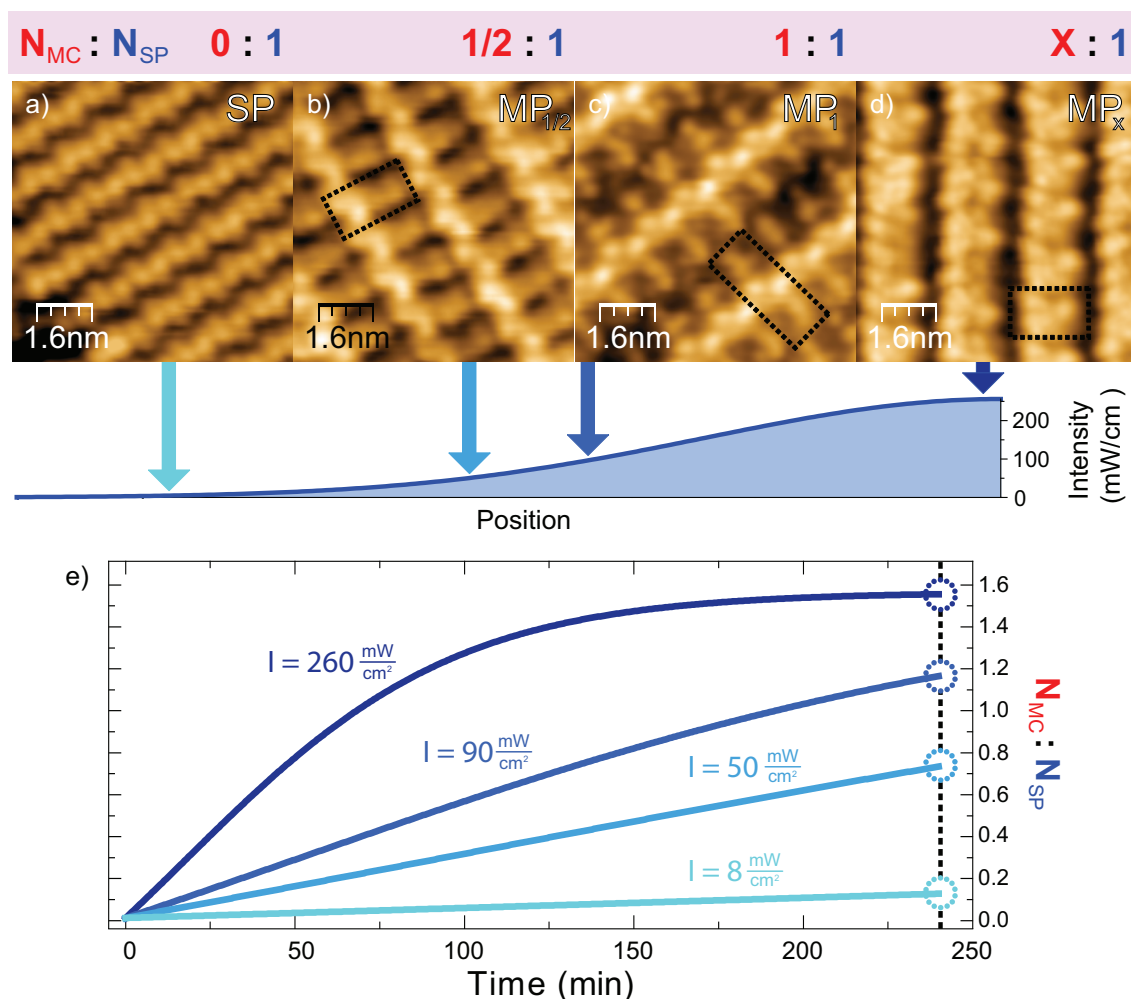


Figure 4.18: Photo switching activity of spiropyran on Bi(110). a) to d) show STM images of the four dominating molecular patterns found at the positions with the different radiation intensities after an irradiation time of 240 min. The Gaussian curve at the bottom depicts this. A unit cell is marked for the three mixed phases and the assumed MC:SP ratio of the pattern is noted above the images. The initial SP island phase (a) is found at no or few irradiation. A presumably 1:2 pattern ( $MP_{1/2}$ , b) and a similarly looking 1:1 pattern ( $MP_1$ , c) were found at places with moderate illumination. After irradiating with maximal intensity a saturation phase with unclear fraction of MC molecules was found in all experiments ( $MP_X$ , d). e): Saturation curves, showing the evolution of the MC:SP ratio for four different illumination intensities that were investigated in the experiments. The curves are drawn from the experimentally observed switching cross sections (see section A.2). The point of observation ( $t = 240$  min) and the thus expected MC:SP ratios are marked by dashed lines.

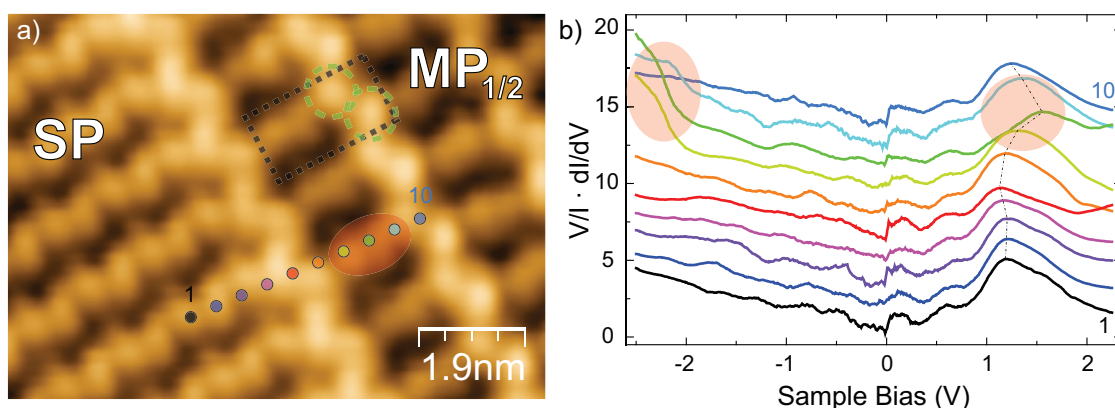


Figure 4.19: Tunneling spectroscopy performed on the interface between a pure SP island and the mixed molecular phase MP<sub>1/2</sub>. a) shows the topographic image of the interface. The points of spectroscopy are marked. Also a unit cell is marked (black dashed box) that contains two lobes in the spinal row (green dashed circles). This suggests the assumption of an SP:MC ratio of 1:2, as described in the text. b) shows the normalized tunneling spectra taken on the ten different positions. As can be seen, the curves taken on the pure spiropyran island (1-4) show a similar shape as the spectra taken on the MP<sub>1</sub> spinal molecules (5,6,10). A clear deviation can be seen in the spectroscopies on the ladder step molecules (7-9): the maximum of the resonance at  $\approx 1.2$  eV (dashed line) shifts up for 0.4 eV and a higher conductivity at voltages below 2.0 V can be observed. The spectra were shifted vertically for clarity.

a) that can be interpreted as two SP molecules<sup>7</sup>. In the following this mixed molecular phase is labeled with the abbreviation MP<sub>1/2</sub>.

A different phase evolves at positions with a higher irradiation fluence of about 1300 J/cm<sup>2</sup> (figure 4.18 c). The phase with a unit cell of  $1.3 \times 3.5$  nm<sup>2</sup> resembles the structure MP<sub>1/2</sub> in several points: a raised spinal molecular row is visible as well as perpendicular ladder step like molecules. The main difference is given by the fact that each unit cell now contains the double number of ladder step molecules: a higher rate of merocyanine molecules is therefore involved in the structure. We therefore label the structure as MP<sub>1</sub>, assuming a MC:SP ratio of 1.

If an illumination of over 3 kJ/cm<sup>2</sup> is applied to the sample, as it was the case in the laser spot center, a transformation of all former patterns takes place to one single phase, that is depicted in 4.18 d). This final phase was found to be the bottom line in all our experiments of long time and high intensity illumination ( $> 2.5$  kJ / cm<sup>2</sup>). It is therefore likely to be a stationary equilibrium phase of the  $SP \rightleftharpoons MC$  reaction on Bi(110). The same phase (MP<sub>x</sub>) was formerly found as intermediate phase during the annealing experiments,

<sup>7</sup>As a test, the analysis described in this section and in appendix A.2 was also applied to a 1:1 ratio and led to very similar results.

where the sample was heated to 330 K, as described in section 4.4.2. This fact elucidates the principle equivalence of the differently driven isomerization processes.

The unit cell of the final phase has a size of  $2.3 \times 1.4 \text{ nm}^2$  and its composition is not unique but has a number of different realization types, as can be seen in high resolution STM images. Hence a determination of the number and amount of components is difficult and the phase gets labeled as  $\text{MP}_x$ . Despite the undefined inner structure of a single unit cell, the alignment of the unit cells with respect to each other follows strict ordering processes, resulting in an extended row pattern.

For completeness it should be stated that during all illumination experiments an additional phase appeared that is characterized by no clear short or long range order. This phase, labeled as *disordered phase* (DP), is believed to consist of both isomers in a non-integer ratio since it already turns up on low illumination fluences ( $\approx 200 \text{ J / cm}^2$ ). At higher intensities it has the effect to compensate for fractional numbers of the MC:SP proportion that cannot form ordered islands.

We thus can state that the experiment evidences photo induced  $\text{SP} \rightleftharpoons \text{MC}$  switching reactions and back reactions on a Bi(110) sample. Upon illumination, the initially pure SP monolayer gradually evolves into an equilibrium between SP and MC isomers. Before the system reaches the actual equilibrium state, it passes several stages of relative SP:MC compositions that lead to distinct self-assembled molecular phases in the STM images.

The speed of the process depends on the illumination intensity. The time dependence<sup>8</sup> of the relative MC:SP ratio for four different illumination intensities is shown in figure 4.18 e). The higher the photon flux, the earlier the equilibrium state is reached. The growth rate of the curves is determined by the reactions' cross sections for photo-isomerization  $\sigma_{\text{sm}}$  and  $\sigma_{\text{ms}}$  (for  $\text{SP} \rightarrow \text{MC}$  resp.  $\text{MC} \rightarrow \text{SP}$  reactions). These quantities can approximately be extracted from an analysis of the STM images at the different positions, as is explained in appendix A.2. For the 445 nm light of the laser diode, we found the photon cross sections to be  $\sigma_{\text{sm}} \approx 4 \cdot 10^{-22} \text{ cm}^2$  and  $\sigma_{\text{ms}} \approx 3 \cdot 10^{-22} \text{ cm}^2$ . These values lie in the range of comparable systems [92]. The corresponding photon quantum yields, that allow a comparison with our other results, are  $\Phi_{\text{sm}} \approx 5 \cdot 10^{-8}$  events per photon and  $\Phi_{\text{ms}} \approx 4 \cdot 10^{-8}$  events per photon.

On this point the question arises, why the observed photo quantum yield on bismuth is three orders of magnitude larger than the electron quantum yield measured on gold and bismuth. A quenching of the switching process due to a reduction of electron lifetimes, as it was stated above for a strong molecule-metal interaction, fails to explain the difference between the yields of tunnel electrons and photons on the same Bi(110) surface, if both reactions are based on the same mechanism. If however the photo induced process is triggered by either an intramolecular HOMO-LUMO excitation or by a cationic

<sup>8</sup>The time dependence follows a typical curve for equilibrium reactions, as it can for example be deduced from equation A.1 by substituting  $F = I \cdot t$ .



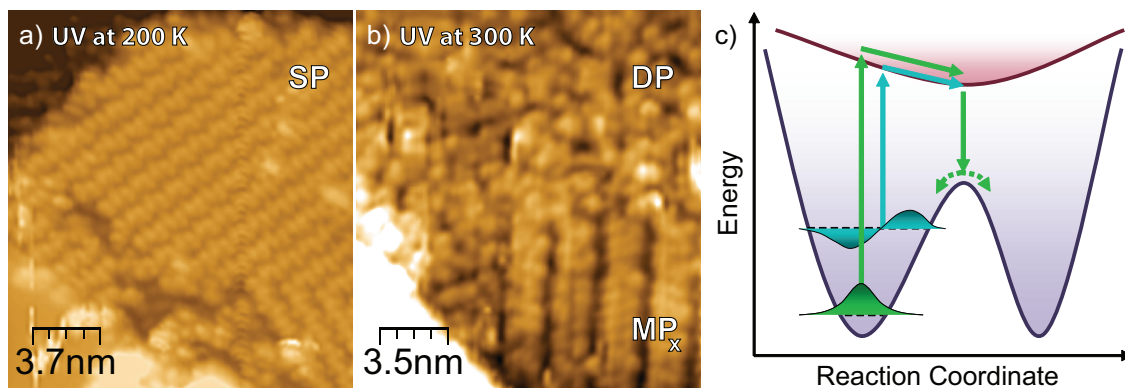


Figure 4.20: Resulting molecular structures after UV light illumination of  $\approx 900 \text{ J / cm}^2$  on a SP/Bi(110) sample at 200 K (a) and at room temperature (b): photoswitching effects and resulting new phases can only be observed at the higher temperature. c) Schematic drawing of the vibron-assisted photoswitching. Photoionization processes (i.e. adding an electron or hole from the metal into the molecule) can start from the ground state (green) or from a vibrationally pre-excited state (turquoise). Depending on the actual form of the potential in reaction coordinate space, the expectation value of a vibrational state may be situated closer to the switching barrier. As a result, the excited state can travel in shorter time into its minimum thus maximizing the probability to reach before a deexcitation takes place.

excitation from the HOMO into the unoccupied metal states, a change in the reaction's efficiency might be possible. The occurrence of the first of the two mechanisms can be excluded due to simple reasons: with a HOMO-LUMO gap distance of 3.5 eV, the 445 nm wavelength photons would not be able to excite this transition. In addition, we were able to induce a similar switching behavior with even less energetic light (red,  $\lambda > 525 \text{ nm}$  ( $h\nu < 2.4 \text{ eV}$ )). The second mechanism must be considered but is unlikely to cause the mentioned yield differences since the electron lifetimes are expected to be in the same order as for the anionic state.

To answer this question we have performed another set of experiments, where UV light was irradiated onto a sample at a temperature of 200 K (figure 4.20 a). A total illumination fluence of  $870 \text{ J / cm}^2$  did not affect the spiropyran monolayer to a noteworthy degree. If the same illumination was irradiated onto samples at room temperature, the whole monolayer turned into a mixture of DP and MP<sub>x</sub> patches. Such a strong dependence of a photo induced reaction's efficiency from the substrate temperature was found in desorption processes of small gas molecules on surfaces [117, 118, 119, 120], and also in photoswitching of tetra-tert-butyl-azobenzene (TBA) molecules on Au(111) [74, 121]. In the latter case, an increase of the photon cross sections of three orders of magnitude for a sample temperature range between 30 K and 200 K was found. The effect is explained

by an enhancement of cross sections of higher vibrational levels due to a shift in the reaction coordinate's expectation values into the direction of the barrier (figure 4.20 c). This reduced the time required for the ionized system to relax into its potential minimum, from where the other isomeric form can be reached. Starting from thermally preoccupied higher vibrational levels, the system thus switches more easily at larger temperatures. If we assume a similar process for the spiropyran/Bi(110) system, the low tunnel electron yield can be explained by the fact that all STM experiments were performed at 5 K where the yield of the very same mechanism can be reduced by 3 orders of magnitude.

## 4.5 Conclusion

In summary, we have shown that 6-nitrobenzopyrylospiran adsorbed on Au(111) and Bi(110) forms a similar type of self assembled island structure on both metals. On heating the structures to temperatures above 300 K, a thermally induced transformation into the isomeric merocyanine form can be evoked. The molecular assembly of this species differs on the two surfaces, but on both metals merocyanine appears as the most stable form of the two isomers. It turned out to be impossible to thermally switch the merocyanine molecules back into the initial spiropyran form again. This is in contrast to free molecules, where SP is known to be the most stable isomer. The reason for this stability inversion on the metal surfaces is the strong adsorption of the planar MC molecules. An additional stabilization is created by the zwitterionic character of the merocyanine molecules that leads to a strong interaction with the bulk bands of the gold substrate. These bands are missing on bismuth, where the molecules appear more neutral, what causes the different molecular patterns that were observed. The irreversibility of the  $SP \rightarrow MC$  switching might limit the potential for technological applications. Therefore, it is desirable to reduce the adsorption strength of the merocyanines. One possible way may be the use of thin oxide layers to achieve a decoupling from the metal substrate.

While the thermo switching process takes place at roughly the same parameters on both surfaces, great differences were observed for the photo-isomerization behavior. On gold, no clear evidence of any light induced switching processes could be found. On bismuth, on the other hand, a comparably high photo-switching yield for the ring-opening reaction was observed at room temperature. We believe that the molecular environment on bismuth resembles more the "free molecule" case than the one on gold. There, stronger interactions of the molecular orbitals with the metal bands quench the switching reactions by shortening the anionic state's lifetime. On bismuth, such interactions are reduced due to the lower density of states.

In addition, a temperature enhancement effect of the photo-isomerization was observed on bismuth. On a cooled sample, the photon yield was strongly reduced. A higher switching efficiency of vibrationally excited initial states is believed to be the origin. This effect



suggests the application of temperature as an additional parameter, besides the illumination intensity and wavelength, to achieve a higher control over the bidirectional switching of the isomers.

On bismuth, the system of mixed SP and MC molecules reveals a rich phase portrait. Light irradiation can be used to create the different reactant's ratios, that lead to the different self-assembly patterns. This is not possible for switching of molecules in a solution and can therefore be considered as a novel concept. At long illumination intensities, an equilibrium switching state is reached, what confirms that also backswitching reactions are induced by the light. Although we did not manage to transfer the system back to its initial state, we think that this might be possible with the appropriate light and temperature parameters.

As a final excitation method we showed that the molecules can also be switched by attachment of tunneling electrons into the LUMO. We believe that these events follow the same underlying reaction process as the photo-isomerization although the switching efficiency is reduced by three orders of magnitude. Therefore the most likely reason is that the experiments were conducted in an LT-STM at 5 K, where the quantum yield might be strongly reduced.



## Chapter 5

# Electronic Transport Through Mechanically Contacted Molecule Junctions

In this last chapter, we want to present another approach to investigate the modification of electronic transport through molecular junctions with vibrational degrees of freedom. Since this project is not yet finished, we will present our current results and give an outlook of further work at the end of the chapter.

Electrons transported through a molecular junction can interact with the different vibrational modes of the molecule. This influence of the electrons can lead to transport types that are either elastic or inelastic in nature. Elastic vibrational transport, i.e. the tunneling of electrons through vibronic levels, can be detected on tunneling at energies above an electronic resonance and results from interaction with vibrational modes of the ionized molecule. Inelastic processes typically include the direct activation of vibrational modes in the neutral or in the ionized molecule. Besides that, tunneling electrons can lose their energy into plasmonic excitations in the tip or substrate that further decay by photo emission [122]. This ability of the electrons to deposit energy in continuous amounts allows for numerous multi-step transitions, like the activation of an anionic vibrational mode and a subsequent decay into the ground state, that go beyond the processes that can typically be observed by IETS measurements. Many details of these inelastic transitions are still unknown. An ideal way to investigate them includes, besides the typical  $I_t(V_s)$  measurements, the detection and analysis of the emitted photon spectrum, what goes beyond the capabilities of a classical LT-STM. Therefore, we aim to include an optical setup to our experiment that will allow us to detect and analyze the photons that are emitted from a single molecule junction.

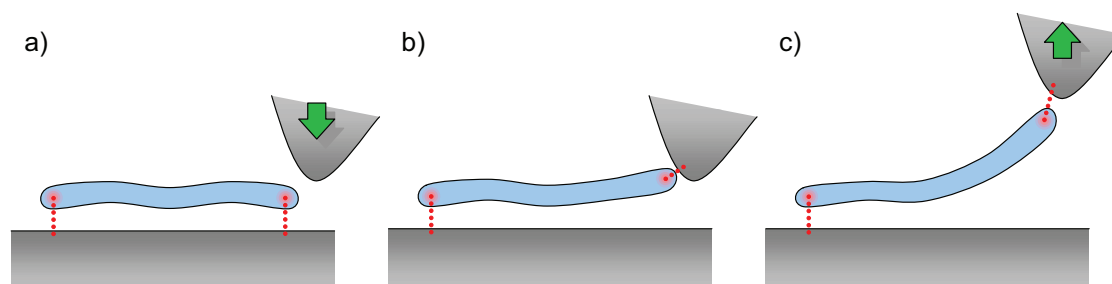


Figure 5.1: Schematic drawing of a “lifting-up” procedure as described in the text: a) the STM tip is approached close to a flat-lying molecule’s reactive end group. b) the bonding state of the end group is changed by convenient means in a way that a bond is established between the tip and the molecule. c) by retraction of the tip the molecule is pulled away from the surface into a more upright position. This situation ideally allows for elastic and inelastic transport measurements through the molecule.

An electron that undergoes such a two-step process, between different electronic and vibrational levels has to interact more than once with its environment during the time at which it is located inside the junction. Therefore a critical parameter for the effective realization of these processes is the lifetime of the electron on the molecule. If the time is long enough, the electron is more likely to undergo several transitions. To study these types of effects it is therefore necessary to find a system that is well decoupled from the surface to support longer electronic lifetimes. An ideal system would allow for tuning the decoupling strength, so the lifetime and therefore the electron yield for the processes under observation can be adjusted. This feature is found at a type of junction that is in the further label as “lifted-molecule junction”, where the STM tip is used to contact one end of an elongated molecule on the surface and to pull it slowly into an upright position. In this chapter we will investigate the capability of two molecular systems to form such a junction and we will further study the transport behavior of one by means of  $dI_t/dV_S$  measurements.

## 5.1 Contact Formation and Lift-Up

A contact between the STM tip and a single surface-adsorbed molecule allows a very controlled and thus well-defined interaction with the system, since the position of the LT-STM tip can be adjusted with a precision better than a tenth of an Ångström in all directions. With respect to junction control this method is therefore superior to the technique of mechanically controllable break junctions (MCBJ), the “classical” contact experiment, where only the  $z$  direction can be controlled with similar accuracy.

This degree of three-dimensional tip control allows to perform one special type of experiment, namely the “lifting” of a single elongated planarly adsorbed molecule [123, 124, 125]. The idea is to create a bond between the STM tip and one reactive end group of the molecule in a well-defined and reproducible way. Then the molecule is pulled into a more upright position by retracting the tip (see figure 5.1). This setting is quite convenient for observing conduction through molecular wires since the molecule is now in direct contact with the two leads while being at least partially decoupled from the surface. One advantage of the procedure is that presumably the details of the connection between tip and molecule vary only little between different lifting operations, compared to the MCBJ method. Since it is known that the character of the tip-molecule contact has considerable influence on the conduction behavior [11, 126] such a reproducibility is a prerequisite for spectroscopic investigations of the molecular properties.

The lifting-up of the molecule will also cause direct changes of the system’s properties: rotations or vibrations in the molecule that are quenched in a flat-lying geometry may become more pronounced and a partial decoupling of the molecule from the surface may alter the system’s electronic features like electron lifetimes, charge screening or bonding states [123, 127]. Apart from that, the lifted geometry may influence the sensitivity of the system to detect characteristic features, since the tip that unites manipulation device *and* detection probe is stronger coupled to the molecule in contact than in tunnel. One example is the different working mechanism of inelastic spectroscopy that is generally different in the two regimens: in the tunneling regime, as described in section 2.1.3, vibrational modes provide additional tunneling channels which give rise to peaks in the IETS spectra. In contrast to that, electron back-scattering at the same modes dominates the influence on the current in the contact regime, leading to a weakening of the current and therefore to dips in its second derivative [128]. Also intermediate peak shapes may be found [129]. In view of these features, the spectroscopic investigation of such a lifted-molecule system is expected to be quite rewarding.

The goal of our first set of experiments is, to follow and investigate the formation of a “lifted molecule junction”, starting at the flat-lying molecule over contacting with the tip to the final formation of a molecular bridge connecting the two leads. Beyond that, we want to find a suitable system that will allow for measuring of elastic and inelastic transport spectra and for observation of optical transitions in future experiments, as explained in chapter 5.3. Putting this together, we formulate a list of features the system under observation must fulfill:

- (i) the molecules must allow precise contacting of one end group to the tip
- (ii) the central part of the molecule must not bind too strongly to the substrate, so the molecule can be “stripped off” easily
- (iii) they should show sufficiently clear transport characteristics

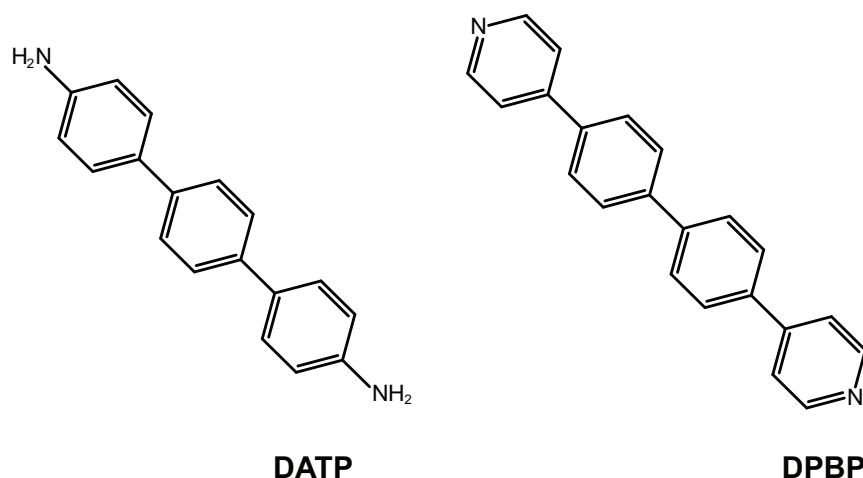


Figure 5.2: Lewis formula of the two molecules (from left) Di-Amino-Tri-Phenyl (DATP) and Di-Pyridyl-Bi-Phenyl (DPBP) that were investigated for their suitability as molecular bridges in a bi-contacted STM junction.

- (iv) they should be suitable for investigation of optical transitions
- (v) they should be preparable in UHV by evaporation

Taking these considerations into account, we decided to proceed with two poly-phenyl species, functionalized with different end groups. Namely these are *Di-Pyridyl-Bi-Phenyl* (DPBP) and *Di-Amino-Tri-Phenyl* (DATP), (see figure 5.2). With this selection, we cover the range of  $sp^2$  and  $sp^3$  hybridized nitrogen atoms at the anchoring groups to find out for which the best tip-molecule contact can be achieved. Typically, the formation of a dative bond between these end groups and the tip is expected, where the lone pair electrons of the nitrogen atom fill a bonding state to the coordinatively unsaturated transition metal tip atom [130]. As a consequence, the energy and geometric direction of the nitrogen lone pair electrons are of importance for the bond. As is shown schematically in figure 5.3, the lone pairs of the  $sp^2$  hybridized species (DPBP) are placed along the molecules' main axes, whereas the lone pair is found under an angle of about  $70.5^\circ$  from this axis for the  $sp^3$  type (DATP). The synthesis and purification of DATP was done by [131] and of DPBP by [132]. The moderate size of the molecules allows easy evaporation without the danger of breaking the structure.

In a first assumption one might assume that both types of molecules are good conductors, since the  $\pi$ -electrons may be delocalized over the complete length, according to valence-bond theory [133]. On the other hand, it is known that the conductance of such polyphenyls goes down, if the phenyl rings exhibit a stronger tilt angle  $\theta$  around the main axis (see figure 5.4). In fact, [134] could show that the transmission through the molecule

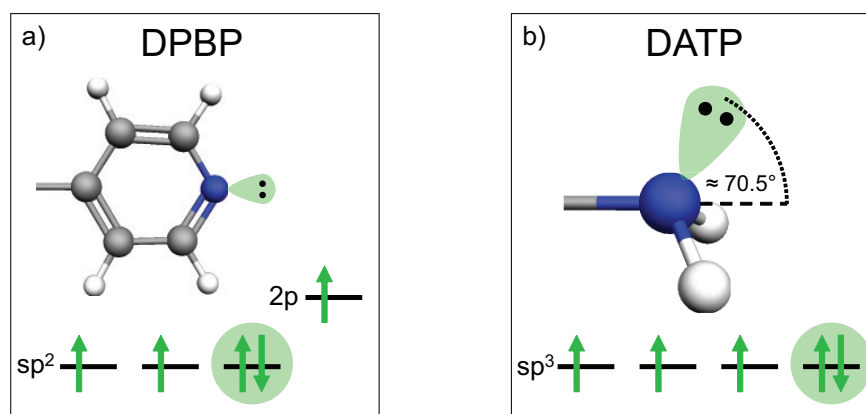


Figure 5.3: The two different hybridization states of the terminating nitrogen atom of Di-Pyridyl-Bi-Phenyl (a) and Di-Amino-Tri-Phenyl (b). A ball-and-stick figure of the respective end groups and a simplified energy scheme of the nitrogen atom's L-shell in the three different hybridization states are shown. The light green circles mark the lone pair electrons.

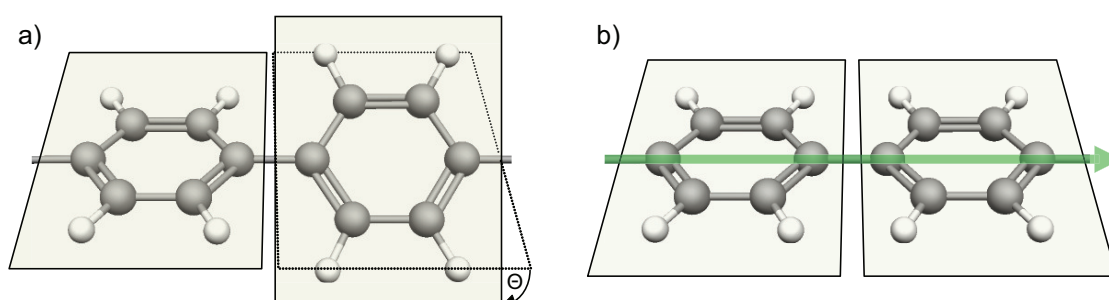


Figure 5.4: a) Definition of the tilt angle  $\theta$  between neighboring phenyl rings. A  $\theta$  of  $\approx 40^\circ$  is found for a neutral molecule. b) The anionic molecule is rather flat, the conductance is high.

is damped at every phenyl-phenyl connection by a factor of  $\cos^2(\theta)$ . The ground state angle of DATP, for example, is  $\theta \approx 36^\circ$ , what implies a reduction of more than 50%. If the central phenyl ring is free to rotate,  $G$  can be reduced to less than 25% of its original value. Together with additional damping at the connection points to the leads, this effect reduces the conductance of this molecule to be lower than  $0.2 \cdot 10^{-4} G_0$  for low voltages (25 mV) [134].

The tilt angle  $\theta$  also has a second important implication on the expected transport behavior. While the tilting of the phenyl rings is rather high for the neutral polyphenyl ( $\approx 40^\circ$ ), the anionic species is found to be flat. Therefore, a strong coupling between the phenyl frustrated rotations and the transition between neutral and anionic state can be expected. One possible result of such strong coupling may be the apparition of enhanced inelastic



features in the  $dI_t/dV_s$  or  $d^2I_t/dV_s^2$  spectra like vibronic or IETS peaks. Depending on the type of transport, also the yield for photon emitting deexcitations may be intensified, as described above. As a final goal, we want to study these different effects of the  $\theta$  degree of freedom on the transport behavior by means of STS, IETS and photo spectroscopy.

In a first set of experiments, we study the adsorption behavior of the two molecular species and we test, which end group is most suitable for performing the “lifting-up” experiments as described above. We use low-index copper surfaces as substrates since they may provide a good balance between a weaker binding of the phenyl ring bodies and a stronger anchoring of the end groups. The evaluation of the lifting experiments refers to three general questions: how difficult is it to form a contact junction by lifting of the molecules, how stable is the junction and how reproducible are the resulting data. In a first section, the results and details of the molecular adsorption are given, followed by the description of the lifting experiments.

### 5.1.1 Di-Amino-Tri-Phenyl on Cu(100)

Amino end groups, as in DATP, have been used in contact experiments of Venkataraman *et al.*, where they were found to form reliable bonds to Au metal contacts [135, 136]. There, the molecule-surface contact was established by the  $sp^3$ -hybridized nitrogen atom, binding by its lone pair electrons to an coordinately unsaturated Au adatom on the surface. We assume that a similar type of bond can be formed to unsaturated copper atoms. We find that the molecules form linear chiral chains on the surface that are bonded by intermediate single copper atoms.

#### Chiral Structures of DATP

The molecules were prepared at a coverage of about 14 % of a monolayer (figures 5.5). In the STM images the molecules appear as elongated protrusions with a central height of  $\approx 1.0$  Å. During the evaporation, the Cu(100) surface was at room temperature, what results in a molecular assembly in clusters with a tendency to form mostly linear molecular chains with a length of up to seven molecules. The molecules in these chains arrange in a head-to-tail alignment, but with a clear transversal shift between each two neighbors, what results in a staircase-like appearance (figure 5.5 b). As benchmark numbers for these steps we can extract the step height  $d_s$  and the (projected) next neighbor distance  $d_l$  from the STM images as shown in figure 5.6 a), and calculate the step ratio  $R_{\text{step}} = d_l/d_s = 2.9 \pm 0.3$  and the angle  $\alpha = 19.1^\circ \pm 2.4^\circ$  between the symmetry axis of one molecule and the chain direction.

One characteristic feature of the undisturbed chains is that they show a chiral structure, i.e. a single chain has either only steps to the right or to the left. Regarding the question what

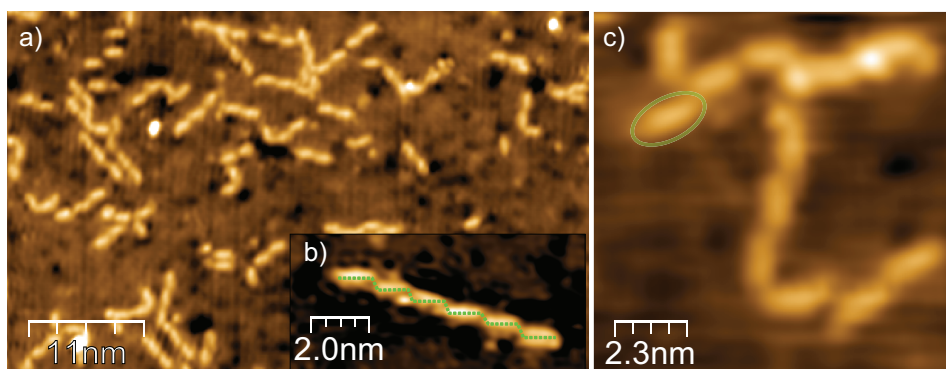


Figure 5.5: STM images of DATP molecules on a Cu(100) surface prepared at room temperature. a) Overview over a larger region. The molecules arrange in disordered clusters with a tendency to form linear chains. Dark spots on the surface are caused by impurities. b) Molecular chain of six molecules. The staircase-like chain structure is marked. c) Close-up of a molecular cluster. A single molecule is marked by the green ellipse. Feedback parameter of the images are: a)  $I_t = 0.1$  nA,  $V_s = 0.7$  V, b)  $I_t = 0.2$  nA,  $V_s = 1.1$  V, c)  $I_t = 0.11$  nA,  $V_s = -1.0$  V.

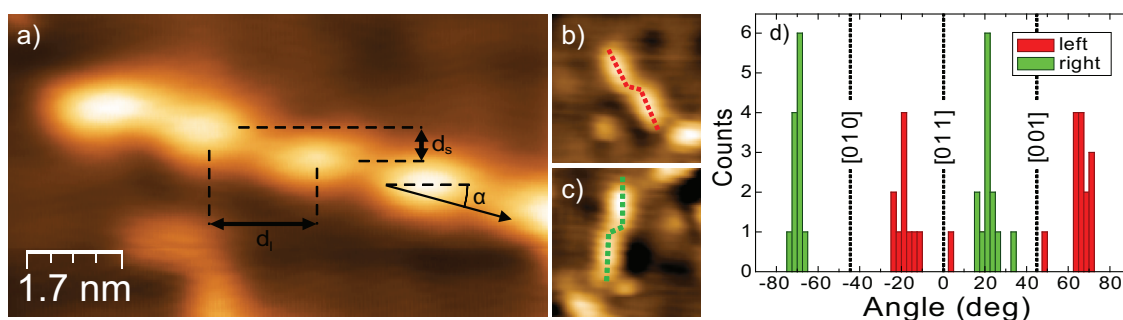


Figure 5.6: a) staircase-like DATP chain of the “right” type. The sketched distances  $d_l$  and  $d_s$  are  $d_l = 17.2 \pm 0.9$  Å and  $d_s = 6.0 \pm 0.7$  Å. The image parameters are  $I_t = 0.1$  nA and  $V_s = 0.7$  V. Images b) and c) show short chains of the “left”- and “right”-type, consisting of two molecules each. The images are  $5.7 \times 5.7$  nm in size, the scanning parameters are  $I_t = 0.1$  nA,  $V_s = 0.7$  V. d) statistical analysis of the directions of 50 molecular chains. “Left”-chains run in the  $-18.5^\circ \pm 2.5^\circ$  and  $67.1^\circ \pm 1.7^\circ$  directions and “right”-chains into the  $-69.6^\circ \pm 1.2^\circ$  and  $21.0^\circ \pm 1.5^\circ$  directions. All errors as  $2 \times \text{SEM}$ .

causes this behavior one might look at a single molecule, but from the first view it is not clear if DATP that is symmetric in structure has an intrinsic chirality on the surface or not. Since also a non-chiral adsorbate can form a chiral system together with the underlying surface lattice and therefore build chiral assemblies, we need to take a closer look to the orientation of the chains for answering this question.

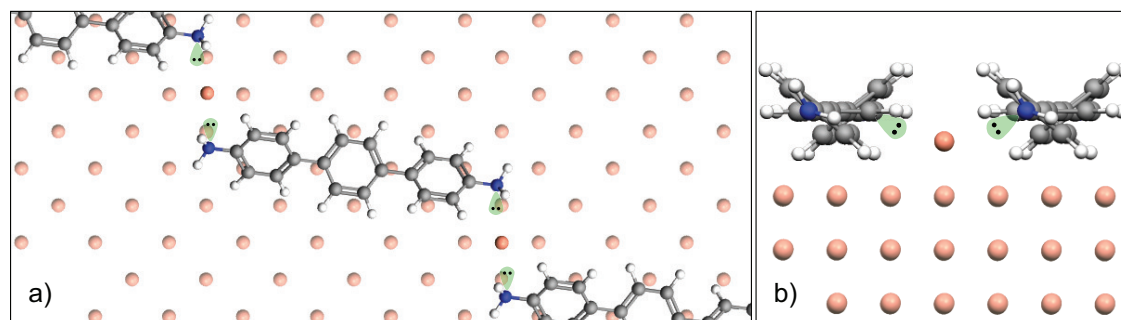


Figure 5.7: a) and b): Top and side view of a proposed model of the structure of a “right”-handed chiral chain of DATP on a Cu(100) surface as described in the text. The binding of the molecules is here mediated by a copper adatom sitting on a position of the following layer (full color). Structural values of this model are:  $\phi = 18.4^\circ$ ,  $d_l = 15.3 \text{ \AA}$ ,  $d_s = 5.3 \text{ \AA}$ , what results in  $R_{\text{step}} = 2.9$  and implies a piezo missadjustment of 13 %. Nitrogen lone pair electrons pointing towards the copper adatom are indicated.

To distinguish the two chiral forms we will introduce the nomenclature of “right-hand”- and “left-hand”-type chains here. “Right” types have their steps to the right and “left” types to the left as it is shown in figures 5.6 b) and c). One remarkable feature of the two types is that the handedness of a chain is linked to its orientation on the surface. Figure 5.6 d) shows a statistical analysis of the heading angles of 50 chains with respect to the [011] direction<sup>1</sup>. It can be seen from the histogram that each chirality has two favored heading directions, separated from each other by  $\approx 90^\circ$ . This is due to the  $90^\circ$  rotational symmetry of the Cu(100) surface. With respect to the [011] or  $[01\bar{1}]$  direction, the right-handed chains are aligned under an angle of  $\phi = 20.7^\circ \pm 2^\circ$ , while the sign of  $\phi$  is opposite for the left-handed chains.

With this we can find a periodic chain structure that is commensurate to the Cu(100) surface lattice and matches best the values  $\phi$ ,  $R_{\text{step}}$ ,  $d_l$  and  $d_s$ . This model is shown in figure 5.7 and explained below. It is apparent that the transversal distance  $d_s$  of  $5.3 \text{ \AA}$  is too large for being bridged by hydrogen-bonds and we must therefore exclude a model with only direct molecule-molecule interactions. Instead we suggest a different bonding mechanism that in addition can explain the chiral structure of the chain. As we see from a DFT minimization calculation<sup>2</sup>, each phenyl ring of the neutral free molecule has an angle of  $36^\circ$  with respect to its neighbor thus giving a spiral shape to the molecule. The lone pair electrons of the two  $sp^3$  hybridized nitrogen atoms point into a direction that is approximately perpendicular to the phenyl rings holding the respective amino group. We may suppose that the molecule keeps some part of its spiral character on the surface

<sup>1</sup>The [011] direction can be determined from images showing straight [011] and  $[01\bar{1}]$  step edges that form close to tip crash sites due to their energetic favorability [137].

<sup>2</sup>Calculated with Gaussian, B3LYP, basis set 6-31G, polarization 2d 2p.

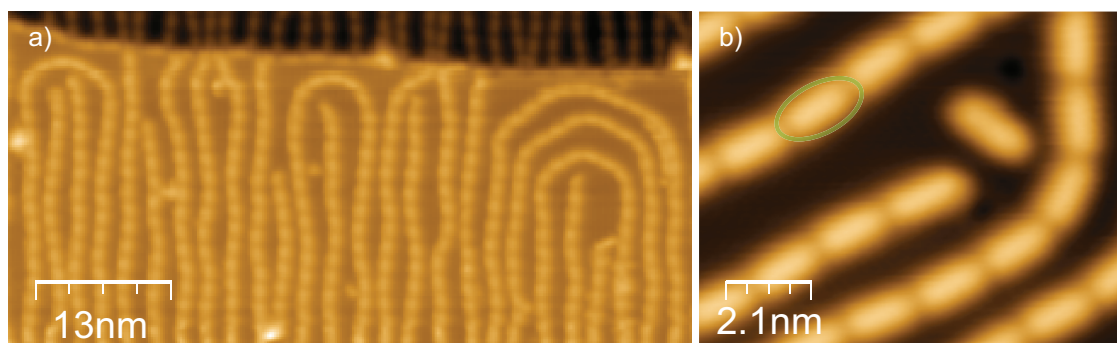


Figure 5.8: DPBP molecules on a Cu(111) surface. In the small scale image a single molecule is marked by a green circle. The apparent length of one molecule  $18.4 \text{ \AA} \pm 0.1 \text{ \AA}$ . Feedback parameters are: a)  $I_t = 0.2 \text{ nA}$ ,  $V_S = 1.1 \text{ V}$ , b)  $I_t = 0.2 \text{ nA}$ ,  $V_S = 1.0 \text{ V}$ .

[138]. As in [135], the nitrogen atom's lone pair can bind to a copper adatom or to a surface atom that is then pulled out of the surface by the binding in such a configuration. The transversal distance between two molecules binding to the same copper atom can in this way be larger than in the case of direct hydrogen bonding. Another DATP that may bind to the free end of the last molecule will not find both binding directions to be equally favorable: the spiral structure of the molecule in the chain, in combination with its alignment to the substrate and the position of the adatom (or atom that is pulled out), will cause the side to be a preferred bonding site for the next copper/DATP link that is opposed to the former bonding direction. A binding to the same side is prevented by steric hindering. This effect can explain the chiral growth of either "left"- or "right"-handed chains.

### 5.1.2 Di-Pyridyl-Bi-Phenyl on Cu(111)

As second molecule we examined DPBP on a Cu(111) surface. The molecules were evaporated onto the copper samples held at room temperature. The molecules appear with an elongated shape, similar to DATP. Their apparent height is  $1.4 \text{ \AA}$ . On Cu(111), the molecules order in linear head-to-tail chain arrangements (figure 5.8). A direct molecule-molecule interaction in this form is quite unlikely, since the pyridine end groups have nitrogen atoms in the terminating position, exposing their lone pair electrons into the same direction. We therefore believe that, similar to the case of DATP, the binding is mediated by a Cu adatom.

The chains usually try to avoid open ends and show a strong affinity to start and end at the lower side of a copper step edge (see figure 5.8 a). This characteristics also shows the high affinity of the pyridine end group to bind to accessible copper atoms. The upper side of step edges typically supports no favorable binding sites for the chains. The chains

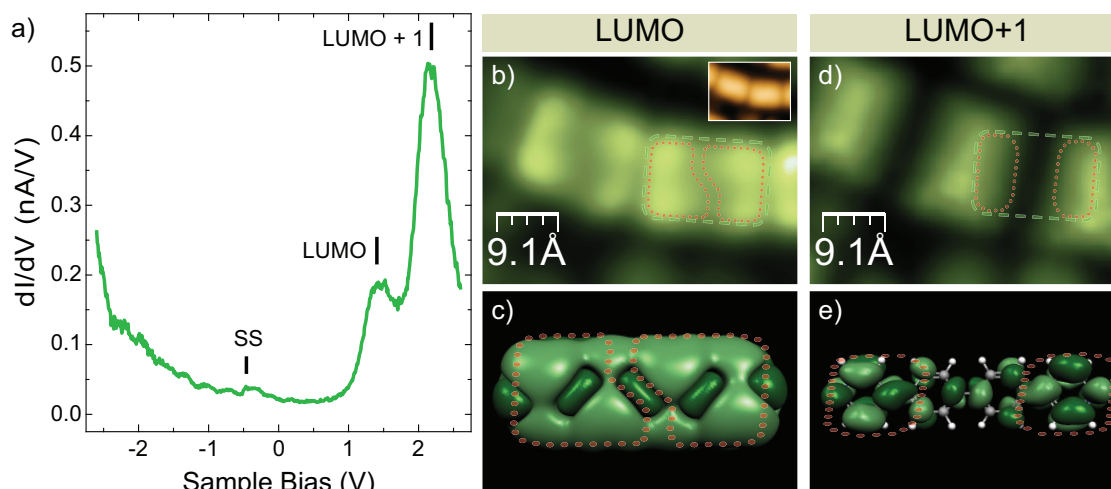


Figure 5.9: a):  $dI_t/dV_S$  curve of DPBP on Cu(111). The LUMO and the LUMO+1 (marked) can clearly be seen at values of  $1.4 \text{ eV} \pm 0.1 \text{ eV}$  and at  $2.2 \text{ eV} \pm 0.1 \text{ eV}$ . The modulation was 20 mV. Additionally, the onset of the Cu(111) surface state is marked at  $-0.45 \text{ eV}$ . b):  $dI_t/dV_S$  map at  $V_S = 1.5 \text{ V}$ . The inset shows the topography image of the same region. One molecule of the chain is marked in the map by a green dashed line. The internal structures described in the text are marked by a red dashed line. d):  $dI_t/dV_S$  map of the same region at  $V_S = 2.1 \text{ V}$ . The same molecule is marked by the green line. The red line marks the dominant features on the rim of the molecule. Feedback current of b) and d):  $I_t = 0.2 \text{ nA}$ . c) and e): DFT calculated iso-surfaces of the DPBP LUMO and LUMO+1. The energetic difference between the levels is  $0.7 \text{ eV}$ . The red dotted line marks equal structures as in the  $dI_t/dV_S$  maps. The reason of the structure in b) and c) is the phenyl tilting angle  $\theta$ , as explained in the text. d) and e) have their major contribution on the molecule's endings.

tend to arrange approximately parallel to one of the three high symmetry directions of the Cu(111) surface, but with a certain flexibility to follow arbitrary directions. This is a sign that the binding of the molecules to the substrate is not too strong.

To elucidate the electronic properties of the DPBP molecules on the Cu(111) surface, we performed STS measurements on the system. A typical spectrum is shown in figure 5.9 a): while no occupied molecular orbital can be detected, two distinct unoccupied resonances are clearly visible at  $1.4 \text{ eV}$  and  $2.2 \text{ eV}$ . We identify these resonances as LUMO and LUMO+1. Depending on the position of the measurement, their relative height with respect to each other changes significantly. The reason for this are big differences in the spacial distribution of the orbital's density, what can be seen best in the  $dI_t/dV_S$  maps b) and d) of figure 5.9: while the LUMO resonance at  $1.5 \text{ eV}$  shows a shape that is rather homogeneously distributed along the molecule, the map of the LUMO+1 resonance at



2.1 eV shows the highest signal between two joining molecules, implying a high density of this orbital on the pyridine end groups.

Shape and energetic values of the two unoccupied resonances as seen in the  $dI_t/dV_S$  maps are in good agreement with DFT calculations of the neutral gas phase molecule<sup>3</sup> (see figure 5.9 c and e). The calculated iso-surfaces as well as the  $dI_t/dV_S$  maps show the LUMO+1 resonance to be mostly located on the end parts of the molecule (figures 5.9 e and d). At the maps, the area of this resonance tends to merge with the one of the neighboring molecule, resulting in one region of high conductance located between the two molecules. Despite the good agreement with the calculation, we cannot completely rule out the possibility that this resonance is associated with the copper adatom connecting the two molecules. A similar correspondence between iso-surface and  $dI_t/dV_S$  map can be found for the case of the LUMO. This is more evenly distributed along the molecule than the LUMO+1 (figures 5.9 c and b). Two dominant structures with an interlocked shape (red dotted lines in figures 5.9 c and b) are present in both visualizations. An analysis of the calculation reveals the origin of these structures: an alternating tilting of the phenyl rings, as it was formerly found for the DATP species, leads to the observed zig-zag-pattern. That polyphenyl molecules keep their tilted gas phase structure when adsorbed on a transition metal surface was also found by Braun *et al.* for a Ag(111) surface [138].

### 5.1.3 Lifting Properties

In this section we describe and discuss the results of the contact and lifting experiments that were performed on the two molecular species. For contacting a molecule we place the tip over one end of it and open the feedback loop. Then, the bias voltage  $V_S$  is set to an appropriate value before the tip is first approached several Ångströms towards the sample. We then retract the tip either directly or after a short time span ( $\sim$ one second). The transport current  $I_t$  is recorded during the complete procedure. The approach distance was adjusted to be the shortest distance that led to contact in a reasonable amount of trials. The tip-sample-bias was varied over a range of -1.0 V to 1.0 V. The contact formation between tip and molecule is often discernible by a deviation of the conductance  $G$  from the exponential tunneling regime, e.g. as a sudden increase of  $G$ , as described in chapter 3.1. If the formed contact is stable enough, the molecular bond does not break during the first phase of retraction, what manifests in a  $G(z_{\text{appr}})$  curve that clearly differs from the tunneling behavior that was observed during the approach. If the tip-molecule contact finally breaks,  $G$  drops down to its original tunneling state value. The distance between contact formation and contact breaking can thus be deduced from the  $G(z_{\text{appr}})$  curves and is labeled as  $z_{\text{retr}}$ .

<sup>3</sup>Calculated with Gaussian, B3LYP, basis set 6-31G.

### Lifting Properties of DATP

We focused our efforts to contact the molecule mostly on the free ends of the stepped chains of DATP since we expect that these ends can be removed more easily. The typical tip approach distance in our experiments was between 5 and 7.5 Å from the tunneling region. To achieve a controlled contact turned out to be not very easy: in over 50 % of the attempts that showed a significant deviation of  $G(z_{\text{appr}})$  from tunnel,  $G$  raised to values orders of magnitudes larger than  $G_0$ . This indicates that a direct tip-substrate contact has been formed instead of a tip-molecule-contact. The subsequent imaging of the area confirmed this assumption. The other cases typically show contact conductances between  $0.3 G_0$  and  $25 G_0$  and mostly lead to significant non-reproducible changes of the molecules' appearances in the STM images as well. Only a small fraction of less than 1 % of the attempts lead to a stable and reliable contact. One of these events that was realized at a bias voltage of 300 mV is shown in figure 5.10. The sketches depict the situations during the three stages of the operation. During the approach, the exponential behavior of  $G(z_{\text{appr}})$  shows that the electron transport can be described best as tunneling process. At the closest point, a tip-molecule contact is formed, but this cannot be noticed at this moment since no change of  $G$  is observed. The new transport channel that is added to the junction upon contact formation is small compared to the direct tunneling transition amplitude. It gets visible as the tip is again retracted:  $G(z_{\text{appr}})$  persists at a value of  $\approx 9 \cdot 10^{-3} G_0$ . This is about 50 times the value that was reported for this molecule on break junctions measurements at a lower bias voltage (25 mV) [134].

We want to address the question, why the formation of a tip-molecule contact could be achieved only in so few cases, after the amino end group has been described in the literature as a good linker group [134, 135]. One possible explanation may be related to the way the molecules are bonded with their end groups as explained above. The lone pair electrons of the terminating nitrogen atoms are faced towards the connecting copper adatom and therefore towards the surface. For contact formation with the tip it is necessary to invert the direction of this hybridization state in such a way that it is pointing away from the surface. This is only possible if the two bonds connecting the hydrogen atoms of the amino group are rearranged. Pascual *et al.* have achieved such an inversion for ammonia molecules by activation of appropriate molecular vibrations [139]. However, this requires a sample bias setting that allows for inelastic excitations of these modes. In our case we could not find any dependence on the used sample bias voltages (0–170 mV, 0.3, 0.5, 0.6, 1.0 V) but it stays nevertheless likely that the bond formation is hindered by the required atomic redistribution. The MCBJ approach, on the other hand, does not face these problems: there, the molecules, coming from the solution, have an equal probability to bind on either of the two leads.

Summarizing, the contacting and lifting efficiency of DATP molecules with the STM tip turned out to be poor, because of the large rate of failures that considerably change the tip and destroy the probed molecules.



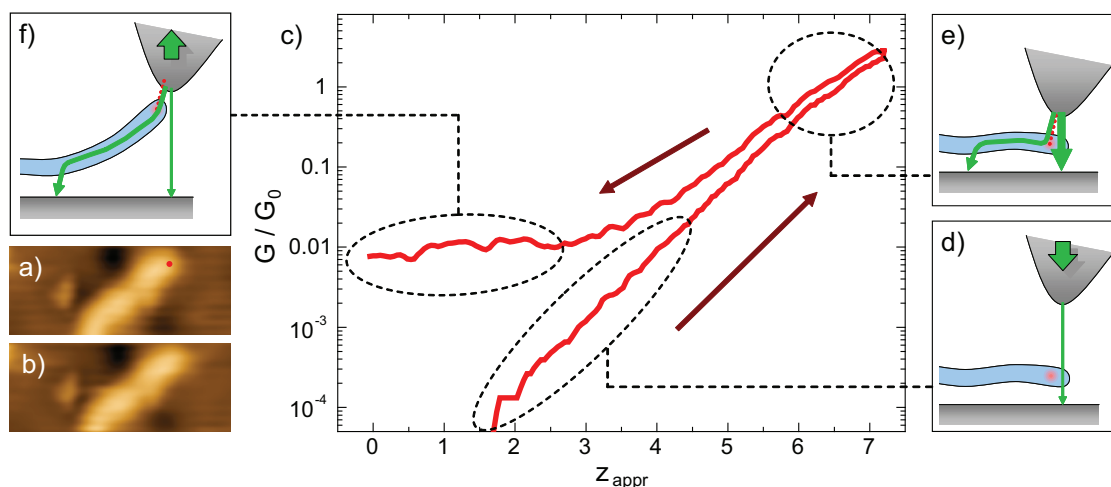


Figure 5.10: The successful DATP contacting event described in the text. a) and b) are STM images of the respective molecule before and after the operation. The point of the manipulation is marked red. c) shows the conductance curve during the operation. The different stages are marked and connected to the respective sketches (d–f): the tunneling region (d) is followed by the contact formation (e). The green arrows mark the different transport channels, their size depicts their intensity. On retraction, the transport channel through the molecule gains in importance (f). The sample bias during the operation was  $V_S = 0.3$  V.

### Lifting Properties of DPBP

A different behavior was found for the DPBP molecules on the Cu(111) surface. As in the case of DATP in many cases a sudden increase of  $G$  indicates the establishment of a tip-molecule contact, but the typical values of  $G$  are now considerably smaller, in the order of  $0.1\%$   $G_0$ . The contact curves show a comparatively high degree of reproducibility ( $\sim 80\%$ ). One typical curve is shown in figure 5.11. The interpretation of the different stages is similar to the DATP curve presented in figure 5.10: during approach,  $G(z_{\text{appr}})$  shows an exponential growth as it is typical for a tunneling junction. At a value of about  $3 \cdot 10^{-4} G_0$ , a number of sudden jumps of  $G$  to higher values indicate the contact formation and the opening of additional channels for the electrons to cross the junction. On retraction, the conductance decreases in a curve that clearly deviates from the pure tunnel behavior. Another downward jump occurs when the contact breaks, usually after retracting the tip for distances between 2 and 8 Å. The molecule usually stays intact after such a procedure and may change its position slightly.

We performed experiments to study the dependence of successful contacting on the tip's position and on applied bias voltage, shown in figure 5.12 a) and b). As demonstrated there, a contact can be formed only if the tip is approached to a free end of a molecule

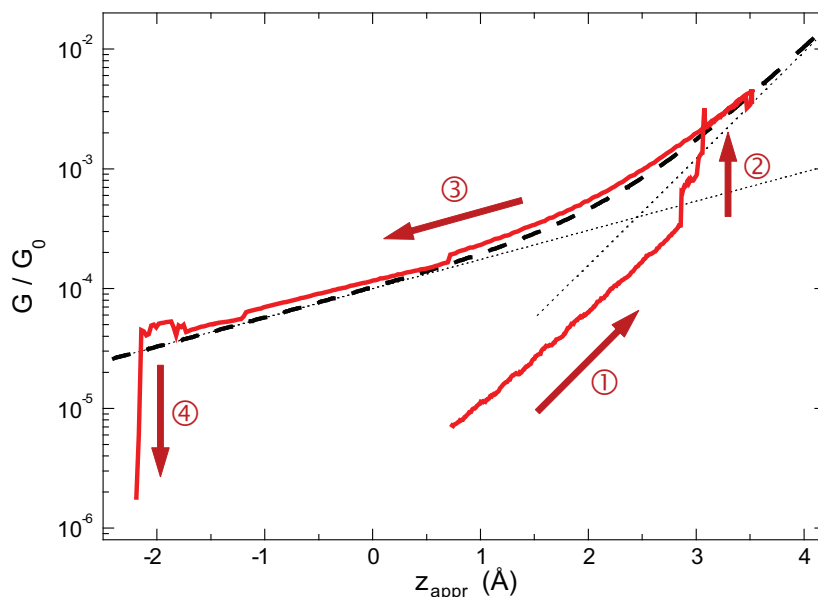


Figure 5.11: Typical lifting operation conductance curve  $G(z_{\text{appr}})$  of DPBP on Cu(111): an exponential increase (①) of  $G$  in the normal tunneling state is followed by a “jump to contact” (②). The conductance then follows the model of two independent tunneling channels (③) until, at large retractions, the contact opens again (④). The bold dashed line is a fit of the model to the average of 90 different curves. Thin dashed lines mark the two independent tunneling conductances. Feedback parameters:  $I_t = 0.2$  nA,  $V_S = 1.0$  V; sample bias during operation:  $V_S = 90$  mV.

that is not bonded to another molecule. In addition, contact could only be formed with negative or low positive sample bias ( $< \sim 150$  mV). These findings make it plausible that the observed jumps of  $G$  occur if the pyridine end group is drawn to the tip by the electric field. We therefore cannot safely attribute this jump to the formation of a chemical bond, and have to leave the question of the bonding details open.

The reproducible retraction curves  $G(z_{\text{appr}})$  can be described by a model of two idealized transport channels. One channel represents the “normal” tunneling through the vacuum gap, while the other can be viewed as an additional tunneling path through the molecule (compare figure 5.10 f). Since the molecule exhibits no resonant state around the Fermi level (i.e. at the energies of the electrons), the electrons have to tunnel along the complete molecule for the second transport channel. While the rigid molecule gets further lifted, the fraction of it that lost contact to the surface increases linearly, what leads to the deviating  $z_{\text{appr}}$ -dependence. On the molecule, the electrons experience a lower energetic barrier than in the vacuum due to the lower “energetic distance” to the unoccupied molecular orbitals. This explains the reduced slope of the  $G(z_{\text{appr}})$  curve. The total fitting function is therefore taken to be  $G = G_1 + G_2$  with  $G_i \sim \exp(\beta_i \cdot z_{\text{appr}})$ . The fit to an average of 90 different curves is plotted in figure 5.11. The resulting vacuum gap damping factor  $\beta_1 = 2.1 \text{ \AA}^{-1}$

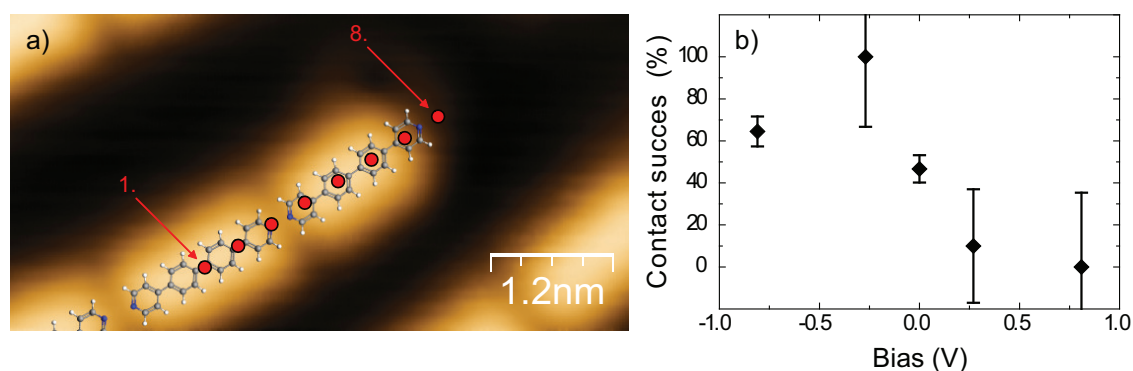


Figure 5.12: a) Image of a DPBP chain end on Cu(111) with a model of the molecules. The red dots denote a series of contact experiments that was taken to determine the dependence of the contact experiment's success rate on the lateral position. Only on the last two positions (7. and 8.) contacts could be formed. Image parameters:  $I_t = 0.2$  nA,  $V_S = 1.0$  V; contact parameters:  $V_S = 0.1$  V. b) Statistic of successful contact experiments of DPBP on Cu(111), depending on the bias voltage  $V_S$ . Errors as SEM.

is close to the expected value on Cu(111) ( $2.28 \text{ \AA}^{-1}$ ). The damping factor for tunneling through the molecule is found to be  $\beta_2 = 0.56 \text{ \AA}^{-1}$ . This is a typical value for organic molecules [124, 140, 141, 142, 143].

## Comparison

As we see, the affinity of the system to form a tip-molecule bond depends strongly on the choice of the binding end group and its initial bonding state. For the DATP molecules, a contact formation was very difficult to achieve. The valence states of the amino group's nitrogen atom are  $sp^3$  hybridized, with the lone pair electrons involved in a chemical bond with the surface and thus opposing the tip. It is plausible that this configuration makes it difficult to form a bond with the tip, what includes the breaking of the existing bond as well as a displacement of the two amino hydrogen atoms. In contrast to this, the DPBP molecules have their lone pair orbitals and thus their preferred binding direction aligned along their main axis so it can be more easily accessed by the tip. Bond formation was found to be more favored in this case. Unfortunately we cannot give a clear statement about the type of bonds that are formed between molecule and tip. Since it was not possible to pull the molecule into a complete upright position, as it was achieved by [123, 124, 125], we cannot exclude that the formed bonds are of a weak van-der-Waals-like character.

Aside from the ability to form point contacts, the stability of the lifted-molecule junction is another key feature of the system. In view of this, we found that both molecular species

turned out to be stable in the junction for pulling distances up to 8 Å. For a rigid molecule, this would correspond to a tilting angle between 30° and 40°.

Finally, a useful molecule-lifting process needs to be reproducible to a certain degree. An evaluation of the reproducibility of the DATP/Cu(100) junctions was not possible due to the small number of successful lifting events. For an adequate analysis of this system, large statistics are needed, that are difficult to obtain with STM methods. On the other hand, the DPBP/Cu(111) system was found to generate conductance curves on retraction  $G(z_{\text{appr}})$  of a high reproducibility that can furthermore be explained by a simple two-way tunneling model. This simplicity makes the system attractive for a further spectroscopic investigation, that is presented in the following section.

## 5.2 Spectroscopic Analysis of the DPBP Bridge Junction

It was shown in the last section that DPBP molecules can be used to build up metal-molecule-metal junctions with a high reproducibility. Our goal is to further investigate the type of electron transport through these junctions. STS measurements can provide information about the electronic character of the system.

To measure  $dI_t/dV_S$  spectra of a lifted-molecule junction, in principle the same procedure as was described in the last section was used. At first, we positioned the tip at a certain distance over a molecule's free end. After switching off the feedback loop, the tip was approached 3.5 Å towards the molecule. We used a sample bias of  $-0.81$  V since contact formation is favored at negative voltages, as described above. Then the tip was retracted  $z_{\text{retr}}$  Ångströms, where its position was fixed for the ramping of the voltage over the interval of interest. It turned out to be more efficient to ramp over the negative values of  $V_S$  first since the contact can easily break off positive voltages.

The spectra thus taken show a number of features that are not typical for  $dI_t/dV_S$  spectra of normal tunnel junctions. First, different spectra show some deviations from each other, even if taken with the same tip on the same position over the molecule. Second, in some events a bi- or tristability of the system manifest in a telegraph noise with increasing switching frequency for increasing voltage and current magnitude. Third, the positions of the LUMO resonances shift to higher values than in the tunneling spectra and fourth, the tip-molecule contact of all observed junctions broke off during the recording of the spectrum, at the latest when the LUMO starts to be populated by tunneling electrons. Therefore, typically only the resonance's onset is visible (see figure 5.13) that can be determined by the procedure described in appendix A.1. From the first two features we can conclude that the system does not reside in one unique contact configuration. Instead,

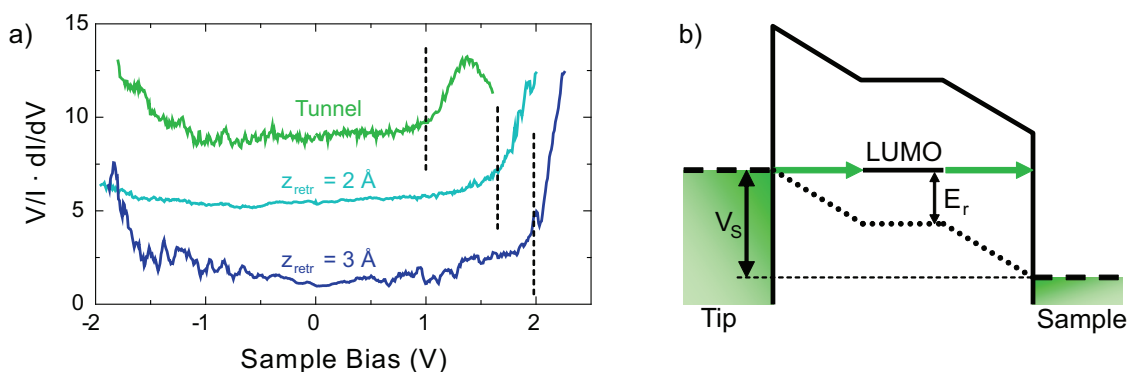


Figure 5.13: a) Examples of normalized  $dI/dV_s$  curves taken in tunnel (green curve) and in contact after retraction of 2 Å (turquoise) and 3 Å (blue). Dashed black lines show the LUMO onset positions. It should be noted that the measured onset positions can vary over a range between 1.2 V and 2.2 V. The green and turquoise curves are shifted upwards for clarity. The method for assignment of the onsets is described in appendix A.1. b) Schematic drawing of a symmetric junction with two tunnel gaps on either side of a central resonance (LUMO with energy  $E_r$  above the Fermi level). The sample bias  $V_s$  that needs to be applied to tunnel through the resonance is two times  $E_r$ .

a certain number of contact structures are realized, that differ in geometric and electronic details.

Major variations can be found in the apparent onset positions of the LUMO peak. Two different spectra taken in lifted-molecule conformations are shown together with a spectrum measured in tunnel in figure 5.13 a). The onset of the LUMO that is measured in the tunneling case is at 1.0 V. If the molecule is lifted for 3 Å or more, the onset is found at approximately 2.0 V<sup>4</sup>. This behavior is not surprising since the lifted-molecule junction is expected to be more symmetric, compared to a classical tunnel junction. In a symmetric junction, resonances are positioned in between two equal tunnel gaps (see figure 5.13 b). The applied voltage potential drops equally on both sides of the resonance. The consequence is, that the applied bias needs to be two times as high to tunnel through the resonance as in the asymmetrical (normal) case. The observed LUMO onset that is in the order of two times the tunnel value confirm this picture in our case.

An additional effect that may further promote the increase of the LUMO onset is the fact, that the molecule slowly leaves the proximity of the surface when it is lifted. Therefore, it leaves the region where screening by substrate electrons usually reduce the level of the measured LUMO (actually the electron affinity, see 2.1.2) This also results in a certain upwards shift of the unoccupied resonances. On the other hand, the molecule is expected

<sup>4</sup>For retraction heights  $z_{\text{retr}}$  smaller than 3 Å, the LUMO onset shows a tendency to decrease to 1.0 V when decreasing  $z_{\text{retr}}$  to zero.

to experience a stronger screening from the tip during the lifting experiment. Nevertheless a contribution of this effect to the observed shifts cannot be excluded.

Regarding the fact that it turned out to be impossible to raise the tunneling voltage up to a value where the maximum of the LUMO is reached, we conclude that the breaking of the tip-molecule bond is a direct result of the population of this resonance. Vibrational excitation by electron-phonon scattering is increased as more electrons are transported through the LUMO. A major candidate for these vibrations are phenyl-phenyl frustrated rotations, as discussed above. These vibrations will inevitably lead to a geometric distortion inside the tip-molecule bond region that, in combination with the electrostatic effects of the positive bias voltage, makes it likely for the molecule to “hop” off from the tip. Insofar we may take the contact breakdown behavior as indirect experimental indication for an effective coupling between the anionic state of the molecule and a number of its vibrational modes.

### 5.3 Conclusion and Outlook

In this section, we examined the suitability of the two molecule/substrate systems DATP / Cu(100) and DPBP / Cu(111) to form a stable metal-molecule-metal junction and to allow for electronic transport through their resonant levels. The DATP molecules arrange in stepped chains on the surface whose structure can be explained by a copper adatom mediated molecule-molecule bonding. The details of this bond, i.e. the orientation of the amino groups binding orbital may be the explanation for the very poor probability for contacting the end group with the tip, that was observed. A successful contacting and lifting event was further analyzed that shows that the lifting is in general possible.

DPBP molecules were found to form long chains on the surface that are bonded by an adatom mechanism that is quite similar to the one of DATP. Here the two-dimensional shape of the anchor group enhances the contacting probability since the STM tip can access the critical region more easily. Highly reproducible conductance curves show the mechanism of transport in a lifted- molecule junction. The molecule provides an additional tunneling channel that becomes dominant when the molecule is slowly removed from the surface. A successful contacting was only possible at negative sample bias, what can be explained by the electrostatic force that pulls the molecule to the tip. A lifting of the molecule for up to 8 Å or  $\approx 30^\circ$  was achieved. Nevertheless, the binding strength is not sufficient to pull the molecules in a completely upright position, as it was achieved for other systems by [123, 124, 125]. It may be a worthy endeavor to perform comparison experiments on different substrate materials to overcome this problem.

We were able to perform tunneling spectroscopy on the DPBP bridges that show that the LUMO shifts about 1.0 eV upwards on lifting of the molecule. The proposed reason is



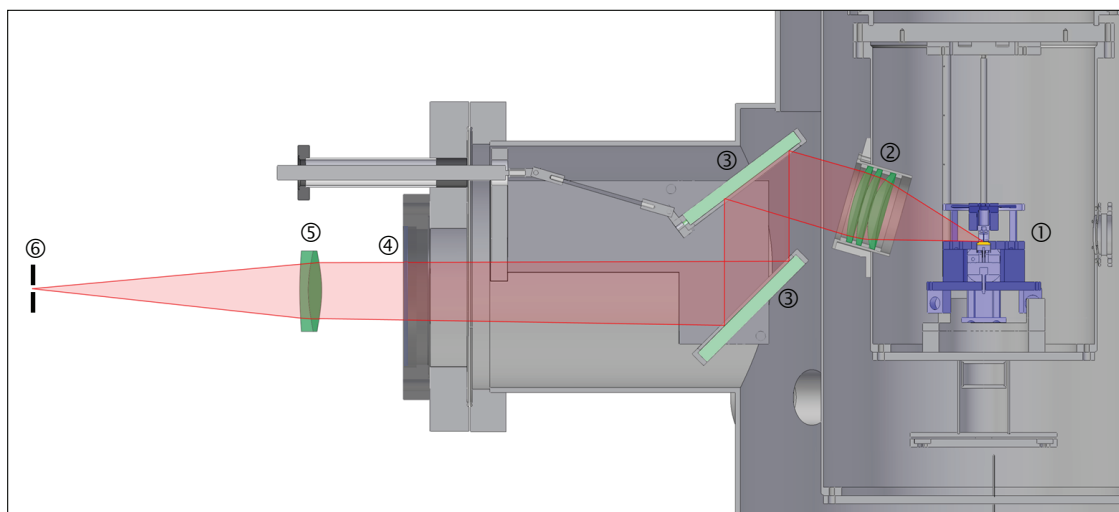


Figure 5.14: Cross-sectional drawing of the optical system that was designed and build into out LT-STM for further investigation of photo emission from DPBP molecules or comparable systems. Emitted photons leave the STM (blue) ①, are bundled by a first lens system ② and guided by mirrors ③ through a window ④ out of the vacuum chamber. A second lens ⑤ refocuses the beam so it can enter the spectrometer slit ⑥.

the more symmetric character of the metal-molecule-metal junction. It was found that the junction immediately breaks if electrons start to tunnel through the LUMO resonance, independently of the resonance's position. Enhanced vibrational excitation of the molecular junction induced by inelastically tunneling electrons is the reason for this effect. This proves a considerable coupling between molecular vibrations and the transition between neutral and anionic state.

We therefore plan to proceed with this molecular species as a first candidate in our aim to study optical transitions that involve and resolve vibrationally excited states. Photons emitted from multi-step processes that involve the transition between different electronic and vibrational levels can give information about inelastic electron transport channels that are not accessible otherwise. In order to detect this photon emission from the junction it is necessary to get a sufficient amount of the light from the STM into an optical spectrometer. For this purpose, we developed and built an optical system that allows for collimating the emitted photons, guiding them out of the vacuum chamber and refocusing them into a grid spectrometer (figure 5.14). A liquid nitrogen cooled CCD detector will be used as analyzer, allowing for fast recording of the emitted spectrum.



## Chapter 6

### Summary

In this thesis, we presented three different experiments that investigate fundamental aspects of the behavior of single molecules in the proximity of metal surfaces and electrodes.

In our first experiment, we investigate the character of different heating and cooling mechanisms governing the temperature reached by a single  $C_{60}$  molecule inside an STM junction during electronic transport. The molecule is heated by inelastic scattering of the tunneling electrons with vibrational modes. The strength of this heating process depends on the current and can be adjusted by variation of the tip-molecule distance  $z$ . If the current is increased to the order of microamperes by approaching of the tip, the  $C_{60}$  molecule undergoes an irreversible temperature-induced rupture of the fullerene cage. This can be identified in STM images and STS curves.

In our study, we have analyzed various aspects of the decomposition process with the help of an elemental description of the excitation of vibrational modes. Therein, the decomposition of the molecular structure takes place when a number of vibrational modes is excited. This accumulation of vibrational energy exhibits a high statistical character that leads to an unexpected behavior of the system: the faster the tip is approached to induce the molecular decomposition, the higher is the tunneling current at the point of degradation. The easy model is presented that explains this effect in terms of probabilities.

The temperature inside a  $C_{60}$  molecule is determined by the interplay between heating and cooling mechanisms. Our results provide evidence of two major molecular cooling mechanisms: vibron assisted tunneling, i.e. the transfer of vibrational energy of the molecule into tunneling electrons, and the excitation of electron-hole ( $e-h$ ) pairs in the close-by metal. Both mechanisms are found to be active in our setup. The first one is connected to modulations of the electrical power that is required to decompose the  $C_{60}$  molecules with the applied bias voltage, which reflect the molecular resonance structure of the fullerene. Electrons tunneling at an energy just below a molecular resonance may

cool the fullerene by “trapping” of a vibron. A similar effect causes electrons with energies slightly above a resonance to heat the system most efficiently by vibron emission.

The influence of the second mechanism, i.e. vibrational deexcitation through creation of  $e-h$  pairs in the contacts, becomes apparent when comparing the required decomposition powers on three different metals, copper, lead and gold. The most stable molecules are found on copper, where a power of about 20  $\mu\text{W}$  is needed to trigger a decomposition. On gold,  $\text{C}_{60}$  molecules show the lowest stability with decomposition powers of only  $\sim 1 \mu\text{W}$ . The reasons for these considerable differences is a different alignment of the molecular resonances with respect to the Fermi levels for the three substrates. We propose that on copper, where the LUMO is aligned at the Fermi level, the  $e-h$  pair creation process is enhanced due to a strong coupling of the semi-filled orbital to the electron states of the metal that are accessible for  $e-h$  excitation. When the LUMO energy is gradually shifted away from  $E_F$ , as it is the case on lead and gold, the efficiency for  $e-h$  pair creation decreases and with it the cooling performance of this mechanism. This leads to thermally less stable molecules. The power dissipated through this cooling channel was found to be fairly independent of the tunnelling electron energy, what causes the total power for decomposition to be approximately constant in the tunneling regime. This decomposition power value is thus a characteristic of the nature of the metal substrate. The considerable influence of this channel becomes apparent also when the STM tip is brought into contact with the molecule. Then, an additional contribution to the cooling is established by the possibility to create  $e-h$  pairs in the tip, what drastically enhances the thermal stability of the molecules.

In chapter 4 we have investigated the ring-opening isomerization behavior of the photo-switching 1,3,3-Trimethylindolino-6-nitrobenzopyrylospiran (spiropyran, SP) molecules when adsorbed to metal surfaces. SP molecules can react to their isomeric form merocyanine (MC) by a ring-opening reaction, that is induced by heating or light illumination. For molecules in gas phase or in solution, this isomerization process is bidirectional. In our experiments, we study how the adsorption of the molecules to a metal surface affects this switching behavior.

If SP molecules are deposited on a Au(111) or a Bi(110) surface at temperatures between 200 K and 270 K, they form ordered self-assembled islands. On annealing to temperatures above 300 K, a thermally induced ring-opening reaction takes place. The potential barrier height for this reaction is similar to the one of a free molecule, as deduced with the help of HREELS measurement performed by the group of Dr. P. Tegeder. The resulting MC molecules form 1-dimensional chain-like structures on gold and 2-dimensional islands on bismuth. We believe that on gold repulsive forces between the molecules stemming from the zwitterionic character of the merocyanines lead to electrostatic repulsions and promote the condensation in a 1-dimensional phase. The lower density of electronic states (DOS) of the bismuth substrate prevents the formation of zwitterions, what reduces the repulsion and enables condensation in a more compact phase.

On gold, no back-transformation of the MC molecules into the initial SP species could be achieved by temperature, electrons or light. Merocyanines turned out to be the most stable form of the two isomers. This is in contrast to free molecules, where SP is known to be the most stable isomer. The reason for this stability inversion on the metal surfaces is the strong adsorption of the planar MC molecules, as was deduced with the help of NEXAFS measurements done by the group of Prof. W. Kuch. The MC  $\rightarrow$  SP photo-isomerization is probably also hindered by this stabilization process.

The photoswitching behavior of the molecules was tested by illumination and shows a clear dependence on the substrate material. On gold, no photoswitching effects could be observed in either direction. On bismuth, several mixed MC/SP phases appear on light illumination. Here, the switching is supposed to be bidirectional and leads to the formation of an equilibrium phase between the two species. Nevertheless, the switching yield per photon was found to be eight orders of magnitude smaller than for free molecules. The reason is a considerable reduction of the photo-excited state's lifetimes on metal surfaces, where excitations can quickly deexcite into the substrate. The probability for ring-opening reactions then decreases with the lifetime.

On the other hand, an increase of the switching probability was observed, if the bismuth sample was kept at higher temperatures during illumination (300 K instead of 200 K). In this case, higher vibrational states of the molecule are populated, which serve as initial states of the photo-induced ring-opening reaction and increase the success rate of this process.

The attachment of tunneling electrons into the LUMO resonance of the spiropyran molecules was identified as a third way to induce SP  $\rightarrow$  MC isomerizations. These processes were observed on both metals and are believed to base on a similar mechanism as the photo-switching.

The last experimental study of this work deals with the investigation of single molecular wires fixed between two metal electrodes. Such junctions can be formed by contacting and lifting of single poly-phenyl molecules with the STM tip. The aim of this experiment is to study the transport behavior through the molecules and, at a later point, the optical deexcitation mechanisms of such junction.

The molecules under investigation were functionalized with amino and pyridil end groups to form reliable bonds between the tip and the molecule. To achieve a strong bonding to the end group's terminating nitrogen atoms, copper was used as tip and substrate material. Deposited on Cu(100), the amino-equipped di-amino-tri-phenyl (DATP) molecules form chains with a chiral staircase-like structure. The bond between two adjoining molecules is hereby proposed to be mediated by a copper adatom. It turned out that the formation of a contact between tip and molecule is difficult. We believe the reason to be the special  $sp^3$  bond geometry of the amino end group's nitrogen atom. Its lone pair orbital, that

is involved in bonds to copper atoms, is directed towards the substrate. This orientation hinders the bond formation with the tip that approaches from the opposite direction.

Pyridil-terminated di-pyridyl-bi-phenyl (DPBP) molecules form linear chains on a Cu(111) surface. Like in the case of DATP, the molecular interconnection is believed to be mediated by copper adatoms. We found that contacts between tip and molecules can very reliably be formed. The molecules can be pulled up to 8 Å by the tip, before the tip-molecule contact breaks. *I-z* curves recorded during the tip retraction state that a new tunneling pathway for the electrons is provided by the molecule while they are fixed between the contacts.

STS curves can be measured in a lifted-DPBP-molecule situation and show a considerable shift of the LUMO energy position to roughly double its value with respect to the flat lying alignment. We attribute this to the fact, that the tip-molecule-surface junctions approaches a double tunnelling barrier configuration. It was further found that the breaking of the tip-molecule bond can be induced by attachment of tunneling electrons to the LUMO.

Our plans for the future are to investigate the electron induced photon emission of such tip-molecule-surface junctions. Therefore an optical setup will be used that allows for collection and spectral analysis of photons that are emitted from the tunnel junction during such transport experiments. The emitting processes are expected to be multi-step transitions between different electronic and vibrational levels of the molecule. We believe that the DPBP molecules are good candidates for such experiments since they are known to have a strong coupling between electronic state transitions and internal vibrational modes of the molecules.



## Appendix A

## Appendix A

### Details of Data Analysis

#### A.1 Assignment of Peak Onsets in Incomplete Spectra

The problem is to assign comparable positions of the LUMO peak onsets of the  $dI_t/dV_s$  spectra presented in chapter 5.2. A simple approach would be, to fit a Gaussian curve and to define the onset position as the point where a fixed ratio, say 1/10, of the maximum peak height is reached. This method will inevitably run into problems, since the top part of the actual resonance peak is situated outside the spectrum's range and only a shoulder is visible in the spectrum. As a result, the obtained values for amplitude, center and width of the Gaussian peak would be somehow arbitrary.

To circumvent this problem, we used the following procedure: fitting of a Gauss curve on an exponentially increasing background to the normalized spectrum, plotting the second derivative of the logarithm of this fit and defining the first maximum as the resulting onset position. By this procedure the onset can be defined accurately as it is shown for the case of a tunneling spectrum in figure A.1 a).

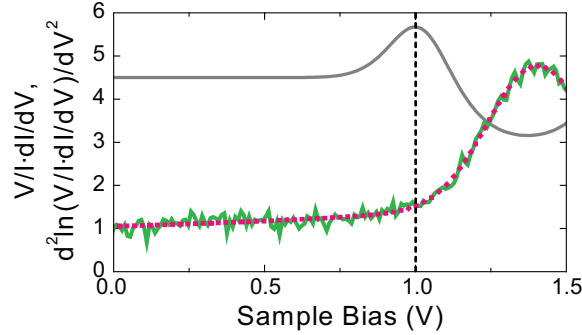


Figure A.1: Illustration of the method for defining the onset of the LUMO peak using the example of an STS curve of the DPBP molecule: the logarithm of the fitting function (dashed red line) to the normalized  $dI/dV_S$  curve (green line) is derived two times (gray line). The first maximum of the resulting curve defines the onset position (dashed black line).

## A.2 Determination of Photo Quantum Yield

The spot profile of the 45 mW laser diode used in the illumination experiments in 4.4.4 can be approximated by a oval spot with Gaussian profile. The spot's width and height are about  $7.0 \text{ mm} \times 3.2 \text{ mm}$ . Therefore an intensity distribution

$$I(x,y) = I_0 \cdot \exp \left[ -0.5 \left( \frac{x}{\omega_x} \right)^2 \right] \exp \left[ -0.5 \left( \frac{y}{\omega_y} \right)^2 \right]$$

with  $\omega_x = 0.35/\sqrt{2} \text{ cm}^{-1}$ ,  $\omega_y = 0.16/\sqrt{2} \text{ cm}^{-1}$  and  $I_0 = 256.0 \text{ mW/cm}^2$  was taken as reference for the estimation of the photo yield value (see figure A.2).

To determinate the photo quantum yield that was presented in section 4.4.4, we analyzed five positions on the sample that were illuminated for a time  $T_0 = 240 \text{ min}$  with this laser spot during the experiment. It was necessary to estimate the approximate light intensity and the resulting MC:SP ratio on each of these points. The first was done with the help of the spot profile approximation described above. During the experiments we recorded the position and orientation of the illumination spot with respect to the sample and the different scanning positions. The assignment of an intensity  $I_i$  on the point  $i$  is thus possible. For the second task, a number of STM images was analyzed by measuring the island size of the different phases. This allows a rough estimation of the amount of MC and SP

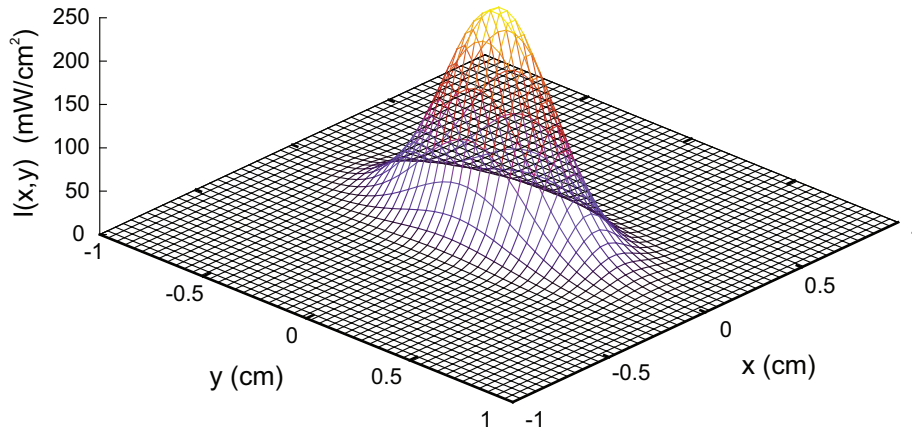


Figure A.2: Approximated intensity distribution  $I(x,y)$  of the used 45 mW laser diode.

molecules. The relative number of merocyanine molecules over the illumination fluence  $F = I \cdot T_0$  can then be fitted by the expression

$$\frac{N_{MC}(F)}{N_{MC}(F) + N_{SP}(F)} = \frac{1}{1 + \frac{P_{ms}}{P_{sm}}} [1 - \exp \{ - (P_{ms} + P_{sm}) \cdot F \}] \quad (\text{A.1})$$

where  $N_{SP}$  and  $N_{MC}$  denote the number of SP and MC molecules and  $P_{ms}$  and  $P_{sm}$  are probability factors for the MC→SP and SP→MC switching respectively. It is assumed in this formula that the probability for switching of one molecule per second is  $P_{xx} \cdot I$  and thus linear to the incoming photon intensity. This is valid for small probability values as it is the case here.

It should be noted that the resulting values of the statistical analysis depend to a considerable degree on the composition assignment of the different phases. This was chosen as described in section 4.4.4.

The result of the fitting is shown in figure A.3. We obtain the probability values  $P_{ms} = 6.3 \cdot 10^{-7} \pm 4.5 \cdot 10^{-7} \text{ (mJ / cm}^2\text{)}^{-1}$  and  $P_{sm} = 9.9 \cdot 10^{-7} \pm 4.5 \cdot 10^{-7} \text{ (mJ / cm}^2\text{)}^{-1}$ .

The total cross sections of the reactions with the 445 nm photons can be derived from these values<sup>1</sup> and yields  $\sigma_{ms} = 2.8 \cdot 10^{-22} \pm 2.0 \cdot 10^{-22} \text{ cm}^2$  and  $\sigma_{sm} = 4.4 \cdot 10^{-22} \pm 2.0 \cdot 10^{-22} \text{ cm}^2$ .

---

<sup>1</sup>  $\sigma_{xx} = P_{xx} \cdot h\nu$

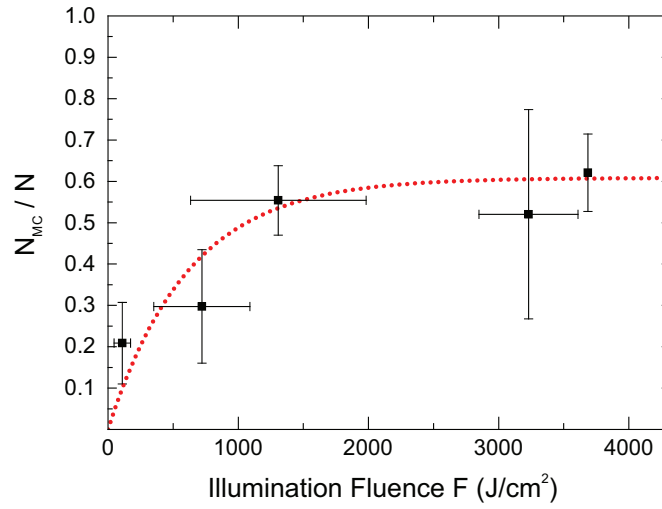


Figure A.3: Counted fraction of MC molecules vs illumination fluence plot (black squares) and error weighted fit of equation A.1 (dashed red line) to the data points. The fitting results are  $P_{ms} = 6.3 \cdot 10^{-7} \pm 4.5 \cdot 10^{-7} \text{ (mJ / cm}^2\text{)}^{-1}$  and  $P_{sm} = 9.9 \cdot 10^{-7} \pm 4.5 \cdot 10^{-7} \text{ (mJ / cm}^2\text{)}^{-1}$ . The errors are  $2 \times \text{SEM}$ .

The photo quantum yield can be derived by dividing the cross sections by the approximate area of one molecule<sup>2</sup> and gives  $\Phi_{ms} = 3.6 \cdot 10^{-8} \pm 2.6 \cdot 10^{-8}$  events per photon and  $\Phi_{sm} = 5.3 \cdot 10^{-8} \pm 2.4 \cdot 10^{-8}$  events per photon. It should be noted that the actual error of the numbers can be somewhat bigger. This is due to uncertainties that enter with the spot profile approximation and with the assignment of the composition of the different phases.

<sup>2</sup> $\Phi_{ab} = \sigma_{ab} / a_a$ , with the experimental areas of one SP molecule  $a_{SP} = 0.83 \text{ nm}^2$  and of one MC molecule  $a_{MC} = 0.80 \text{ nm}^2$ .

### A.3 Decomposition Dynamics Model

In section 3.2.2, the electronic multi excitation dynamics of critical vibrational modes, i.e. of modes that can induce molecular degradation of a  $C_{60}$  molecule, was presented. The statistical properties of the excitation process explain the experimentally observed dependence of the decomposition current  $I_{\text{dec}}$  on the tip approach speed  $\zeta$ . In this section we will explain the mathematical details of the proposed statistical model.

For illustrative reasons, we will start with an approximation of the molecular potential of the critical mode(s) as harmonic oscillator potential (figure A.4). We will apply the formal treatment of this potential that allows single electrons to create single steps of vibrational excitations only. Several electrons are thus needed to achieve multiple vibrational excitations (*multiple incoherent excitations*) [54]. Later, we expand the formalism also to the more general case of multi-vibrational excitation by a single electron (*multiple coherent excitation*).

Starting from the occupation of the  $n$ th vibrational level, the probability for a tunneling electron to create a vibrational excitation in level  $n+1$  by inelastic scattering shall be labeled as  $\Phi_n$ . The lifetime of the  $n$ th level is labeled as  $\tau_{\text{vib},n}$ . In the incoherent multiple excitation formalism, the dependence on the level number  $n$  can be expressed as  $\Phi_n = (n+1)\Phi$  and as  $\tau_{\text{vib},n} = \tau_{\text{vib}} / n$  [54].

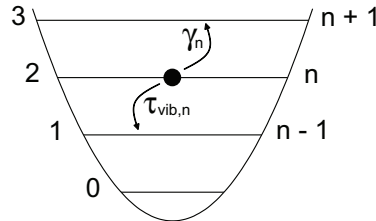


Figure A.4: Harmonic oscillator approximation with nomenclature as used in the text.

The basic idea of the model is to define the moment of decomposition by the moment the  $N$ th electron-induced vibrational excitation of the model molecule takes place. Therefore, we need to find an expression of the probability for general higher-level vibrational excitations to occur. This will be derived in a first step.

It is convenient to define two different time scales: the time parameter  $t_0$  that is defined in a *macroscopic* time scale of the experiment, i.e. in a range of several seconds. Slowly changing parameters as the tip-molecule distance or the tunnel current depend on  $t_0$ . Apart from that, a *microscopic* time scale is defined by the variable  $t$ .

The electron current that effectively induces excitations from the  $n$ th vibrational level to the  $(n+1)$ th one is given as  $I_{\text{eff},n}(t_0) = \Phi_n I(t_0)$  with  $I(t_0)$  being the tunneling current at

time  $t_0$  in A. Therefore, the mean time between two such excitations is  $\gamma_n(t_0) = \frac{q_{e^-}}{I_{\text{eff},n}(t_0)}$  ( $q_{e^-}$ : electron charge).

We now assume that a first vibrational excitation from the  $(n-1)$ th to the  $n$ th level ( $n > 0$ ) has initially occurred at a time  $t_0$ . The probability density for a randomly distributed event, like the excitation to the  $(n+1)$ th level is

$$p_{t_0}^{(n \rightarrow n+1)}(t) = \frac{1}{\gamma_n(t_0)} \cdot \exp\left(-\frac{t-t_0}{\gamma_n(t_0)}\right). \quad (\text{A.2})$$

The total probability that this excitation takes place within the lifetime  $\tau_{\text{vib},n}$  of the  $n$ th vibrational state can be derived by integration:

$$P_{t_0}^{(n \rightarrow n+1)} = \int_{t_0}^{t_0 + \tau_{\text{vib},n}} p_{t_0}(\tilde{t}) d\tilde{t} \quad (\text{A.3})$$

$$= 1 - \exp\left(-\frac{\tau_{\text{vib},n}}{\gamma_n(t_0)}\right). \quad (\text{A.4})$$

This expression is the basic building block of the model and is interpreted as probability of the excitation to the  $(n+1)$ th vibrational level. However, it should be noted that this treatment implies a first simplification of the physical system. The statistical character of the vibrational deexcitation process is neglected and every excitation is assumed to decay exactly after the mean lifetime  $\tau_{\text{vib},n}$ . The effect of this approximation is discussed in section A.3.1.

In a next step, we can re-express the exponential factor of equation A.4 as

$$\frac{\tau_{\text{vib},n}}{\gamma_n(t_0)} = \frac{\tau_{\text{vib},n} \cdot \Phi_n \cdot I(t_0)}{q_{e^-}} = \left(1 + \frac{1}{n}\right) \frac{\tau_{\text{vib}} \cdot \Phi \cdot I(t_0)}{q_{e^-}}. \quad (\text{A.5})$$

From this expression we can see two important properties of the system. The first feature is that the parameters  $\Phi$  and  $\tau_{\text{vib}}$  cannot be resolved separately since they enter the equation as a product. Consequently, we can define a new combined model parameter  $\tau_{\text{eff}} = \tau_{\text{vib}} \cdot \Phi$ , the *effective excitation lifetime*. This means that the system acts as if *every electron excites one vibrational level with a level lifetime  $\tau_{\text{eff}}$* .

The second discovery is that the maximum effect that is caused by the parameter  $n$  is a doubling of the exponent for small  $n$  by the factor  $(1 + \frac{1}{n})$ . At higher  $n$  this prefactor



gradually reduces to one. Thus, the simplification  $(1 + \frac{1}{n}) \approx 1$  can be applied. This means that the probability for an excitation to the next higher level is assumed to be independent on the actual level number  $n$ . Although this approximation causes a certain error in the resulting value of  $\tau_{\text{eff}}$ , it does not affect the general behavior of the model, as is discussed in section A.3.1.

With this last simplification we can generalize the picture of our model from the consideration of a harmonic oscillator potential to a more general potential well. This includes especially the possibility of multi-step vibrational excitations by single electrons<sup>3</sup> (*multi coherent excitations*). Therefore, the general probability for any single- or multi-vibrational excitation by one electron (after the initial excitation) in the time span  $\tau_{\text{vib}}$  is given as

$$P_{t_0}^{(1)} = 1 - \exp\left(-\frac{\tau_{\text{eff}} \cdot I(t_0)}{q_{\text{e}^-}}\right). \quad (\text{A.6})$$

We can now easily expand the consideration to a higher number of excitation events. For  $m$  more excitations after the initial one, this equation becomes a *Poisson distribution*, i.e. the probability of exactly  $m$  more excitations to occur in a time span  $\tau_{\text{vib}}$  is

$$P_{t_0}^{(m)} = \frac{1}{m!} \left(\frac{\tau_{\text{eff}} \cdot I(t_0)}{q_{\text{e}^-}}\right)^m \cdot \exp\left(-\frac{\tau_{\text{eff}} \cdot I(t_0)}{q_{\text{e}^-}}\right). \quad (\text{A.7})$$

Since the first occurrence of  $m = N - 1$  or more excitations triggers the decomposition process, it is necessary to derive the probability of *at least*  $m$  excitations occurring after the first one in the time window  $\tau_{\text{vib}}$ :

$$P_{t_0}^{(\geq m)} = \sum_{n=m}^{\infty} P_{t_0}^{(n)} \quad (\text{A.8})$$

$$= 1 - \exp\left(-\frac{\tau_{\text{eff}} \cdot I(t_0)}{q_{\text{e}^-}}\right) \cdot \sum_{n=0}^{m-1} \frac{1}{n!} \left(\frac{\tau_{\text{eff}} \cdot I(t_0)}{q_{\text{e}^-}}\right)^n. \quad (\text{A.9})$$

For  $m = N - 1$ , this expression represents the probability of the model molecule to decompose in one attempt, i.e. within a time span  $\tau_{\text{vib}}$ . We can now extend the model to the time interval of the complete experiment, where a large number of attempts are performed

<sup>3</sup>In fact, the model, as it is constructed and applied, does not differentiate between coherent and incoherent excitation mechanisms as they are described in [54].

one after the other. To do so, we introduce the attempt frequency  $f$  and discretize the experiment's continuous time  $t_0$  into intervals of the width  $f^{-1}$ , i.e.  $t_0 \rightarrow i \cdot f^{-1}$  with  $i \in \mathbb{N}$ . The respective magnitudes are relabeled as  $I_i := I(i \cdot f^{-1})$  and  $P_i^{(\geq m, f^{-1})} := P_{i \cdot f^{-1}}^{(\geq m)}$ . This second magnitude now describes the probability that  $m$  or more electrons appear within the  $i$ th interval.

One critical point is the choice of the right attempt frequency. Although an interval length  $f^{-1} = \tau_{\text{vib}}$  would be the appropriate choice, we cannot do this since  $\tau_{\text{vib}}$  is no basic parameter of the model. Instead we define  $f^{-1} = \tau_{\text{eff}}$ , what can be justified as explained in section A.3.1.

This allows us to finally write the probability that  $m$  or more excitations occur within the  $i$ th interval and *not before* as

$$L_i^{(\geq m, \tau_{\text{eff}})} = P_i^{(\geq m, \tau_{\text{eff}})} \cdot \prod_{j=0}^{i-1} \left(1 - P_j^{(\geq m, \tau_{\text{eff}})}\right) \quad (\text{A.10})$$

and the probability density for this occurrence

$$dL_i^{(\geq m, \tau_{\text{eff}})} = \frac{1}{\tau_{\text{eff}}} \cdot L_i^{(\geq m, \tau_{\text{eff}})}. \quad (\text{A.11})$$

Example curves of  $P^{(\geq m, \tau_{\text{eff}})}(t)$  and  $dL^{(\geq m, \tau_{\text{eff}})}(t)$  are displayed in figure A.5 a) and explained below. The decomposition current expectation value can now be calculated from this

$$\langle I_{\text{dec}} \rangle = \tau_{\text{eff}} \sum_{j=0}^{\infty} \left( dL_j^{(\geq m, \tau_{\text{eff}})} \cdot I_j \right). \quad (\text{A.12})$$

For finally evaluating this equation we need two more ingredients: a model of the time evolution of the tunneling current  $I(t)$  as the tip approaches and a second, macroscopic time discretization to calculate the results with fewer effort than summing over all microscopic time intervals. The first is achieved by fitting the idealized tunnel equation  $I(z_{\text{appr}}) = a \cdot \exp(\beta \cdot z_{\text{appr}})$  to experimental curves recorded under the same parameters as the decomposition events ( $C_{60}$  on Pb(111), feedback opened at  $I_t = 2.0$  nA and  $V_S = 0.5$  V). The resulting fit is shown together with the resulting parameters  $a$  and  $\beta$  in figure A.5 b). In combination with the approach speed  $\zeta = z_{\text{appr}}/t$ , good approximations of  $I(t)$  and  $\gamma(t)$  are obtained.

The second problem is faced by an additional time discretization  $\Delta t$  in the order of microseconds to milliseconds, what allows the calculation of  $dL_i^{(\geq m, \tau_{\text{eff}})}$  and  $\langle I_{\text{dec}} \rangle$  on a standard office PC.

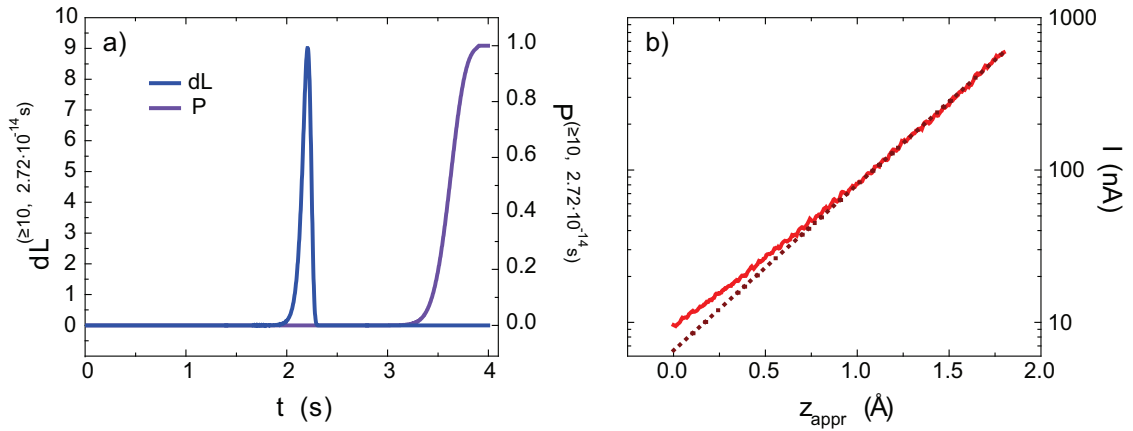


Figure A.5: a) The statistical values  $P^{\geq m, \tau_{\text{eff}}}(t)$  (violet) and  $dL^{\geq m, \tau_{\text{eff}}}(t)$  (blue) that describe the probability to find  $m$  or more electrons in a time interval  $\tau_{\text{eff}}$  and to find  $m$  or more electrons *the first time* in  $\tau_{\text{eff}}$ , calculated for  $m = 10$ ,  $\tau_{\text{eff}} = 2.72 \cdot 10^{-14}$  s and  $\zeta = 1.0$  Å/s. b) Average of 14 tunneling current approach curves  $I(z_{\text{appr}})$  and fit to it. The resulting parameters are  $a = 6.536 \cdot 10^{-9}$  A and  $\beta = 2.508$  Å<sup>-1</sup>. The deviation from the fit in the regime of low  $z_{\text{appr}}$  is due to nonlinear effects of the current preamplifier.

Curves of  $P^{\geq m, \tau_{\text{eff}}}(t)$  and  $dL^{\geq m, \tau_{\text{eff}}}(t)$  are displayed in figure A.5 a) for an exemplary model experiment. The  $dL$  curve represents the probability density of the model for the occurrence of a decomposition event. This probability density initially increases, since the probability per attempt  $P^{\geq m, \tau_{\text{eff}}}$  increases with  $I$ . After reaching a maximum value,  $dL$  gets suppressed again: the possibility that the decomposition took place at an earlier moment and that the model molecule is already “consumed” leads to a decrease  $dL$ .

The implemented calculation of  $\langle I_{\text{dec}} \rangle$  was used to perform a weighted least-square fit of the parameters  $\tau_{\text{eff}}$  and  $m$  (and thus  $N$ ) to the experimental values of  $I_{\text{dec}}$  for different tip approach speeds  $\zeta$  (figure 3.10 a). The  $I_{\text{dec}}$  distribution shown in figure 3.10 b) can then be obtained by plotting of  $dL^{\geq m, \tau_{\text{eff}}}$  vs.  $I$ .

### A.3.1 Limitations of the Model

As described above, some simplifications were applied to the decomposition model that can affect the reliability of the parameter values as derived from a fitting to the experimental data. The first approximation is the fact that the statistical character of the vibrational deexcitation was neglected and replaced by a model of a deexcitation after the mean value  $\tau_{\text{vib}}$ . The second simplification was done by removing the factor  $(1 + \frac{1}{n})$  from expression A.5. To estimate the impact of these approximations, we calculated and compared prob-

ability curves for the realization of the proposed degradation condition  $P_i^{(\geq m)}(\tau_{\text{eff}})$  as a function of  $\tau_{\text{eff}}$  for the model (with simplification) and for a full theory (without simplifications). We find that especially in the regime of low probabilities (the decomposition is typically realized at  $P_i^{(\geq m)}$  values in the order of  $10^{-12}$  or below) the full theory curve can be approximated by the model curve, if an additional renormalization factor in the order of up to ten is applied to  $\tau_{\text{eff}}$ . We can thus state that the value of  $\tau_{\text{eff}}$  as derived from a fitting to the experimental data is certainly wrong in this order. Nevertheless, we believe that the total order of magnitude of  $\tau_{\text{eff}}$  is approximately conserved by the approximations.

Another uncertainty enters the model via the assignment of the attempt frequency  $f$ . As explained in the text,  $f$  should ideally be set to  $\tau_{\text{vib}}^{-1}$ , what cannot be done since  $\tau_{\text{vib}}$  is no direct model parameter. Instead, an attempt frequency  $\tau_{\text{eff}}^{-1}$  is used. To check whether this has an influence on the behavior of the model system, we compared calculated  $I_{\text{dec}}(\zeta)$  curves with an  $f$  of  $\tau_{\text{eff}}^{-1}$  to curves with attempt frequencies that were manually reduced by a factor of 100. It turned out that the second system behaves exactly identical, if their effective vibrational lifetimes  $\tau_{\text{eff}}$  are multiplied by a factor of 1.7 compared to the first curve. This renormalization would normally be performed by a fitting routine. Especially the slope of the curves, that depends mainly on the critical number of excitations  $N$  did not change. We conclude, that the misadjustment of the attempt frequency  $f^{-1}$  leads to a wrong value of  $\tau_{\text{eff}}$  as well, but the parameter  $N$  appears to be robust against this approximation.

Summing up, we find that the approximations that were applied to the model result in a high uncertainty of the value of parameter  $\tau_{\text{eff}}$ . In contrast to that, the parameter  $N_{\text{e-}}$  appeared to be fairly robust. However, more advanced models should try to circumvent these approximations.

## Appendix B

## Appendix B Numerical Methods

### B.1 Force Field Molecular Mechanics Calculations

The force field calculations used the force field parameter set mm2 (1991) [144, 145, 146], which provides sufficient parameters for the modeling of the two molecules while supporting adequate accuracy for simulating the intermolecular forces and distances of small hydrocarbons [147]. Minor amendments had to be added to the parameter sets of the indoline N atom and the single O atom, and were gained by either extrapolation of extant constants or by setting of default values [147].

Simulations were performed using the freeware TINKER [112], modified to confine the motion of certain atoms into a plane by applying a harmonic potential (force constant of 100 kcal/Å<sup>2</sup>) to the  $z$  coordinate. Confinement to the  $z=0$  plane was applied to the carbon atoms of the nitrobenzene moiety, for the SP molecule, and to all  $sp^2$  C atoms of the MC molecule. To simulate surface induced bending on the three-dimensional SP molecule, the carbon atoms of the di-methyl moiety were also constrained to the  $z=0$  plane.

In order to investigate the complex charge distribution in the zwitterionic MC isomer an alternative charging model for merocyanine was explored and tested against the standard mm2 charging treatment. Static charges amounting to  $+\frac{1}{2}e$  and  $-\frac{1}{2}e$  were placed in the indole N atom and in the single O atom, leading to an increase of the total molecular dipole moment from 3.9 Debye to 13.6 Debye. The resulting minimum energy structures using this alternative charging model could not be reconciled with the STM images, probably

because the free molecules dipole moment is quenched in the proximity of the surface.

The energetically most stable structure of molecular dimers was obtained by a simulated annealing algorithm that cools the system exponentially from 600 K down to 0 K in 600000 steps of 1.0 fs. An additional gradient minimization was used to ensure that the structure ends in a minimum energy configuration. For every molecular pairing this procedure was repeated ten times, thus allowing the extraction of a global minimum-energy configuration. To further simulate larger molecular structures, the most stable spiropyran dimer configuration was used to construct an assembly of six molecules following the structures obtained by STM (figure 4.4 b)) and minimized following a sequence of gradient minimization, simulated annealing (exponential cooling from 80 K to 0 K in 40000 steps) and a second subsequent gradient minimization. By this procedure, the system gets joggled into a minimum of the structure, whenever it exists.

## References

- [1] - S. Solomon, D. Qin, M. Manning, Z. Chen, M. Marquis, K. B. Averyt, M. Tignor and H. L. Miller (eds.),  
*Climate Change 2007: Fourth Assessment Report of the Intergovernmental Panel on Climate Change*, Report, (2007)  
Cambridge University Press, Cambridge, New York
- [2] - J. M. Epstein,  
*Modelling to contain pandemics*,  
Nature 460 (2009) 687
- [3] - V. Springel, S. D. M. White, A. Jenkins, C. S. Frenk, N. Yoshida, L. Gao, J. Navarro, R. Thacker, D. Croton, J. Helly, J. A. Peacock, S. Cole, P. Thomas, H. Couchman, A. Evrard, J. Colberg and F. Pearce,  
*Simulations of the formation, evolution and clustering of galaxies and quasars*,  
Nature 435 (2005) 629
- [4] - M. Y. Lanzerotti (ed.),  
*The Technical Impact of Moore's Law*,  
IEEE solid-state circuits society newsletter 20 (3) (2006)
- [5] - V. V. Zhirnov, R. K. Cavin, J. A. Hutchby and G. I. Bourianoff,  
*Limits to Binary Logic Switch Scaling—A Gedanken Model*,  
Proc. IEEE 91 (2003) 1934
- [6] - R. Feynman,  
*There's Plenty of Room at the Bottom*, Lecture, December 29, 1959  
California Institute of Technology
- [7] - A. Aviram and M. A. Ratner,  
*Molecular Rectifiers*,  
Chem. Phys. Lett. 29 (1974) 277



- [8] - A. S. Martin, J. R. Sambles and G. J. Ashwell  
*Molecular rectifier*,  
Phys. Rev. Lett. 70 (1993) 218
- [9] - L. A. Bumm, J. J. Arnold, M. T. Cygan, T. D. Dunbar, T. P. Burgin, L. Jones,  
D. L. Allara, J. M. Tour and P. S. Weiss,  
*Are single molecular wires conducting?*,  
Science 271 (1996) 1705
- [10] - S. J. Tans, A. R. M. Verschueren and C. Dekker,  
*Room-temperature transistor based on a single carbon nanotube*,  
Nature 393 (1998) 49
- [11] - X. Li, J. He, J. Hihath, B. Xu, S. M. Lindsay and N. Tao,  
*Conductance of Single Alkanedithiols: Conduction Mechanism  
and Effect of Molecule-Electrode Contacts*,  
J. Am. Chem. Soc. 128 (2006) 2135
- [12] - I. Horcas, R. Fernández, J. M. Gómez-Rodríguez and J. Colchero  
*WSXM: A software for scanning probe microscopy  
and a tool for nanotechnology*,  
Rev. Sci. Instrum. 78 (2007) 013705
- [13] - J. Tersoff and D. R. Hamann,  
*Theory and Application for the Scanning Tunneling Microscope*,  
Phys. Rev. Lett. 50 (1983) 1998
- [14] - N. D. Lang,  
*Spectroscopy of single atoms in the scanning tunneling microscope*,  
Phys. Rev. B: Condens. Matter 34 (1986) 5947
- [15] - J. Bardeen,  
*Tunneling from a many-particle point of view*,  
Phys. Rev. Lett. 6 (1961) 57
- [16] - A. Selloni, P. Carnevali, E. Tosatti and C. D. Chen  
*Voltage-dependent scanning-tunneling microscopy  
of a crystal surface: Graphite*,  
Phys. Rev. B: Condens. Matter 31 (1985) 2602
- [17] - G. Binnig, K. H. Frank, H. Fuchs, N. Garcia, B. Reihl, H. Rohrer,  
F. Salvan and A. R. Williams  
*Tunneling Spectroscopy and Inverse Photoemission: Image and Field States*,  
Phys. Rev. Lett. 55 (1985) 991

- [18] - R.M. Feenstra, J. A. Stroscio and A.P. Fein,  
*Tunneling spectroscopy of the Si(111)2 × 1 surface* ,  
Surf. Sci. 181 (1987) 295
- [19] - J.I. Pascual, J. Gómez-Herrero, C. Rogero, A.M. Baró, D. Sánchez-Portal,  
E. Artacho, P. Ordejón and J.M. Soler,  
*Seeing molecular orbitals*,  
Chem. Phys. Lett. 321 (2000) 78
- [20] - J. I. Pascual, J. Gómez-Herrero, D. Sánchez-Portal and H.-P. Rust,  
*Vibrational spectroscopy on single C<sub>60</sub> molecules:  
The role of molecular orientation*,  
J. Chem. Phys. 117 (2002) 9531
- [21] - X. Crispin, V. Geskin, A. Crispin, J. Cornil, R. Lazzaroni,  
W. R. Salaneck, and Jean-Luc Brédas,  
*Characterization of the Interface Dipole at Organic Metal Interfaces*,  
J. Am. Chem. Soc. 124 (2002) 8131
- [22] - W. Ho  
*Single-molecule chemistry*,  
J. Chem. Phys. 117 (2002) 11033
- [23] - J. I. Pascual  
*Single molecule vibrationally mediated chemistry*,  
Eur. Phys. J. D 35 (2005) 327
- [24] - K. J. Franke, G. Schulze and J. I. Pascual,  
*Excitation of Jahn-Teller active modes during electron  
transport through single C<sub>60</sub> molecules on metal surfaces  
between lead electrodes*,  
Submitted to Nano Lett.
- [25] - S. W. Wu, G. V. Nazin, X. Chen, X. H. Qiu and W. Ho  
*Control of Relative Tunneling Rates  
in Single Molecule Bipolar Electron Transport*,  
Phys. Rev. Lett. 93 (2004) 236802
- [26] - N. Liu, N. A. Pradhan and W. Ho  
*Vibronic states in single molecules:  
C<sub>60</sub> and C<sub>70</sub> on ultrathin Al<sub>2</sub>O<sub>3</sub> films*,  
J. Chem. Phys. 120 (2004) 11371
- [27] - T. Frederiksen, K. J. Franke, A. Arnau, G. Schulze, J. I. Pascual and N. Lorente  
*Dynamic Jahn-Teller effect in electronic transport through single C<sub>60</sub> molecules*,  
Phys. Rev. B: Condens. Matter 78 (2008) 233401

- [28] - H. Ibach  
*Physics of Surfaces and Interfaces*, 1st Edition, (2006)  
Springer Verlag Berlin, Heidelberg, New York
- [29] - R. E. Palmer and P. J. Rous  
*Resonances in electron scattering by molecules on surfaces*,  
Rev. Mod. Phys. 64 (1992) 383
- [30] - H. Haken and H. C. Wolf  
*Molekülphysik und Quantenchemie*, 5th Edition, (2006)  
Springer Verlag Berlin, Heidelberg, New York
- [31] - J. Stöhr  
*NEXAFS Spectroscopy*, 1st Edition, (1992)  
Springer Verlag Berlin, Heidelberg, New York
- [32] - F. Reinert, G. Nicolay, S. Schmidt, D. Ehm and S. Hüfner,  
*Direct measurements of the L-gap surface states on the (111)  
face of noble metals by photoelectron spectroscopy*,  
Phys. Rev. B: Condens. Matter 63 (2001) 115415
- [33] - S. Kevan  
*High-resolution angle-resolved photoemission study  
of the Cu(011) surface state*,  
Phys. Rev. B: Condens. Matter 28 (1983) 4822
- [34] - J. V. Barth, H. Brune, G. Ertl and R. J. Behm  
*Scanning tunneling microscopy observations on the reconstructed Au(111)  
surface: Atomic structure, long-range superstructure, rotational domains,  
and surface defects*,  
Phys. Rev. B: Condens. Matter 42 (1990) 9307
- [35] - S. Agergaard, Ch. Søndergaard, H. Li, M. B. Nielsen, S. V. Hoffmann,  
Z. Li and Ph. Hofmann  
*The effect of reduced dimensionality on a semimetal:  
the electronic structure of the Bi(110) surface*,  
New J. Phys. 3 (2001) 15.1
- [36] - Ph. Hofmann,  
*The surfaces of bismuth: Structural and electronic properties*,  
Prog. Surf. Sci. 81 (2006) 191
- [37] - M. Galperin, M. A. Ratner and A. Nitzan,  
*Molecular transport junctions: vibrational effects*,  
J. Phys. Condens. Matter 19 (2007) 103201

- [38] - Z. Huang, B. Xu, Y. Chen, M. Di Ventra and N. Tao  
*Measurement of Current-Induced Local Heating in a Single Molecule Junction*,  
Nano Lett. 6 (2006) 1240
- [39] - Z. Huang, F. Chen, R. D'Agosta, P. A. Bennett, M. Di Ventra and N. Tao  
*Local ionic and electron heating in single-molecule*,  
Nat. Nanotechnol. 2 (2007) 698
- [40] - N. Néel, J. Kröger, L. Limot, T. Frederiksen, M. Brandbyge and R. Berndt  
*Controlled Contact to a C<sub>60</sub> Molecule*,  
Phys. Rev. Lett. 98 (2007) 065502
- [41] - R. Landauer,  
*Spatial variation of currents and fields due to  
localized scatterers in metallic conduction*,  
IBM J. Res. Dev. 1 (1957) 223
- [42] - H. Michaelson  
*The work function of the elements and its periodicity*,  
J. Appl. Phys. 48 (1977) 4729
- [43] - V. S. Fomenko and I. A. Podchernyaeva  
*Emission and Adsorption Properties  
of Substances and Materials: A Handbook*, (1975)  
Atomizdat, Moscow
- [44] - G. Schulze, K. J. Franke, A. Gagliardi, G. Romano, C. S. Lin, A. L. Rosa,  
T. A. Niehaus, Th. Frauenheim, A. Di Carlo, A. Pecchia and J. I. Pascual  
*Resonant Electron Heating and Molecular Phonon Cooling  
in Single C<sub>60</sub> Junctions*,  
Phys. Rev. Lett. 100 (2008) 136801
- [45] - R. Fasel, R. G. Agostino, P. Aebi and L. Schlapbach  
*Unusual molecular orientation  
and frozen librational motion of C<sub>60</sub> on Cu(110)*,  
Phys. Rev. B: Condens. Matter 60 (1999) 4517
- [46] - G. Schull and R. Berndt,  
*Orientationally Ordered (7 × 7) Superstructure of C<sub>60</sub> on Au(111)*,  
Phys. Rev. Lett. 99 (2007) 226105
- [47] - C. Rogero, J. I. Pascual, J. Gómez-Herrero and A. M. Baró,  
*Resolution of site-specific bonding properties of C<sub>60</sub> adsorbed on Au(111)*,  
J. Chem. Phys. 116 (2002) 832

- [48] - N. Néel, L. Limot, J. Kröger and R. Berndt,  
*Rotation of  $C_{60}$  in a single-molecule contact*,  
Phys. Rev. B: Condens. Matter 77 (2008) 125431
- [49] - X. Lu, M. Grobis, K. H. Khoo, S. G. Louie, and M. F. Crommie,  
*Charge transfer and screening in individual  $C_{60}$  molecules on metal substrates: A scanning tunneling spectroscopy and theoretical study*,  
Phys. Rev. B: Condens. Matter 70 (2004) 115418
- [50] - Y. B. Zhao, D. M. Poirier, R. J. Pechman and J. H. Weaver,  
*Electron stimulated polymerization of solid  $C_{60}$* ,  
Appl. Phys. Lett. 64 (1994) 577
- [51] - M. R. Stetzer, P. A. Heiney, J. E. Fischer and A. R. McGhie  
*Thermal stability of solid  $C_{60}$* ,  
Phys. Rev. B: Condens. Matter 55 (1997) 127
- [52] - V. Saltas, C. A. Papageorgopoulos  
*Adsorption and decomposition of  $C_{60}$  on Ni(110) surfaces*,  
Surf. Sci. 488 (2001) 23
- [53] - A. Sellidj, B. E. Koel  
*Vibrational and electronic properties of monolayer and multilayer fullerene  $C_{60}$  films on rhodium (111)*,  
J. Phys. Chem. 97 (1993) 10076
- [54] - G. P. Salam, M. Persson and R. E. Palmer  
*Possibility of coherent multiple excitation in atom transfer with a scanning tunneling microscope*,  
Phys. Rev. B: Condens. Matter 49 (1994) 10655
- [55] - A. Pecchia, G. Romano and A. Di Carlo,  
*Theory of heat dissipation in molecular electronics*,  
Phys. Rev. B: Condens. Matter 75 (2007) 035401
- [56] - G. Romano, A. Pecchia and A. Di Carlo,  
*Coupling of molecular vibrons with contact phonon reservoirs*,  
J. Phys. Condens. Matter 19 (2007) 215207
- [57] - S. G. Tikhodeev and H. Ueba,  
*Theory of inelastic tunneling and its relation to vibrational excitation in ladder climbing processes of single adsorbates*,  
Surf. Sci. 587 (2005) 25
- [58] - A. Gagliardi, C. S. Lin, A. L. Rosa, T. A. Niehaus, Th. Frauenheim  
Bremen Center for Computational Materials Science, Universität Bremen

- [59] - G. Romano, A. Di Carlo, A. Pecchia  
Università di Roma "Tor Vergata"
- [60] - R. M. Nicklow, G. Gilat, H. G. Smith, L. J. Raubenheimer  
and M. K. Wilkinson  
*Phonon Frequencies in Copper at 49 and 298° K*,  
Phys. Rev. 164 (1967) 922
- [61] - V. Schettino, M. Pagliai, L. Ciabini and G. Cardini  
*The Vibrational Spectrum of Fullerene C<sub>60</sub>*,  
J. Phys. Chem. A 105 (2001) 11192
- [62] - S. Gao, M. Persson and B.I. Lundqvist  
*Atomic switch proves importance of electron-hole pair mechanism in  
processes on metal surfaces*,  
Solid State Commun. 84 (1992) 271
- [63] - A. Pecchia, private communication
- [64] - P. Aebi, J. Osterwalder, R. Fasel, D. Naumovic and L. Schlapbach  
*Fermi surface mapping with photoelectrons at UV energies*,  
Surf. Sci. 307-309 (1994) 917
- [65] - S. LaShell, B. A. McDougall and E. Jensen  
*Spin Splitting of an Au(111) Surface State Band Observed  
with Angle Resolved Photoelectron Spectroscopy*,  
Phys. Rev. Lett. 77 (1996) 3419
- [66] - D. A. Papaconstantopoulos  
*Handbook of the Band Structure of Elemental Solids*, 1st Edition, (1986)  
Plenum Press, New York
- [67] - B. N. J. Persson and M. Persson  
*Vibrational Lifetime for CO Adsorbed on Cu(100)*,  
Solid State Commun. 36 (1980) 175
- [68] - C. Tindall, O. Takaoka, T. Kobayashi, Y. Hasegawa and T. Sakurai  
*Charge transfer of C<sub>60</sub> on copper surfaces*,  
Science Reports of the Research Institutes Tohoku University  
Series A – Physics, Chemistry and Metallurgy 44 (1997) 51
- [69] - N. Henningsen, K. J. Franke, I. Fernández-Torrente, G. Schulze, B. Priewisch,  
K. Rück-Braun, J. Dokić, T. Klamroth, P. Saalfrank and I. J. Pascual  
*Inducing the Rotation of a Single Phenyl Ring with Tunneling Electrons*,  
J. Phys. Chem. C 111 (2007) 14843

- [70] - X.-L. Zhou, X.-Y. Zhu and J.M. White  
*Photochemistry at adsorbate / metal interfaces*,  
Surf. Sci. Rep. 13 (1991) 73
- [71] - C.-Q. Wu, J.-X. Li and D.-H. Lee,  
*Switching and Nonswitching Phases of Photomechanical Molecules in Dissipative Environments*,  
Phys. Rev. Lett. 99 (2007) 038302
- [72] - K. Ichimura, S.-K. Oh and M. Nakagawa,  
*Light-Driven Motion of Liquids on a Photoresponsive Surface*,  
Science 288 (2000) 1624
- [73] - C.-S. Tsai, J.-K. Wang, R. T. Skodje and J.-C. Lin,  
*A Single Molecule View of Bistilbene Photoisomerization on a Surface Using Scanning Tunneling Microscopy*,  
J. Am. Chem. Soc. 127 (2005) 10788
- [74] - M. J. Comstock, N. Levy, A. Kirakosian, J. Cho, F. Lauterwasser, J. H. Harvey, D. A. Strubbe, J. M. J. Fréchet, D. Trauner, S. G. Louie and M. F. Crommie,  
*Reversible Photomechanical Switching of Individual Engineered Molecules at a Metallic Surface*,  
Phys. Rev. Lett. 99 (2007) 038301
- [75] - N. Levy, M. J. Comstock, J. Cho, L. Berbil-Bautista, A. Kirakosian, F. Lauterwasser, D. A. Poulsen, J. M. J. Fréchet and M. F. Crommie,  
*Self-Patterned Molecular Photoswitching in Nanoscale Surface Assemblies*,  
Nano Lett. 9 (2009) 935
- [76] - M. Alemani, M. V. Peters, S. Hecht, K.-H. Rieder, F. Moresco and L. Grill,  
*Electric Field-Induced Isomerization of Azobenzene by STM*,  
J. Am. Chem. Soc. 128 (2006) 14446
- [77] - N. Henningsen, R. Rurali, K. J. Franke, I. Fernández-Torrente and I. J. Pascual  
*Trans to cis isomerization of an azobenzene derivative on a Cu(100) surface*,  
App. Phys. A 93 (2008) 241
- [78] - J. Henzl, M. Mehlhorn, H. Gawronski, K.-H. Rieder and K. Morgenstern,  
*Reversible cis-trans Isomerization of a Single Azobenzene Molecule*,  
Angew. Chem. Int. Ed. 45 (2006) 603
- [79] - B.-Y. Choi, S.-J. Kahng, S. Kim, H. Kim, H. W. Kim, Y. J. Song, J. Ihm and Y. Kuk,  
*Conformational Molecular Switch of the Azobenzene Molecule: A Scanning Tunneling Microscopy Study*,  
Phys. Rev. Lett. 96 (2006) 156106



- [80] - A. A. Garci, S. Cherian, J. Park, D. Gust, F. Jahnke and R. Rosario,  
*Photon-Controlled Phase Partitioning of Spiropyrans*,  
J. Phys. Chem. A 104 (2000) 6103
- [81] - R. Byrne and D. Diamond,  
*Chemo/bio-sensor networks*,  
Nature Mater. 5 (2006) 421
- [82] - G. Berkovic, V. Krongauz and V. Weiss,  
*Spiropyrans and Spirooxazines for Memories and Switches*,  
Chem. Rev. 100 (2000) 1741
- [83] - F.M. Raymo and S. Giordani,  
*Supramolecular Chemistry And Self-assembly Special Feature:  
All-optical processing with molecular switches*,  
Proc. Natl. Acad. Sci. 99 (2002) 4941
- [84] - A. Radu, S. Scarmagnani, R. Byrne, C. Slater, K. Tong Lau  
and D. Diamond,  
*Photonic modulation of surface properties:  
a novel concept in chemical sensing*,  
J. Phys. D: Appl. Phys. 40 (2007) 7238
- [85] - P. N. Day, Z. Wang and R. Pachter,  
*Ab Initio Study of the Ring-Opening Reactions of Pyran,  
Nitrochromene, and Spiropyran*,  
J. Phys. Chem. 99 (1995) 9730
- [86] - G. Cottone, R. Noto and G. La Manna,  
*Theoretical study of spiropyran-merocyanine thermal isomerization*,  
Chem. Phys. Lett. 388 (2004) 218
- [87] - A. K. Chibisov and H. Görner,  
*Singlet versus triplet photoprocesses in indodicarbocyanine dyes and  
spiropyran-derived merocyanines*,  
J. Photochem. Photobiol., A 105 (1997) 261
- [88] - J. B. Flannery, Jr.,  
*The Photo- and Thermochemical Transients from Substituted  
1', 3', 3'-Trimethylindolinobenzospiropyrans*,  
J. Am. Chem. Soc. 90 (1968) 5660
- [89] - T. Bercovici, R. Heiligman-Rim and E. Fischer,  
*Photochromism in spiropyran. Part VI.  
Trimethylindolino-benzospiropyran and its derivatives*,  
Mol. Photochem. 1 (1969) 23

- [90] - H. Görner,  
*Photochromism of nitrospiropyrans: effects of structure, solvent and temperature*,  
Phys. Chem. Chem. Phys. 3 (2001) 416
- [91] - S. Hagen, P. Kate, M.V. Peters, S. Hecht, M. Wolf and P. Tegeder,  
*Kinetic analysis of the photochemically and thermally induced isomerization of an azobenzene derivative on Au(111) probed by two-photon photoemission*,  
Appl. Phys. A 93 (2008) 253
- [92] - M. Wolf and P. Tegeder,  
*Reversible molecular switching at a metal surface: A case study of tetra-tert-butyl-azobenzene on Au(111)*,  
Surf. Sci. 603 (2009) 1506
- [93] - J. Henzl, T. Bredow and K. Morgenstern,  
*Irreversible isomerization of the azobenzene derivate Methyl Orange on Au(111)*,  
Chem. Phys. Lett. 435 (2007) 278
- [94] - M. Piantek, J. Miguel, M. Bernien, C. Navío, A. Kruger, B. Priewisch, K. Rück-Braun and W. Kuch,  
*Adsorption of carboxymethylester-azobenzene on copper and gold single crystal surfaces*,  
Appl. Phys. A 93 (2008) 261
- [95] - T. Huang, Z. Hu, A. Zhao, H. Wang, B. Wang, J. Yang and J. G. Huo,  
*Quasi Chiral Phase Separation in a Two-Dimensional Orientationally Disordered System: 6-Nitrospiropyran on Au(111)*,  
J. Am. Chem. Soc. 129 (2007) 3857
- [96] - T. Huang, Z. Hu, B. Wang, L. Chen, A. Zhao, H. Wang and J. G. Huo,  
*Observation of Hierarchical Chiral Structures in 8-Nitrospiropyran Monolayers*,  
J. Phys. Chem. B 111 (2007) 6973
- [97] - I. Fernández-Torrente, K. J. Franke, N. Henningsen, G. Schulze, M. Alemani, Ch. Roth, R. Ruruli, N. Lorente and J. I. Pascual,  
*Spontaneous formation of triptycene supramolecules on surfaces*,  
J. Phys. Chem. B 110 (2006) 20089
- [98] - A. E. Baber, S. C. Jensen, E. V. Iski and E. C. H. Sykes,  
*Dipole-Driven Ferroelectric Assembly of Styrene on Au{111}*,  
J. Am. Chem. Soc. 129 (2007) 6368

- [99] - T. Yokoyama, T. Takahashi, K. Shinozaki and M. Okamoto,  
*Quantitative Analysis of Long-Range Interactions between Adsorbed Dipolar Molecules on Cu(111)*,  
Phys. Rev. Lett. 98 (2007) 206102
- [100] - I. Fernández-Torrente, S. Monturet, K. J. Franke, J. Fraxedas,  
N. Lorente and J. I. Pascual,  
*Long-Range Repulsive Interaction between Molecules on a Metal Surface Induced by Charge Transfer*,  
Phys. Rev. Lett. 99 (2007) 176103
- [101] - Marten Piantek, Alex Krüger, Cristina Navío,  
Jorge Miguel, Matthias Bernien, Wolfgang Kuch  
Institut für Experimentalphysik, Freie Universität Berlin
- [102] - M. Delamar, J. Aubard, J.-L. Albert and J.-E. Dubois,  
*XPS study of a benzoazolinic spiropyran and a related permanent merocyanine*,  
J. Electron. Spectrosc. Relat. Phenom. 28 (1983) 289
- [103] - M. M. Chehimi and M. Delamar,  
*X-ray photoelectron spectroscopy of merocyanine dyes : VI. shake up satellites in the nitro N1s spectra of some nitromerocyanine dyes*,  
J. Electron Spectrosc. Relat. Phenom. 46 (1988) 427
- [104] - Matthias Koch, Felix Leyssner, Martin Wolf, Petra Tegeder  
Institut für Experimentalphysik, Freie Universität Berlin
- [105] - R. Delgado-Macuil, M. Rojas-López, V.L. Gayou,  
A. Orduña-Díaz and J. Díaz-Reyes,  
*ATR spectroscopy applied to photochromic polymer analysis*,  
Mater. Charact. 58 (2007) 771
- [106] - G. Cottone, R. Noto, G. La Manna and S. L. Fornili,  
*Ab initio study on the photoisomers of a nitro-substituted spiropyran*,  
Chem. Phys. Lett. 319 (2000) 51
- [107] - C. Schiele and G. Arnold,  
*Zur Struktur der photochromen Form des Spiro-6-Nitro-[2H-1-Benzopyran-2,2'-1',3',3'-Trimethylindolins]*,  
Tetrahedron Lett. 8 (1967) 1191
- [108] - A. Navarro, J. J. López González, A. G. Fernández, I. Laczik and G. Pongor,  
*Structural and vibrational study of isochroman*,  
Chem. Phys. 313 (2005) 279

- [109] - J.D. Laposa,  
*Vibrational spectra of nitrobenzene-d<sub>5</sub>*,  
Spectrochim. Acta, Part A 35 (1979) 65
- [110] - J. Clarkson and W. E. Smith,  
*A DFT analysis of the vibrational spectra of nitrobenzene*,  
J. Mol. Struct. 655 (2003) 413
- [111] - M. Piantek, G. Schulze, M. Koch, K. J. Franke, F. Leyssner, A. Krüger,  
C. Navío, J. Miguel, M. Bernien, M. Wolf, W. Kuch, P. Tegeder and J. I. Pascual  
*Reversing the Thermal Stability of a Molecular Switch on a Gold Surface:  
Ring-Opening Reaction of Nitrospiropyran*,  
J. Am. Chem. Soc. 131 (2009) 12729
- [112] - TINKER version 4.2 by Jay Ponder (2004),  
modified to allow for planar fixation of atoms
- [113] - Takahashi, H. Murakawa, Y. Sakaino, T. Ohzeki, J. Abe and O. Yamada,  
*Time-resolved resonance raman studies of the photochromic reaction of  
6-nitro-1',3',3'-trimethylspiro[2H-1-benzopyran-2,2'-indoline]*,  
J. Photochem. Photobiol., A 45 (1988) 233
- [114] - P. Yannoulis, R. Dudde, K. H. Frank and E. E. Koch  
*Orientation of Aromatic Hydrocarbons on Metal Surfaces  
as Determined by NEXAFS*,  
Surf. Sci. 189/190 (1987) 519
- [115] - D. Syomin, J. Kim, and B. E. Koel  
*Identification of Adsorbed Phenyl (C<sub>6</sub>H<sub>5</sub>) Groups on Metal Surfaces:  
Electron-Induced Dissociation of Benzene on Au(111)*,  
J. Phys. Chem. B 105 (2001) 8387
- [116] - N. Koch, A. Elschner, J. P. Rabe, R. L. Johnson  
*Work Function Independent Hole-Injection Barriers Between  
Pentacene and Conducting Polymers*,  
Adv. Mater. 17 (2005) 330
- [117] - Q.-S. Xin and X.Y. Zhu,  
*Temperature dependent photodesorption of methyl radical from  
GaAs: role of the initial state*,  
Chem. Phys. Lett. 265 (1997) 259
- [118] - S. Thiel, T. Klüner, M. Wilde, K. Al-Shamery and H.-J. Freund,  
*The role of the initial population of molecular vibrations,  
in surface photochemistry*,  
Chem. Phys. 228 (1998) 185

- [119] - D. Kröner, S. Klinkusch and T. Klamroth,  
*Enhanced photodesorption by vibrational pre-excitation:  
Quantum model simulations for Cs/Cu(111),*  
Surf. Sci. 602 (2008) 3148
- [120] - H. Arnolds, R. J. Levis and D. A. King,  
*Vibrationally assisted DIET through transient temperature rise:  
the case of benzene on Pt(111),*  
Chem. Phys. Lett. 380 (2003) 444
- [121] - S. Hagen,  
*Isomerization behavior of photochromic molecules  
in direct contact with noble metal surfaces,*  
Dissertation, May 2009  
Institut für Experimentalphysik , Freie Universität Berlin
- [122] - X. H. Qiu, G. V. Nazin and W. Ho,  
*Vibrationally Resolved Fluorescence Excited with Submolecular Precision,*  
Science 299 (2003) 542
- [123] - F. Pump, R. Temirov, O. Neucheva, S. Soubatch, S. Tautz,  
M. Rohlfing and G. Cuniberti,  
*Quantum transport through STM-lifted single PTCDA molecules,*  
Appl. Phys. A 93 (2008) 335
- [124] - L. Lafferentz, F. Ample, H. Yu, S. Hecht, C. Joachim and L. Grill,  
*Conductance of a Single Conjugated Polymer  
as a Continuous Function of Its Length,*  
Science 323 (2009) 1193
- [125] - W. Haiss, C. Wang, I. Grace, A. S. Batsanov, D. J. Schiffrin,  
S. J. Higgins, M. R. Bryce, C. J. Lambert and R. J. Nichols,  
*Precision control of single-molecule electrical junctions,*  
Nat. Mater. 5 (2006) 995
- [126] - C.-C. Kaun and T. Seideman,  
*Conductance, contacts, and interface states in  
single alkanedithiol molecular junctions,*  
Phys. Rev. B: Condens. Matter 77 (2008) 033414
- [127] - R. Temirov, A. Lassise, F. B. Anders and F. S. Tautz,  
*Kondo effect by controlled cleavage of a single-molecule contact,*  
Nanotechnology 19 (2008) 065401

- [128] - J. van Ruitenbeek, E. Scheer and H. B. Weber,  
*Contacting Individual Molecules Using Mechanically  
Controllable Break Junctions*,  
Lecture Notes in Physics 680 (2005) 253  
Springer Verlag Berlin, Heidelberg, New York
- [129] - M. Galperin, M. A. Ratner and Abraham Nitzan,  
*On the Line Widths of Vibrational Features in Inelastic  
Electron Tunneling Spectroscopy*,  
Nano Lett. 4 (2004) 1605
- [130] - Y. Jean,  
*Molecular Orbital of Transition Metal Complexes*, 1st English Edition, (2005)  
Oxford University Press
- [131] - Ying Luo, Rainer Haag  
Institut für Chemie und Biochemie, Freie Universität Berlin
- [132] - Svetlana Klyatskaya, Mario Ruben  
Institut für Nanotechnologie, Forschungszentrum Karlsruhe
- [133] - H.-R. Christen  
*Grundlagen der allgemeinen und anorganischen Chemie*, 8th Edition, (1985)  
Otto Salle Verlag, Frankfurt am Main  
Verlag Sauerländer, Aarau
- [134] - L. Venkataraman, J. E. Klare, C. Nuckolls,  
M. S. Hybertsen and M. L. Steigerwald,  
*Dependence of single-molecule junction conductance  
on molecular conformation*,  
Nature 442 (2006) 904
- [135] - L. Venkataraman, J. E. Klare, I. W. Tam, C. Nuckolls,  
M. S. Hybertsen and M. L. Steigerwald,  
*Single-Molecule Circuits with Well-Defined Molecular Conductance*,  
Nano Lett. 6, 3 (2006) 458

- [136] - Z. L. and D. S. Kosov,  
*Nature of well-defined conductance of amine-anchored molecular junctions:  
Density functional calculations,*  
Phys. Rev. B: Condens. Matter 76 (2007) 035415
- [137] - H. Dürr, J. F. Wendelken and J.-K. Zuo  
*Island morphology and adatom energy barriers  
during homoepitaxy on Cu(001),*  
Surf.Sci. 328 (1995) L527
- [138] - K.-F. Braun and S.-W. Hla  
*Probing the Conformation of Physisorbed Molecules at  
the Atomic Scale Using STM Manipulation,*  
Nano Lett. 5 (2005) 73
- [139] - J. I. Pascual, N. Lorente, Z. Song, H. Conrad and H.-P. Rust,  
*Selectivity in vibrationally mediated single-molecule chemistry,*  
Nature 423 (2003) 525
- [140] - X. Xiao, B. Xu and N. Tao,  
*Conductance Titration of Single-Peptide Molecules,*  
J. Am. Chem. Soc. 126 (2004) 5370
- [141] - J. He, F. Chen, J. Li, O. F. Sankey, Y. Terazono, C. Herrero,  
D. Gust, T. A. Moore, A. L. Moore and Stuart M. Lindsay,  
*Electronic Decay Constant of Carotenoid Polyenes  
from Single-Molecule Measurements,*  
J. Am. Chem. Soc. 127 (2005) 1384
- [142] - Seong Ho Choi, BongSoo Kim, and C. Daniel Frisbie,  
*Electrical Resistance of Long Conjugated Molecular Wires,*  
Science 320 (2008) 1482
- [143] - Marshall D. Newton,  
*Quantum chemical probes of electron-transfer kinetics:  
the nature of donor-acceptor interactions,*  
Chem. Rev. 91 (1991) 767
- [144] - N. L. Allinger,  
*Conformational analysis. 130. MM2.  
A hydrocarbon force field utilizing V1 and V2 torsional terms,*  
J. Am. Chem. Soc. 99 (1977) 8127
- [145] - J. T. Sprague, J. C. Tai, Y. Yuh and N. L. Allinger,  
*The MMP2 calculational method,*  
J. Comput. Chem. 8 (1987) 581



- [146] - N. L. Allinger, R. A. Kok and M. R. Imam,  
*Hydrogen bonding in MM2*,  
J. Comput. Chem. 9 (1988) 591
- [147] - D. M. Schnur, M. V. Grieshaber and J. P. Bowen,  
*Development of an internal searching algorithm for  
parameterization of the MM2/MM3 force fields*,  
J. Comput. Chem. 12 (1991) 844

## Acknowledgment

My special thanks go to Prof. Nacho Pascual for the opportunity to write this thesis in his group and for lots of support he was providing during the last years.

I also want to express my special thanks to Prof. Katharina Franke, who always was a great help in any respect.

For making the effort to read through this thesis, I want to thank Prof. Paul Fumagalli.

I furthermore want to thank all the colleagues of our group and of the groups of P. Fumagalli, L. Grill, W. Kuch and P. Tegeder for the fruitful and nice collaboration and, of course, all friends and relatives for the positive social environment. Extra thanks to Isa and Hendrik for proof-reading.

For supporting us with theoretical data for this work I want to thank the groups of Th. Frauenheim and A. Pecchia.

Finally, I am obliged to the Deutsche Forschungsgemeinschaft for funding my positions through the Sfb 658 and the SPP 1243.



## Curriculum Vitae

For reasons of data protection,  
the curriculum vitae is not included in the online version.

## List of Publications

### Publications related to this thesis

K. J. Franke, G. Schulze and J. I. Pascual,  
*Excitation of Jahn-Teller active modes during electron transport through  
single C<sub>60</sub> molecules on metal surfaces between lead electrodes,*  
Submitted to Nano Lett.

M. Piantek<sup>1</sup>, G. Schulze<sup>1</sup>, M. Koch, K. J. Franke, F. Leyssner, A. Krüger, C. Navío, J. Miguel, M. Bernien, M. Wolf, W. Kuch, P. Tegeder and J. I. Pascual  
*Reversing the Thermal Stability of a Molecular Switch on a Gold Surface: Ring-Opening Reaction of Nitrospiropyran,*  
J. Am. Chem. Soc. 131 (2009) 12729

G. Schulze, K. J. Franke, and J. I. Pascual  
*Current induced heating and heat dissipation mechanisms in single C<sub>60</sub> molecular junctions,*  
in *Current-Driven Phenomena in Nanoelectronics*,  
Pan Stanford Publishing, submitted

T. Frederiksen, K. J. Franke, A. Arnau, G. Schulze, J. I. Pascual and N. Lorente  
*Dynamic Jahn-Teller effect in electronic transport through single C<sub>60</sub> molecules,*  
Phys. Rev. B: Condens. Matter 78 (2008) 233401

G. Schulze, K. J. Franke, and J. I. Pascual  
*Resonant heating and substrate-mediated cooling of a single C<sub>60</sub> molecule in a tunnel junction,*  
New J. Phys. 10 (2008) 065005

G. Schulze, K. J. Franke, A. Gagliardi, G. Romano, C. S. Lin, A. L. Rosa, T. A. Niehaus, Th. Frauenheim, A. Di Carlo, A. Pecchia and J. I. Pascual  
*Resonant Electron Heating and Molecular Phonon Cooling in Single C<sub>60</sub> Junctions,*  
Phys. Rev. Lett. 100 (2008) 136801

K. J. Franke, G. Schulze, N. Henningsen, I. Fernández-Torrente, J. I. Pascual, S. Zarwell, K. Rück-Braun, M. Cobian, and N. Lorente  
*Reducing the molecule-substrate coupling in C<sub>60</sub>-based nanostructures by molecular interactions,*  
Phys. Rev. Lett. 100 (2008) 036807

---

<sup>1</sup>Both authors contributed equally to this work.

## Publications not related to this thesis

N. Henningsen, K. J. Franke, G. Schulze, I. Fernández-Torrente, B. Priewisch, K. Rück-Braun, J. I. Pascual  
*Active intramolecular conformational dynamics controlling the assembly of azobenzene derivatives at surfaces,*  
Chem. Phys. Chem. 9 (2008) 71

N. Henningsen, K. J. Franke, I. Fernández-Torrente, G. Schulze, B. Priewisch, K. Rück-Braun, J. Dokić, T. Klamroth, P. Saalfrank and I. J. Pascual  
*Inducing the Rotation of a Single Phenyl Ring with Tunneling Electrons,*  
J. Phys. Chem. C 111 (2007) 14843

I. Fernández-Torrente, K. J. Franke, N. Henningsen, G. Schulze, M. Alemani, Ch. Roth, R. Rurali, N. Lorente and J. I. Pascual,  
*Spontaneous formation of triptycene supramolecules on surfaces,*  
J. Phys. Chem. B 110 (2006) 20089

K. Langfeld, H. Reinhardt and G. Schulze,  
*Correlations of center flux in  $SU(2)$  Yang-Mills theory,*  
Proceedings of Science, Lattice 2005 (2005) 321

K. Langfeld, G. Schulze, H. Reinhardt,  
*Center flux correlation in  $SU(2)$  Yang-Mills theory,*  
Phys. Rev. Lett. 95 (2005) 221601

